

SPHERICAL BARIUM FERRITE NANOPARTICLES AND HEXAFERRITE SINGLE  
CRYSTALS FOR INFORMATION DATA STORAGE AND  
RF DEVICES

by

JEEVAN PRASAD JALLI

YANG-KI HONG, COMMITTEE CHAIR

ALAN M. LANE  
BYOUNG CHUL CHOI  
DAWEN LI  
SEONGSIN KIM

A DISSERTATION

Submitted in partial fulfillment of the requirements  
for the degree of Doctor of Philosophy  
in the Department of Electrical and Computer Engineering  
in the Graduate School of  
The University of Alabama

TUSCALOOSA, ALABAMA

2014

Copyright Jeevan Prasad Jalli 2014  
ALL RIGHTS RESERVED

## ABSTRACT

Since their discovery in the early 1950's hexagonal ferrites or hexaferrites have been studied for a long time because of their technological applications, such as microwave devices and high density magnetic recording media. In this dissertation efforts have been made to address these two applications by developing nanosized spherical barium ferrite particles for advanced magnetic recording media, and hexaferrite single crystals for low loss RF devices. Accordingly, this dissertation consists of two parts; part one spherical barium ferrite nanoparticles for information data storage media, and part two hexaferrite single crystals for RF devices.

### **Part I. Spherical Barium Ferrite Nanoparticles**

Hexagonal barium ferrite (H-BaFe) nanoparticles are good candidates for particulate recording media due to their high uniaxial magnetocrystalline anisotropy, excellent chemical stability, and narrow switching field distribution. One major disadvantage of using H-BaFe particles for particulate recording media is their poor dispersion and a high degree of stacking that deteriorate the recording capability by creating large media noise and surface roughness. One way to solve and improve the recording performance of H-BaFe media is employing substantially nanosized spherical barium ferrite (S-BaFe) particles. Spherical shaped particles have low aspect ratio and only form a point-to-point contact, unlike the H-BaFe particles. Therefore, using S-BaFe particles not only decrease the degree of magnetic interaction between the particles but also can substantially increases the recording performance by improving the

dispersion and SNR of the particles in the magnetic media. In this dissertation, two different approaches were employed successfully to synthesize S-BaFe nanoparticles in the range of 20-45 nm.

## **Part II. Hexaferrite Single Crystals**

As wireless communication systems are flourishing, and the operating frequencies are increasing, there is a great demand for RF devices such as circulators and isolators. Traditional RF devices using spinel or garnets are disadvantageous in the millimeter range frequencies, since they require a strong external bias field provided by external permanent magnets. A promising approach to circumvent this problem is to use the high crystalline anisotropy field in the hexaferrites. Single crystals of M and Y-type hexaferrites show promising results with their low microwave losses and excellent magnetic and physical properties. In this dissertation efforts to grow, high-quality bulk M and Y-type single crystals with the aim to study and improve their magnetic and microwave properties with respect to different cation dopant elements is reported. Also, a liquid phase epitaxial technique was developed to grow thick barium ferrite films onto semiconductor substrates. Finally, magnetic domain patterns on bulk M-type single crystals was studied by using a magnetic force microscopy technique.

## DEDICATION

This dissertation is dedicated to my beloved parents Varaprasad and Raja Latha Jalli. Also, this masterpiece would not have been completed without the constant support and encouragement from my lovely wife Alysha and our kids Sunjay and Samirah Jalli.

## LIST OF ABBREVIATIONS AND SYMBOLS

$M$	Magnetization
$H$	Magnetic field
$M_r$	Remanent magnetization
$M_s$	Saturation magnetization
$H_c$	Coercivity
$S$	Remanent squareness
$S^*$	Coercive squareness
$K$	Anisotropy constant
$K_s$	Shape anisotropy constant
$E$	Magnetocrystalline anisotropy energy
$E_{ms}$	Magneto-static energy
$H_d$	Demagnetizing field
$N_d$	Demagnetizing coefficient or factor
$H_{ci}$	Intrinsic coercivity
$D$	Particle diameter size
$D_s$	Single domain particle diameter size
$r_c$	Critical radius of a particle
$A$	Exchange constant
$K_u$	Uniaxial anisotropy constant

$D_p$	Critical superparamagnetic size
$V$	Volume of the particle
$k_B$	Boltzmann constant
$KV$	Anisotropy energy of the particle
$k_B T$	Thermal energy
$T$	Absolute temperature
$H_a$	Intrinsic coercive field
$f$	Frequency of magnetization reversal
$f_0, A$	Attempt frequency
$t$	Time
$\tau$	Lifetime of the particle
$H_{cr}$	Remanent coercivity of the particles
$\frac{K_u V}{k_B T}$	Thermal stability factor
$H_A$	Uniaxial magnetocrystalline anisotropy
MP	Metal particles
GMR	Giant magnetoresistive heads
SNR	Signal- to-noise ratio
SFD	Switching field distribution
H-BaFe	Hexagonal barium ferrite
BaFe	Barium ferrite
S-BaFe	Spherical barium ferrite nanoparticles
S-Mag	Spherical magnetite nanoparticles
XRD	X-ray diffractometer

TEM	Transmission electron microscopy
HR-TEM	High resolution transmission electron microscopy
VSM	Vibrating sample magnetometer
IRM	Isothermal remanence curve
DCD	DC demagnetization curve
$\Delta M$	DCD – (1–2 (IRM))
$\sigma_s$	Saturation Magnetization
TGA	Thermogravimetry analysis
$4\pi M_s$	Saturation Magnetization
BaM	Barium ferrite
SrM	Strontium ferrite
Sm-SrM	Samarium doped strontium ferrite
Zn-Y	$\text{Ba}_2\text{Zn}_2\text{Fe}_{12}\text{O}_{22}$ hexaferrite
Mg-Y	$\text{Ba}_2\text{Mg}_2\text{Fe}_{12}\text{O}_{22}$ hexaferrite
SrBa-Y	$\text{Sr}_{1.5}\text{Ba}_{0.5}\text{Zn}_2\text{Fe}_{12}\text{O}_{22}$ hexaferrite
Zr-Zn-Y	$\text{Ba}_2\text{Zn}_2\text{Zr}_x\text{Fe}_{12-x}\text{O}_{22}$
$e$	Charge of the electron
$m_e$	Mass of the electron
$h$	Planks Constant
$H_0$	Applied DC magnetic field
$T$	Torque
$\vec{M}_{tot}$	Total magnetization
$\vec{H}_{tot}$	Internal magnetic field

$\mu_0$	Permeability of free-space
$\omega$	Operating frequency
$\omega_0$	Resonance frequency
$\omega_m$	Magnetization frequency
$[\mu]$	Tensor Permeability
$H_{res}$	Resonant magnetic field
$f_r$	Resonance frequency
$\gamma'$	Gyromagnetic ratio
LPE	Liquid phase epitaxy
FMR	Ferromagnetic resonance
$\Delta H$	Ferromagnetic resonance (FMR) linewidth
AFM	Atomic force microscopy
MFM	Magnetic force microscopy
$\delta$	Magnetic domain width
$T$	Thickness of the crystal

## ACKNOWLEDGMENTS

It is my greatest pleasure to have this opportunity to express my sincere appreciation to everyone who helped me during my Ph.D. program at the University of Alabama. The most important person is my advisor Prof. Yang-Ki Hong, who guided me into the field of magnetism and magnetic materials. He provided me his excellent guidance, expertise and moral support which were all essential for my success not only as a student, but also in my professional life.

I would like to thank all my committee members, Prof. Lane, Prof. Choi, Prof. Li and Prof. Kim for serving on my committee and for their valuable feedback and corrections on my dissertation. I would like to thank all my lab colleagues: Dr. Seok Bae, Dr. Terimitsu Tanaka, Jaejin Lee, Jihoon Park, Wancheol Lee, and Gavin Abo for their constant help and support.

I thank the MINT center and the CAF facilities staff at the University of Alabama for helping me with the characterization tools for my research. I also appreciate the financial support from the Information Storage Industry Consortium (INSIC) and the E. A. "Larry" Drummond Endowment at the University of Alabama.

Finally, I would like to thank all of my family members, especially my wife, for her continuous love and support.

## CONTENTS

ABSTRACT.....	ii
DEDICATION.....	iv
LIST OF ABBREVIATIONS AND SYMBOLS .....	v
ACKNOWLEDGMENTS .....	ix
LIST OF TABLES.....	xiv
LIST OF FIGURES .....	xv
<b>PART I. SPHERICAL BARIUM FERRITE .....</b>	<b>1</b>
<b>1. Introduction.....</b>	<b>1</b>
1.1. Magnetic tape technology .....	3
1.2. Magnetic tape media requirements.....	5
1.2.1. Magnetic hysteresis loops.....	5
1.2.2. Magnetic anisotropy.....	7
1.2.3. Magnetocrystalline anisotropy.....	8
1.2.4. Shape anisotropy.....	9
1.2.5. Magnetostriction .....	10
1.2.6. Signal to noise ratio (SNR).....	11
1.3. Magnetic properties of small particles .....	11
1.4. Superparamagnetism and thermal stability .....	13
1.5. Magnetic particles for recording media.....	18
1.5.1. Metal based magnetic particles.....	18
1.5.2. Hexagonal barium ferrite particles and media properties .....	19

1.5.3. Recording characteristics of H-BaFe media .....	21
<b>2.0. Objectives</b> .....	26
<b>3.0. Spherical magnetite nanoparticles (S-Mag)</b> .....	28
3.1. Introduction .....	28
3.2. Experimental .....	28
3.2.1. Synthesis of iron oleate complex .....	31
3.2.2. Synthesis of magnetite nanoparticles.....	31
3.3. Results and discussion.....	33
<b>4.0. Hematite nanocubes</b> .....	36
4.1. Introduction .....	36
4.2. Experimental .....	39
4.3. Results and discussion.....	41
<b>5.0. Spherical barium ferrite (S-BaFe)</b> .....	44
5.1. Introduction .....	44
5.2. Experimental .....	44
5.3. Results and discussion.....	48
5.3.1. S-BaFe synthesized from S-Mag precursor particles.....	48
5.3.2. S-BaFe synthesized from hematite nanocubes .....	56
<b>6.0. S-BaFe synthesis from worm-shaped hematite nanoparticles</b> .....	64
6.1. Introduction .....	64
6.2. Experimental .....	65
6.3. Results and discussion.....	66

<b>PART II. HEXAFERRITE SINGLE CRYSTALS.....</b>	<b>73</b>
<b>1. Introduction.....</b>	<b>73</b>
1.1. M-type barium ferrite (BaM) .....	76
1.2. Y-type barium ferrite.....	78
1.3. Magnetic and microwave properties of hexagonal ferrites .....	79
1.3.1. Saturation magnetization .....	79
1.3.2. Magnetocrystalline anisotropy field .....	80
1.3.3. Magnetic domains, coercive field, and remanence.....	80
1.3.4. Microwave properties-permeability tensor and ferromagnetic resonance.....	81
1.3.5. Applications of hexaferrites for microwave devices .....	89
<b>2.0. Objectives.....</b>	<b>93</b>
<b>3.0. Liquid phase epitaxy growth of BaM films .....</b>	<b>94</b>
3.1. Introduction .....	94
3.2. Experimental .....	96
3.3. Results and discussion.....	99
<b>4.0. Magnetic and microwave properties of M-type Sm-doped     SrFe<sub>12</sub>O<sub>19</sub> single crystals .....</b>	<b>105</b>
4.1. Introduction .....	105
4.2. Experimental .....	106
4.3. Results and discussion.....	107
<b>5.0. Ferrimagnetic Sr<sub>(2-x)</sub>Ba<sub>x</sub>Zn<sub>2</sub>Fe<sub>12</sub>O<sub>22</sub> (x = 0.5) (Zn-Y) single     crystal with planar anisotropy .....</b>	<b>114</b>
5.1. Introduction .....	114
5.2. Experimental .....	115

5.3. Results and discussion.....	117
<b>6.0. Magnetic and microwave properties of ferrimagnetic Zr-substituted Ba<sub>2</sub>Zn<sub>2</sub>Fe<sub>12</sub>O<sub>22</sub> (Zn-Y) single crystal .....</b>	<b>122</b>
6.1. Introduction .....	122
6.2. Experimental .....	123
6.3. Results and discussion.....	125
<b>7.0. MFM studies of magnetic domain patterns in BaM single crystals .....</b>	<b>131</b>
7.1. Introduction .....	131
7.2. Experimental .....	132
7.3. Results and discussion.....	134
CONCLUSIONS.....	141
FUTURE WORK.....	145
REFERENCES .....	147
APPENDIX A.....	159
APPENDIX B .....	162

## LIST OF TABLES

### Part-1

1.1	Barium ferrite magnetic site and calculated $K_1$ for $\text{Fe}^{3+}$ by single ion anisotropy model [12] .....	20
5.1	Magnetic properties of barium ferrite nanoparticles at various heat treatment temperatures .....	52
8.1	Magnetic properties of S-BaFe nanoparticles achieved by the three different processes.....	142

### Part-2

1.1	Chemical composition and interrelation of hexagonal ferrites, where S = $\text{Fe}_6\text{O}_8$ (spinel), R = $\text{BaFe}_6\text{O}_{11}$ (hexagonal), and T = $\text{Ba}_2\text{Fe}_8\text{O}_{14}$ (hexagonal). The asterisk (*) indicates that the corresponding sub-unit is rotated $180^\circ$ around the hexagonal $c$ -axis [9] .....	75
1.2	Barium ferrite magnetic site and calculated $K_1$ for $\text{Fe}^{3+}$ by single ion anisotropy model [12] .....	77
4.1	Magnetic properties of Sm-SrM single crystal with various compositions .....	110
6.1	Compositions and magnetic properties of $\text{Ba}_2\text{Zn}_2\text{Zr}_x\text{Fe}_{12-x}\text{O}_{22}$ single crystal .....	126

## LIST OF FIGURES

### Part-1

1.1	Magnetic tape product and tape technology road map showing the areal densities in comparison with hard disk drives [3].....	2
1.2.	Cross section of a magnetic tape.....	4
1.3	Magnetic tape recording a) helical scan recording b) linear tape recording .....	4
1.4	A typical M–H loop for a ferromagnetic material .....	6
1.5	Schematic of a prolate ellipsoid.....	9
1.6	Variation of intrinsic coercivity $H_{ci}$ with particle diameter $D$ [13] ..	12
1.7	An illustration showing the difference in the energy barrier between the two possible magnetization states of a magnetic particle (a) before and (b) after the particle reaches a critical size for the onset of the superparamagnetic effect .....	13
1.8	Illustration of a single-domain prolate spheroidal particle [19].....	14
1.9	Magnetic structure of barium ferrite ( $\text{BaFe}_{12}\text{O}_{19}$ , BaFe) [36].....	20
1.10	Advanced H-BaFe particles used by Fujifilm to achieve the recording densities of (a) $6.67 \text{ Gb/in}^2$ and (b) $29.5 \text{ Gb/in}^2$ [55-56].....	24
1.11	(a) Artist’s drawings for particles dispersion of hexagonal shape [60-65] and (b) TEM micrograph of hexagonal barium ferrite .....	25
1.12	Artist’s drawings for particles dispersion of spherical shape barium ferrite (S-BaFe) [60-62].....	25
3.1	Spinel crystal structure [67].....	29

3.2	Flowchart and the experimental setup used to synthesize S-Mag nanoparticles .....	32
3.3	XRD patterns of spherical magnetite nanoparticles at room temperature .....	33
3.4	TEM micrographs of S-Mag nanoparticles.....	34
3.5	TEM micrographs of the S-Mag nanoparticles synthesized from (a) 1-eicosene and (b) trioctylamine solvents respectively.....	34
3.6	Magnetic hysteresis loop of as-synthesized S-Mag nanoparticles....	35
3.7	Mössbauer spectra of S-Mag nanoparticles .....	35
4.1	Unit cell of hematite viewed in the [001] and [110] directions [84-85].....	36
4.2	Flowchart and the experimental setup used to synthesize hematite nanocubes .....	38
4.3	XRD patterns of hematite nanocubes at room temperature .....	40
4.4	TEM micrographs of the as-synthesized hematite nanocubes .....	40
4.5	TEM images of the hematite products obtained with FeCl <sub>3</sub> / sodium oleate (CFe/SO) ratio (a) CFe/SO = 0.22 (b) CFe/SO = 0.34 (c) CFe/SO = 0.40 and (d) CFe/SO= 0.50.....	42
4.6	Room-temperature hysteresis loops of the hematite particles with FeCl <sub>3</sub> / sodium oleate (CFe/SO) ratio (a) CFe/SO = 0.22 (b) CFe/SO = 0.34 (c) CFe/SO = 0.40 and (d) CFe/SO= 0.50.....	43
5.1	Experimental process for the synthesis of S-BaFe nanoparticles .....	44
5.2	Flowchart and the experimental setup used to synthesize S-BaFe nanoparticles .....	46
5.3	XRD patterns of the as-collected S-Mag nanoparticles (a) before BaCO <sub>3</sub> coating and (b) after BaCO <sub>3</sub> coating onto the S-Mag particles respectively.....	48
5.4	XRD patterns of S-BaFe as a function of various heat-treated temperatures; (a) 650 °C for 2 h, (b) 700 °C for 2 h, (c) 800 °C for 2 h, and (d) 900 °C for 2 h.....	49

5.5	TEM micrographs of S-BaFe nanoparticles heat-treated at 900 °C for 2 h.....	51
5.6	HR-TEM electron diffraction patterns of S-BaFe nanoparticles .....	51
5.7	Magnetic hysteresis loops of S-BaFe nanoparticles as a function of various heat-treated temperatures .....	52
5.8	Mössbauer spectra of S-BaFe nanoparticles heat-treated at 900 °C for 2 h.....	53
5.9	$\Delta M$ curve of spherical barium ferrite (S-BaFe) and hexagonal barium ferrite (H-BaFe) nanoparticles .....	54
5.10	Remanent coercivity as a function of time measured by VSM and fitted curve using Sharrock's equation [110] .....	55
5.11	Magnetic hysteresis loops of the precursory hematite nanocubes before and after BaCO <sub>3</sub> coating .....	56
5.12	XRD patterns of the precursory hematite nanocubes before and after BaCO <sub>3</sub> coating .....	57
5.13	Thermogravimetry analysis curve showing the percentage weight as a function of temperature for the as-coated hematite nanocubes .....	58
5.14	XRD patterns of S-BaFe as a function of various heat-treated temperatures; (a) 650 °C for 2 h, (b) 700 °C for 2 h, (c) 800 °C for 2 h, and (d) 900 °C for 2 h.....	59
5.15	Magnetic properties of S-BaFe nanoparticles as a function of various heat-treated temperatures .....	59
5.16	TEM micrographs of S-BaFe nanoparticles heat-treated at 900 °C for 2 h.....	60
5.17	Mössbauer spectra of S-BaFe nanoparticles heat-treated at 900 °C for 2 h.....	61
5.18	$\Delta M$ curve of spherical barium ferrite (S-BaFe) and hexagonal barium ferrite (H-BaFe) nanoparticles.....	62
6.1	Flowchart showing the process to synthesize S-BaFe nanoparticles .....	64

6.2	Magnetic properties of as-collected oven dried precursor nanoparticles .....	65
6.3	XRD patterns of the as-collected oven dried nanoparticles.....	66
6.4	TEM micrographs of as-collected oven dried nanoparticles .....	67
6.5	XRD patterns of S-BaFe as a function of various heat-treatment temperatures (a) 680°C, (b) 700°C, (c) 750°C, and (d) 800°C for 2 h .....	67
6.6	TEM micrographs of S-BaFe nanoparticles heat-treated at 800°C for 2 h.....	68
6.7	Magnetic hysteresis loop of S-BaFe heat-treated at 800°C for 2 h.....	69
6.8	Magnetic properties as a function of heat-treatment temperatures of S-BaFe nanoparticles .....	70
6.9	Remanent coercivity as a function of time measured by VSM and fitted curve using Sharrock's equation [110] .....	71

## Part-2

1.1	Chemical composition diagram showing how the hexagonal ferrites are derived from the spinel $\text{MeO} \cdot \text{Fe}_2\text{O}_3$ structure [9].....	74
1.2	Magnetic structure of barium ferrite BaM ( $\text{BaFe}_{12}\text{O}_{19}$ , BaFe) [10] .....	75
1.3	Magnetic structure of Y-Type hexaferrites ( $\text{Ba}_2\text{Me}_2\text{Fe}_{12}\text{O}_{22}$ ) [9].....	77
1.4	Spin magnetic dipole moment and angular momentum vectors for a spinning electron [29].....	82
1.5	(a)Precession of a spinning unpaired electron at frequency $\omega_0$ about a static dc magnetic field (b) resonance absorption curve as a function of applied magnetic field .....	87
1.6	General schematic of a Y-junction stripline circulator [31] .....	89
1.7	Energy flow diagram of ferrite disk related to the port of the Y-junction circulator [30] .....	90

1.8	Ferrite resonance frequency as a function of dc magnetic field for various values of the anisotropy field [34].....	91
3.1	Liquid phase epitaxy system.....	95
3.2	Schematic of LPE system .....	96
3.3	Flow chart of the LPE process to grow BaM thick films .....	98
3.4	Scanning electron micrograph showing the cross sectional area and the top view of 144 $\mu\text{m}$ thick LPE processed BaM film.....	99
3.5	X-ray diffraction pattern of 144 $\mu\text{m}$ thick BaM film on (111) GGG substrate.....	100
3.6	Torque measurement of 144 $\mu\text{m}$ thick BaM film on (111) GGG substrate at $H_{\text{App}} = 10 \text{ kOe}$ .....	101
3.7	Magnetic hysteresis loop of the 144 $\mu\text{m}$ thick BaM film on (111) GGG substrate.....	101
3.8	FMR linewidth of the 144 $\mu\text{m}$ thick BaM film.....	103
4.1	Experimental flowchart to grow Sm-SrM type single crystals.....	106
4.2	Optical micrograph of the Sm-SrM single crystals.....	107
4.3	Magnetic hysteresis loop of Sm-SrM single crystal, when external magnetic field is out-of- plane (solid line) and in-plane (dashed line) to the crystal plane .....	108
4.4	Magnetic hysteresis loop of Sm-SrM single crystal as a function of the magnetic field applied at various angles with respect to the $c$ -axis of the crystal.....	109
4.5	X-ray diffraction pattern of a Sm-SrM single crystal showing the (00 $l$ ) planes of the crystal .....	111
4.6	X-ray diffraction pattern of the powdered bulk crystals of Sm-SrM single crystal .....	111
4.7	Mössbauer spectra of the powdered Sm-SrM single crystals .....	112
4.8	Ferrimagnetic resonance spectra of a thin single crystal of Sm-SrM with a linewidth of 85 Oe at 53 GHz.....	113

5.1	Experimental flowchart to grow SrBa-Y type single crystals .....	115
5.2	Optical micrograph of several bulk SrBa-Y single crystals showing the hexagonal growth habit morphology .....	116
5.3	X-ray powder diffraction pattern of a SrBa-Y single crystal.....	116
5.4	Magnetic hysteresis loop of SrBa-Y single crystal.....	117
5.5	Magnetic hysteresis loop of (a) Zn-Y and (b) SrBa-Y single crystal at low applied field .....	118
5.6	Plot of frequency vs FMR resonance field for a single crystal SrBa-Y sample .....	119
5.7	Plot of FMR linewidth vs. frequency for a single crystal SrBa-Y sample .....	120
5.8	Ferrimagnetic resonance linewidth of a SrBa-Y single crystal sample showing the linewidth of 41Oe at 10 GHz .....	121
6.1	Experimental flowchart to grow Zr-Zn-Y type single crystals.....	123
6.2	Optical micrograph of bulk single crystals of Zr-Zn-Y ( $Ba_2Zn_2Zr_xFe_{12-x}O_{22}$ ).....	123
6.3	X-ray powder diffraction pattern reflecting all the major planes, which confirm Zn-Y composition .....	124
6.4	Magnetic hysteresis loops of $Ba_2Zn_2Zr_xFe_{12-x}O_{22}$ single crystal, when external magnetic field is applied in-plane (easy axis) and out-of-plane (hard axis) .....	125
6.5	Angular dependence of magnetization for $Ba_2Zn_2Zr_xFe_{12-x}O_{22}$ single crystal, when external magnetic field is applied in-plane (easy axis) and out-of-plane (hard axis).....	128
6.6	Plot of frequency vs FMR resonance field for a single crystal Zr-Zn-Y.....	128
6.7	Ferrimagnetic resonance linewidth of a Zr-Zn-Y single crystal sample showing the linewidth of 18 Oe at 9 GHz .....	130
7.1	Experimental flowchart to grow BaM single crystals.....	133
7.2	SEM image of a bulk BaM single crystal showing the	

top view and the cross-sectional view .....	134
7.3 X-ray diffraction pattern of a BaM single crystal showing the (00 $l$ ) planes of the crystal.....	135
7.4 Magnetic hysteresis loops of BaM single crystal, when external magnetic field is applied out-of-plane and in-plane of the crystal.....	135
7.5 AFM and MFM images of a BaM single crystal on the (a) basal plane and (b) prism plane .....	136
7.6 Artist's sketch showing the domain patterns on the basal plane and the prism plane of a bulk BaM single crystal.....	136
7.7 AFM and MFM images showing the thickness dependence on domain width of (a) 800 $\mu\text{m}$ , (b) 500 $\mu\text{m}$ , and (c) 100 $\mu\text{m}$ thick BaM crystal .....	138
7.8 Measured relationship between the domain width ( $\delta$ ) and thickness ( $T$ ) of BaM crystals .....	139
7.9 MFM images of BaM single crystal taken on the basal plane (a) as-grown, (b) after a 2 kOe field was applied, (c) after a 4 kOe field was applied, and (d) after a 6 kOe field was applied during the initial magnetization process .....	140

## **PART I. SPHERICAL BARIUM FERRITE**

### **1. Introduction**

Since the early times of computing development, magnetic tape has been the medium of choice for information data storage due to its high volumetric capacity and competitive pricing. Steady advances in drive, media and automation robotics helped it to remain the most effective and reliable solution for data backup and archival storage for data that is less frequently accessed. Automated tape is the most cost-effective storage medium which is less than \$.15 per gigabyte for mainframe storage and between \$0.08 and \$0.12 per gigabyte for open systems storage which are up to 15:1 savings over disk [1]. Moreover, the media life of the tape lasts 10 to 15 years more than 5 years for disk storage, which provides a significant saving on data migration costs. One of the other most important technology aspects of tape media is its ability to be easily transported and stored offsite with no power requirement with an energy cost savings compared to disk of 238:1 over a five-year period [2].

During the last few decades particulate recording media has continued to advance impressively and the amount of data kept on tape is expected to grow at a compound annual growth rate (CAGR) of 45 % from 2010 through 2015 [3]. The latest particulate tape storage formats in the market have a wide range of capacities and performances. The high-end server markets are primarily dominated by IBM and Oracle StorageTek (STK) with tape drives offering high level of performance, reliability, and functionality. Their latest products, IBM-TS1140 and STK-T10000C continue to lead this segment [4-5]. They use linear recording technology and advanced MP tapes to reach capacities of 4-5 TB with a 240-250 MB/sec high data transfer rate

and fast access times respectively. Figure 1.1 shows the roadmap of magnetic tape from the Information Storage Industry Consortium (INSIC) compared to that of the hard disk drive [3]. It appears that the annual areal density progress of hard disk technology has slowed to somewhat less than its recent historical rate of 35% because of the issues that require significant new technology introductions [3]. On the other hand, tape technology is still far away from any fundamental limitations, and INSIC predicts that the growth will continue to increase at the rate of 33.15 %/year till 2022. In addition, laboratory tape demonstrations show a factor of 9 X to 14 X ahead of the latest tape product developments. Recently, in a major breakthrough scientists from IBM Research Center, and FUJIFILM of Japan, demonstrated an advanced prototype tape, at a density of 29.5 billion bits per square inch. This tape is 39 times the areal data density of today's most popular industry-standard magnetic tape with a storage capacity of 35 TB [6].

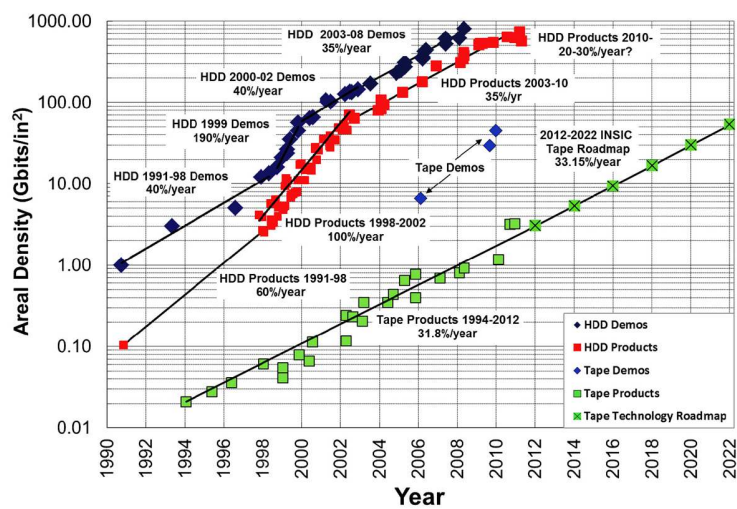


Figure 1.1 Magnetic tape product and tape technology road map showing the areal densities in comparison with hard disk drives [3].

In the next few sections of this dissertation, the physics and fundamentals of the magnetic tape technology with the important magnetic properties are discussed followed by the advantages

of using spherical barium ferrite over metal particles is introduced. Finally, the specific objectives for this part of the dissertation are stated.

### 1.1. Magnetic tape technology

Magnetic tape consists of a thin layer of magnetic particles or top coat suspended within a polymer binder capable of recording a magnetic signal supported by a thicker backing film or substrate. The binder holds the magnetic particles together and to the tape backing while the magnetic layer, is responsible for recording and storing the magnetic signals written on to it. The binder also has the function of providing a smooth surface to facilitate transportation of the tape through the recording system during the record and playback processes. Without the binder, the tape surface would be rough and non-uniform. Other components are added to the binder to help transport the tape and facilitate information playback. A lubricant is also added to the binder to reduce the friction, and the tension needed to transport the tape through the recorder and also tape wear. The backing film or substrate, is required to support the magnetic recording layer, which is too thin and weak to be a stand-alone film layer. In some tape systems, a back coat is applied to the backside of the tape substrate layer. A back coat reduces tape friction, dissipates static charge, and reduces tape distortion by providing a more uniform tape pack wind on the tape reel. A schematic cross-section of a magnetic tape construction is shown in Figure 1.2. It is earlier reported by the Magnetic-Media Industries Association of Japan (MIAJ), that all the three tape components - magnetic particle, binder, and backing - are potential sources of failure for a magnetic tape medium [7].

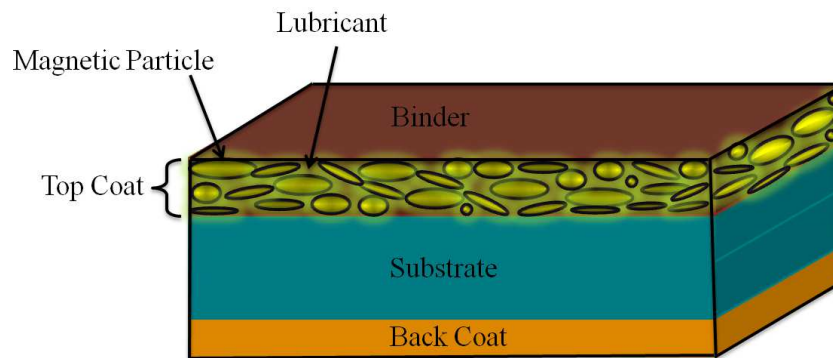


Figure 1.2 Cross section of a magnetic tape.

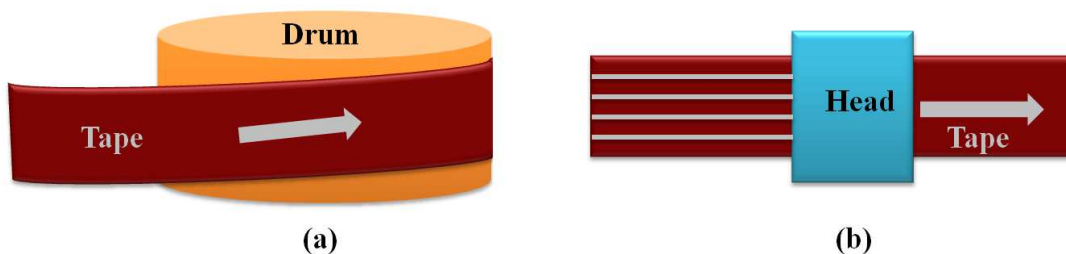


Figure 1.3 Magnetic tape recording a) helical scan recording b) linear tape recording.

Two magnetic tape recording technologies exist: 1) helical scan recording and 2) linear tape recording, as shown in Figure. 1.3 (a) and (b), respectively [8]. In helical scan recording, the recording heads are mounted on a cylindrical drum, which rotates under a specific azimuth angle relative to the tape. The tracks on a magnetic tape are written under the same azimuth angle as the read/write heads are oriented. Helical scan technologies were primarily used in video recorders (VCR) and were generally more complex and less reliable. On the other hand mass data storage and back-up/restore applications use linear tape recording technology also known as the Linear Tape Open (LTO) technology that was introduced in 1998 [8]. The principle of magnetic recording is the same for both the hard disks and magnetic tape. An external magnetic field, created by an inductive write head, induces remanent magnetization of the recording

medium, establishing a series of north and south poles that remain after the magnetic field is removed. The read head, an inductive or a magnetoresistive, passes over the medium and detects magnetic flux reversals (transitions from north to south poles). There are various methods for encoding binary information on the medium, but all methods use detection of flux reversals to represent bit ones and zeros. The number of bits that can be stored in a unit length is called linear bit density and the number of bits that can be stored in a unit area is called areal bit density (or areal recording density).

## 1.2. Magnetic tape media requirements

For a magnetic tape material to be suitable as a recording medium, it must display a number of characteristics: the media magnetization must be reversed by an applied field; maintain its magnetization direction for a long period of time; and the field associated with the magnetized state must be sufficient to be read with a practical read-write head. Accordingly, the particulate media for high recording density should have nanosized particles with high crystalline anisotropy, high coercivity and remanence, low magnetostriction, narrow particle distribution or grain size for smooth surface on substrate, high signal to noise ratio, high Curie temperature, and high thermal stability. The following sections describe some basic magnetic properties that are vital for any recording media and effect the recording performance of the magnetic tape.

### 1.2.1. Magnetic hysteresis loops

Ferromagnetic and ferrimagnetic materials can keep their magnetization to some extent in a given direction after removal of the external magnetic field. This property is displayed by a magnetic hysteresis loop ( $M-H$  loop). A typical  $M-H$  loop is shown in Figure 1.4, which

describes the change of the magnetization ( $M$ ) of a magnetic material with the variation of the intensity of an external magnetic field ( $H$ ). If the initial magnetic state of a material is never magnetized or fully demagnetized ( $M = 0$ ), the magnetization will increase with increase of  $H$ , following the dashed line (called the initial magnetization curve).

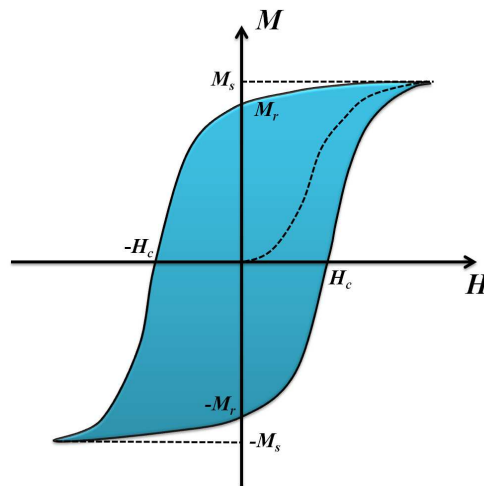


Figure 1.4 A typical  $M$ - $H$  loop for a ferromagnetic material.

The  $M$ - $H$  loop is characterized by remanent magnetization ( $M_r$ ), saturation magnetization ( $M_s$ ) and coercivity ( $H_c$ ), which are all crucial magnetic properties of a material.  $M_r$  is the remaining magnetization of a ferromagnetic material when the applied magnetic field is removed.  $M_s$  is the maximum magnetization that a material could generate. Both  $M_r$  and  $M_s$  are dependent on the composition of the magnetic material and the processing, such as the nature of the atoms and electron structures of materials and also the crystal structures.  $H_c$  is the intensity of the external field required to remove all the magnetization of a material after saturation. Rotation and domain wall motion are two primary processes of magnetization reversal [9]. The value of  $H_c$  is determined by these processes. Magnetic materials with  $H_c < 10$  Oe are usually called soft materials; if  $H_c > 100$  Oe, called hard magnetic materials. Since high  $H_c$  means that the materials are hard to demagnetize (good stability), high  $H_c$  magnetic materials are naturally used as

magnetic recording media. On the contrary, low  $H_c$  magnetic materials are good candidates for the recording head, because it is easy to reverse the magnetization by external field.

The  $M-H$  loop also provides a great deal of other information about magnets. The shape of the initial magnetization curves displays the magnetic characteristics of materials. The curve also shows the processes of domain wall motions. There are two different modes of domain wall motions: nucleation and pinning [10]. In the nucleation-type, magnetic saturation is reached quickly at a low field. This shows that the domain wall can be easily moved and not pinned significantly. In the pinning-type, the saturation magnetization is reached only when a strong field is applied. Here domain wall is substantially pinned, and a relatively strong field is needed to remove pinning sites. Remanent squareness ( $S$ ) and coercive squareness ( $S^*$ ) are used to measure how square the loop is:

$$S = \frac{M_r}{M_s}, S^* = 1 - \frac{M_r / H_c}{\frac{dM(H)}{dH} / H_c} \quad (1.1)$$

usually, large  $S$  and  $S^*$  are required for magnetic recording media since the parameter  $S$  characterizes the flux available for reading and the parameter  $S^*$  characterizes the ability of the medium to sustain sharp transition [11, 12].

### 1.2.2. Magnetic anisotropy

The magnetization of magnetic materials always exhibits direction dependence. This is called magnetic anisotropy, which comes from the different internal energies of the magnetization of a material in different directions. The direction, where the lowest field is required to reach the saturation magnetization is the easy axis. The direction where the highest magnetic field is required is the hard axis. Magnetic anisotropy has a strong effect on the properties of magnetic materials, such as coercivity and remanent magnetization. Usually, it is

necessary to have a high anisotropy constant ( $K_u$ ) to obtain high coercivity which is a very crucial property of a recording medium.

### 1.2.3. Magnetocrystalline anisotropy

Magnetocrystalline anisotropy is a built-in intrinsic anisotropy of a material regarded as a force or certain amount of energy that tends to bind the magnetization to particular crystal direction. These directions are those of spontaneous magnetization in the absence of the applied field and are usually called easy axes or easy directions because they are the easiest directions for the sample to get saturated [13].

Magnetocrystalline anisotropy energy,  $E$ , is the work, the applied field must do to turn the magnetization vector away from an easy direction. In a cubic crystal, such as Fe and Ni,  $E$  is given as:

$$E = K_0 + K_1(\alpha_1^2\alpha_2^2 + \alpha_2^2\alpha_3^2 + \alpha_3^2\alpha_1^2) + K_2(\alpha_1^2\alpha_2^2\alpha_3^2 + \dots) \quad (1.2)$$

where  $K_0, K_1, K_2, \dots$  are magnetocrystalline anisotropy constants, and  $\alpha_1, \alpha_2, \alpha_3$  are the cosines of the angles that the magnetization makes with the crystal axes. In an uniaxial crystal with only one easy axis, such as Co,  $E$  is given as:

$$E = K_0 + K_1\sin^2\theta + K_2\sin^4\theta + \dots \quad (1.3)$$

where  $\theta$  is the angle between the magnetization and the easy axis. The physical origin of magnetocrystalline anisotropy is mainly spin-orbit coupling of electrons [13]. There is very strong orbit-lattice coupling, i.e. the interaction between the orbital motion of electrons and the lattice which is composed of regularly arranged atomic nuclei, and therefore the orientations of electronic orbits are fixed very strongly to the lattice. The magnetocrystalline anisotropy energy is the energy to overcome the spin-orbit coupling and turn the spins away from the easy axis.

Uniaxial materials such as those with a hexagonal crystal structure, have larger magnetocrystalline anisotropy constants than cubic materials. The magnetocrystalline anisotropy constant always decreases as the temperature increases and become zero at or even below Curie temperature [13].

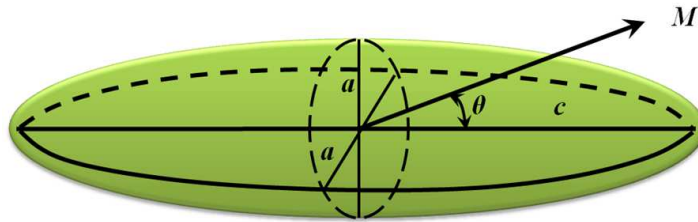


Figure 1.5 Schematic of a prolate ellipsoid.

#### 1.2.4. Shape anisotropy

The physical origin of shape anisotropy is the different magneto-static energy with magnetization in different directions. The magneto-static energy,  $E_{ms}$  (also called self-energy), of a magnet, is the energy due to its magnetization,  $M$ , in the presence of its demagnetizing field,  $H_d$ . By calculating the change of  $E_{ms}$  when the sample is magnetized from 0 to  $M$ , we can get  $E_{ms}$ : [13]

$$E_{ms} = (1/2)N_d M^2 \quad (1.4)$$

where  $N_d$  is the demagnetizing coefficient (or factor).

Considering only the magneto-static energy, the direction in which  $N_d$  is smallest should be the easy direction. Usually,  $N_d$  is smallest along the long-direction, in which the sample is longest. Therefore, the long-direction is usually the easy axis for shape anisotropy. Considering a prolate spheroid (rod-shape) with semi-major axis “ $c$ ” and two semi-minor axes of equal length “ $a$ ”, if the magnetization  $M$  makes an angle  $\theta$  to  $c$ -axis (its easy direction) as shown in Figure 1.5, then its magneto-static energy, which is also its shape anisotropy energy, can be found to be:

$$E_{ms} = E_0 + K_s \sin^2 \theta \quad (1.5)$$

where  $E_0$  and  $K_s$  (shape anisotropy constant) are in the form of:

$$E_0 = (1/2)N_c M^2 \quad (1.6)$$

$$K_s = (1/2)(N_a - N_c)M^2 \quad (1.7)$$

where  $N_a$  and  $N_c$  are the demagnetizing coefficients along  $a$  and  $c$  axes.

Since  $E_0$  doesn't change with direction, the final form of shape anisotropy energy of a prolate spheroid is given by:

$$(E_k)_s = K_s \sin^2 \theta \quad (1.8)$$

where  $K_s$  is given in Eq. 1.7, and  $\theta$  is the angle  $M$  makes with the long  $c$ -axis.  $K_s$  increases with  $c/a$  ratio. When the sample is spherical,  $K_s = 0$ .

### 1.2.5. Magnetostriction

Magnetostriction for a media is a change in shape, dimensions and mechanical properties under the influence of a magnetic field. The deformation  $\Delta l/l$  due to magnetostriction can be as small as  $10^{-5} \sim 10^{-6}$  [14]. The crystal lattice inside each domain deforms in the direction of the domain magnetization (migration of domain walls in response to  $H$ ) and its strain axis rotates with a rotation of the domain magnetization. Thus, the domain wall and domain rotation dynamics result in a deformation (dimensional change) of the magnetic medium. The dimensional change caused by the magnetic interactions within the sample is referred to as spontaneous magnetostriction and the strain induced by an external magnetic field is called forced magnetostriction. The magnetic field causes a change in the domain structure leading to a dimensional change.

### 1.2.6. Signal to noise ratio (SNR)

Areal recording density on magnetic tape is limited by medium magnetic stability, maximum achievable write-head fields, the minimum bit length that can be recorded in the medium, and the signal-to-noise ratio (SNR). The number of particles within a bit or within a transition is one of the key parameters that influence the SNR. Also, the head to tape spacing is the other key parameter that affects the SNR. The signal read from the tape is in general proportional to the number of particles read. Given a specific particle type, if the number of particles per unit volume is increased, the signal will increase proportionately. The media noise read from the tape is proportional to the square root of the number of particles ( $N$ ).

$$SNR = \frac{Signal}{Noise} \propto \sqrt{N} \quad (1.9)$$

therefore, the key is to increase the number of particles within a unit volume of the magnetic layer on the tape, the most common method used to achieve this is to reduce the particle size [15-16]. Model calculations done by J. C. Mallinson, show that in order to achieve a reasonable SNR, about 100 particles per bit are required [21]. Thus as the areal density increases, particles must become smaller. However, reducing the grain size too far causes the small grains in the distribution to become thermally unstable, setting a limit on grain size scaling which will be discussed in the next section.

### 1.3. Magnetic properties of small particles

One of the most important requirements for a magnetic media is to show sufficient hysteresis and coercivity to maintain a permanent record of the data, but not so much as to impede re-magnetization in the field produced by the write head. The recorded information must be erasable if the medium is to be reused. Digital information is encoded in the direction of

magnetization of domains located at identifiable spots on tracks in the magnetic medium. A square hysteresis loop is desirable. The emphasis in magnetic recording is, therefore, on controlling the nucleation of reverse domains, whereas in permanent magnetism the emphasis is on avoiding nucleation altogether. Accordingly, an ideal recording medium should be composed of a thermally stable and non-interacting single domain particle with two well-defined remanent states for information storage. The coercivity  $H_c$  and the squareness ( $S$ ) of magnetic particles are dependent of the size of particles.

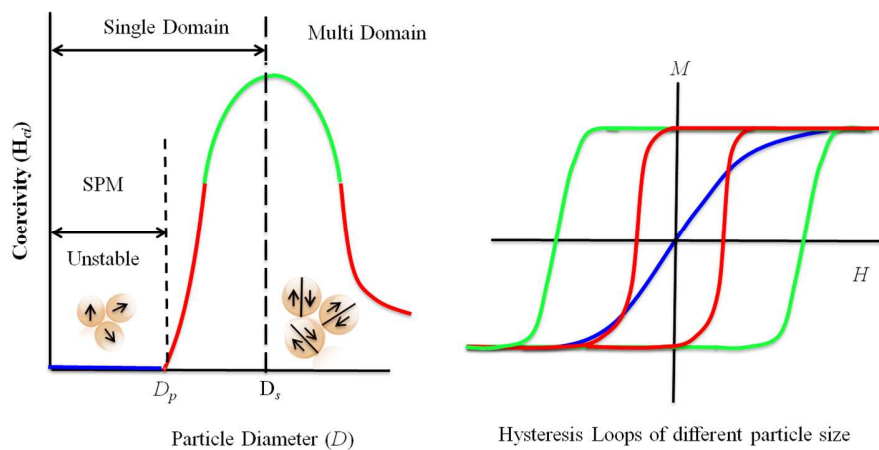


Figure 1.6 Variation of intrinsic coercivity  $H_{ci}$  with particle diameter  $D$  [13].

Figure 1.6 shows how the intrinsic coercivity  $H_{ci}$  changes with particle diameter size  $D$ . Here, the intrinsic coercivity refers to the magnitude of the magnetic field that drives the magnetization to zero after the sample is saturated. In the multi-domain region where  $D > D_s$ ,  $D_s$  is called the critical single domain particle size. As the size of the particle is reduced, the particle cannot longer gain a favorable energy configuration by breaking up into domains, hence it remains in a single domain state ( $D \leq D_s$ ), and in this state the particles have all the spins aligned in a single direction and are most desirable for the applications in magnetic recording media. The critical radius  $r_c$  below which a particle acts as a single domain particle [16] was found to be:

$$r_c \approx 9 \frac{(AK_u)^{1/2}}{\mu_0 M_s^2} \quad (1.10)$$

where  $A$  is the exchange constant,  $K_u$  is the uniaxial anisotropy constant and  $M_s$  is the saturation magnetization of the material. This single domain region can be further divided into two sub-regions the critical superparamagnetic size ( $D_p$ ) where,  $D_s \geq D > D_p$ , and the superparamagnetic sub-region where  $D < D_p$ . In this sub-region, the particles are so small that thermal energy is large enough to overcome the anisotropy energy, leading to zero coercivity, and the particles are in the so-called superparamagnetic state [13].

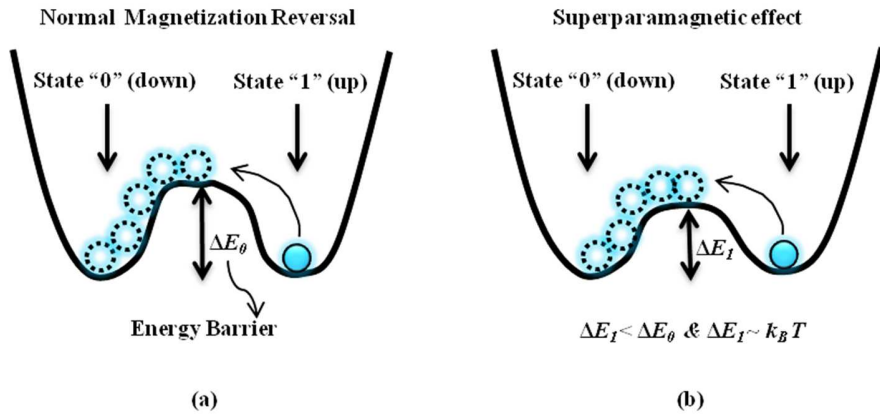


Figure 1.7 An illustration showing the difference in the energy barrier between the two possible magnetization states of a magnetic particle (a) before and (b) after the particle reaches a critical size for the onset of the superparamagnetic effect.

#### 1.4. Superparamagnetism and thermal stability

In 1949, Néel [17] pointed out that when a single domain particle is below a critical volume, thermal energy may be sufficient enough to reverse its magnetization from one easy direction to the other, even in the absence of an external bias field. This occurs if the total anisotropy energy of the particle,  $K_u V$ , is of the order of the thermal energy,  $k_B T$ . Here,  $K_u$  is the anisotropic energy density constant,  $V$  is the volume of the particle,  $k_B$  is the Boltzmann constant,

and  $T$  is the absolute temperature. The term “superparamagnetism” was coined by Bean to describe the behavior of single domain particle has a relatively enormous magnetic moment compared to that of an ion or atom in a normal paramagnet [18]. The magnetization behavior of an array of identical superparamagnetic particles can be described by the Brillouin function of a paramagnet, which has no magnetic hysteresis [19]. Figure 1.7 shows an illustration of this phenomenon. There are two possible magnetization states of a magnetic particle (up or down direction) occur at the two local minimum points in the energy axis of the particle. If the particle is in state “1” (up direction), a minimum energy of  $E_0$  is necessary in order for it to overcome the energy barrier to reverse its magnetization to state “0” (down direction). As the size of single domain particle decreases, the energy barrier will be lowered as well. At some point, the energy barrier will drop to a value comparable to the thermal energy, i.e.,  $\Delta E_1 \sim k_B T$ , and thermal fluctuations alone will be sufficient to reverse the magnetization of the particle. This energy barrier,  $\Delta E_0$ , associated with the spontaneous magnetization reversal process, is primarily determined by the magnetic anisotropy energy of the particles to be switched.

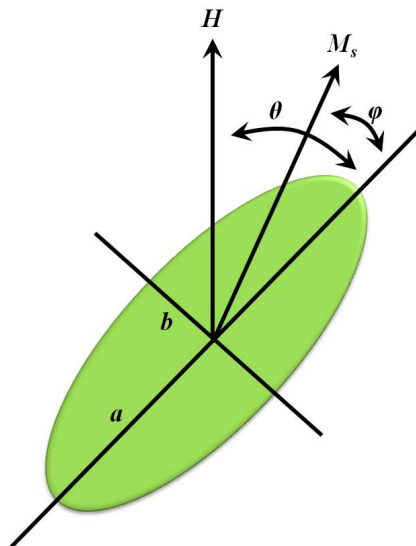


Figure 1.8 Illustration of a single-domain prolate spheroidal particle [19].

For recording media applications understanding, the magnetization reversal of small particles is critical. There are several models to explain this phenomena and one of the most important of them is from Stoner and Wohlfarth [20] describing the coherent rotation of the particle magnetization. In their model, a single domain prolate spheroidal particle as shown in the Figure 1.8 was considered. Without an external bias field, the particle will have its magnetization parallel to the easy axis which is the long axis, and its energy at a minimum [20]. When an external field,  $H$ , is at an angle,  $\theta$ , with respect to the easy axis is applied, the magnetization of the particle rotates towards the direction of the applied field. The energy of the particle is given by [19]:

$$\frac{E}{V} = K_u \sin^2 \phi - H M_s \cos(\theta - \phi) \quad (1.11)$$

where  $\phi$  is the angle between the direction of the applied field and the easy axis, and  $M_s$  is the saturation magnetization of the particle,  $V$  is the particle volume,  $K_u$  is the anisotropy constant.

If we now assume that the external applied field,  $H$  is parallel to the easy axis, but in the opposite direction to the initial magnetization, i.e.,  $\theta = \pi$ , then Equation 1.11 becomes:

$$\frac{E}{V} = K_u \sin^2 \phi + M_s H \cos \phi \quad (1.12)$$

the two local minimal of energy occur at  $\phi = 0$  ( $E_{min} = M_s H V$ ) and  $\phi = \pi$  ( $E_{min} = -M_s H V$ ). In order to determine the peak value of the energy barrier, we can set the derivative of (1.12) with respect to  $\phi$  equal to zero:

$$\frac{1}{V} \frac{dE}{d\phi} = 2K_u \sin \phi \cos \phi - M_s H \sin \phi = 0 \quad (1.13)$$

$$\cos \phi = \frac{M_s H}{2K_u}$$

substituting the above expression into equation (1.12), the energy density of the barrier is found to be [19]:

$$\frac{E_{\max}}{V} = K_u \left[ 1 + \left( \frac{M_s H}{2K} \right)^2 \right] \quad (1.14)$$

the energy barrier is given by the difference between the maximum and the minimum energy as:

$$\begin{aligned} \Delta E &= E_{\max} - E_{\min} \\ &= K_u V \left( 1 - \frac{M_s H}{2K} \right)^2 \\ &= K_u V \left( 1 - \frac{H}{H_0} \right)^2 \end{aligned} \quad (1.15)$$

where,  $H_0 = 2K_u/M_s$  is often known as the anisotropy field. From Eq. (1.15), we see that if the external applied field is equal to the intrinsic coercivity of the particle, i.e.,  $H = H_0$ , then the energy barrier goes to zero, i.e.,  $\Delta E = 0$ , and the minimum condition for magnetization reversal is satisfied. So the particle can change its state.

One other important aspect of magnetization reversal is the reversal due to thermal stability. Regardless, of magnetic particles interactions and the reduction of physical grain size, magnetically harder media materials will also have to meet the requirement of thermal stability. Unfortunately, thermal stability is a function of the grain size and grain size distribution. To estimate the minimal thermally stable grain size, one needs to make assumptions about the magnetization reversal and its thermal decay mechanisms. For a magnetic material with an anisotropy field in the easy axis along the unique crystalline axis, the particles have the magnetization either “up” or “down” along the easy axis. If a particle is magnetized in the “up” direction, it must surmount an energy barrier created by the magnetic anisotropy in order to move to the reversed “down” direction (see Figure 1.7). The magnitude of the barrier is given by

$K_u V$  where  $K_u$  is again the anisotropy constant of the material and  $V$  is the volume of the particle.

If this barrier is small enough, either  $K_u$  or  $V$  small, the particle may be induced to reverse magnetization spontaneously by thermal excitation. The frequency of magnetization reversal due to thermal excitation over a barrier height  $\Delta E$  is given by [13]:

$$f = f_0 e^{-\Delta E/kT} \quad (1.16)$$

where  $\Delta E = K_u V$  and  $f_0$  is a measure of the number of assaults, the magnetization makes on the barrier. However, for practical device applications one would like to know the measurable decay of magnetization in an ensemble of particles caused by thermally induced reversals, and this decay is, of course, directly related to the frequency of reversal of individual grains. The magnetization of an ensemble of particles at time  $t$  is given by

$$M(t) = M(0) e^{-t/\tau} \quad (1.17)$$

where  $\tau$  is the lifetime of the state of one of the particles. From Eq. (1.16), the decay time,  $\tau$ , is inversely related to the particle magnetization reversal frequency:

$$\tau = \frac{1}{f} = \frac{1}{f_0 e^{-\Delta E/kT}} \quad (1.18)$$

the minimum value of  $\Delta E/kT$  for a material to be a candidate for a magnetic medium is usually taken to be about 60 and  $f_0 = 10^9$ - $10^{11}$  s<sup>-1</sup> for 10 years of storage. The time dependent measurement on the remanent coercivity of magnetic media due to the thermal effects was first proposed by Sharrock [23]. In his model, the thermal relaxation of the magnetic particles remanent coercivity ( $H_{cr}$ ) decreases with an increase in the duration time of the applied field. The thermal stability factor,  $K_u V/k_B T$ , can be obtained from the formula for 3D randomly oriented particles as [23]:

$$H_{cr}(t) = H_0 \left[ 1 - \left[ \frac{k_B T}{k_u V} \ln \left( \frac{f_0 t}{\ln 2} \right) \right]^n \right] \quad (1.19)$$

where  $H_{cr}$  is the intrinsic coercive field for a random distribution of non-interacting particles with uniaxial anisotropy constant  $K_u$  and  $V$  is the particle volume. The exponent  $n$  depends on the model of the energy barrier ( $n = \frac{2}{3}$  for 3D random oriented particles). The attempt frequency,  $f_0$  is taken to be  $10^9 \text{ s}^{-1}$ .  $k_B$  is the Boltzmann constant and  $T$  is the absolute temperature.  $t$ , is the time needed for a constant field equaling to  $H_{cr}$  to reduce the magnetization from remanent saturation to zero. Accordingly, to avoid thermally induced switching of the particles, the anisotropy energy  $K_u V$  of each particle should be much larger than thermal energies,  $k_B T$ . A widely used rule to facilitate data retention of recording media is a thermal stability factor of  $K_u V > 60 k_B T$  [13, 22].

## 1.5. Magnetic particles for recording media

### 1.5.1. Metal based magnetic particles

Metal Particles (MP) are the most widely used particles in tapes today due to their high saturation magnetic moment and good thermal stability [24-27]. Several research groups have published details of advanced media fabricated using ultra-small particles and/or coatings, which are capable of supporting relatively high linear densities at very much reduced read track widths [24-27]. These media include advanced metal particle (MP) media that has been developed for use with GMR heads and that was reported to have the capability of supporting 15 Gb/in<sup>2</sup> with an advanced 35-nm-size fine metal particles [24]. In addition to the use of conventional MP-type particles, advances have also been made using other types of magnetic particles including nanosized composite advanced particles (NanoCAP). Dual coated ultrathin tape media fabricated using these particles have been reported to provide media with a smoother surface, reduced media noise, compared with conventional MP-based media, and a high SNR (signal to noise ratio).

More recently, still advances in media fabricated using improved Co-CoO metal evaporated (ME) tape has been described [27]. This media was evaluated using narrow read track-width GMR heads and found to have improved recording characteristics compared with previous ME media. The calculated SNR for this media, assuming partial response for equalization and a track pitch of 0.33  $\mu\text{m}$  was reported to be 19 dB, implying an areal recording density of 23.0 Gb/in<sup>2</sup>. One of the greatest drawbacks of using MP is susceptibility to oxidation and consequently degradation of saturation magnetization. A non-magnetic passivation layer, which is usually a 3 nm thick Y and Al surface coating layer, is required, to prevent the individual MP from corrosion and oxidation[28]. As particles become smaller, this passivation layer becomes a larger portion of the total volume, exceeding 50% in advanced MP. Therefore, the size reduction of MP size is restricted due to its lower effective particles size, and smaller shape anisotropy that effect thermal stability and recording density.

#### 1.5.2. Hexagonal barium ferrite particles and media properties

Highly advanced media fabricated using hexagonal barium ferrite ( $\text{BaFe}_{12}\text{O}_{19}$ ; H-BaFe) particles have been investigated for a number of years due to its high uniaxial magnetic anisotropy, excellent chemical stability, narrow switching field distribution (SFD), small transition region and no passivation layer [29–34]. H-BaFe has the same crystal structure as that of magnetoplumbite ( $\text{PbFe}_{7.5}\text{Mn}_{3.5}\text{Al}_{0.5}\text{Ti}_{0.5}\text{O}_{19}$ ), which consist of both the hexagonal closed-packed (HCP) and the face-centered-cubic (FCC) structures as shown in Figure 1.9. In the H-BaFe unit cell, the oxygen atoms are close-packed with the Ba and Fe ions in the interstitial sites. There are ten layers of oxygen atoms along the *c*-axis which is the magnetic easy axis. The structure is built up from smaller units: a cubic block *S*, having the spinel-type structure, and a

hexagonal block  $R$ , containing the Ba ions. The iron atoms are positioned at five crystallographically different sites of  $2a$ ,  $2b$ ,  $4f_{IV}$ ,  $4f_{VI}$ , and  $12k$ , respectively [35-36]. The structure is symbolically described as  $RSR^*S^*$  where  $R$  is a three-layer block, two  $O_4^-$  containing one  $BaO_3$  with composition  $(Ba^{2+}Fe_6^{3+}O_{11}^{2-})^{2-}$ , and  $S$  is a two  $O_4^-$  layer block with composition  $(Fe_6^{3+}O_8^{2-})^{2+}$ , where the asterisk means that the corresponding block has been turned  $180^\circ$  around the hexagonal  $c$ -axis.

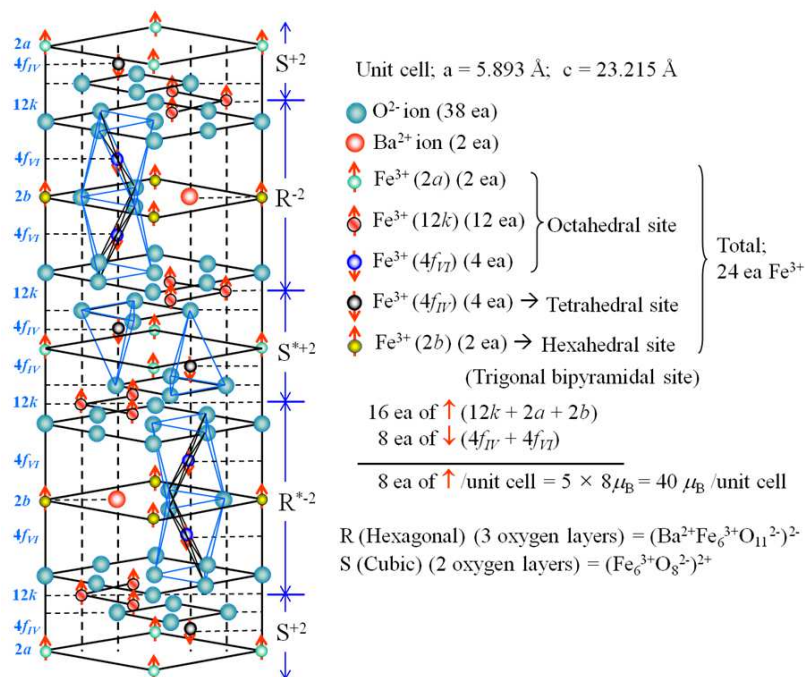


Figure 1.9 Magnetic structure of barium ferrite ( $BaFe_{12}O_{19}$ ,  $BaFe$ ) [36]

	2a	2b	4fIV	4fVI	12k
Position	Octahedral	Hexahedral	Octahedral	Tetrahedral	octahedral
Number of $Fe^{3+}$ ion/molecular	1	1	2	2	6
$K_1$ ( $cm^{-1}/ion$ )	0.23	1.40	0.18	0.51	-0.18
Spin direction	up $\uparrow$	up $\uparrow$	down $\downarrow$	down $\downarrow$	up $\uparrow$

Table 1.1 Barium ferrite magnetic site and calculated  $K_1$  for  $Fe^{3+}$  by single ion anisotropy model [12]

The smaller Fe<sup>3+</sup> ions are arranged in five different kinds of interstitial sites. Three are octahedral sites *12k*, *4fVI*, and *2a*, one is a tetrahedral site, *4fIV*, and the last one is a site in which the ferric ion is surrounded by five oxygen atoms forming a trigonal bipyramid, *2b*. Each crystal site has different number of Fe<sup>3+</sup> ion per molecular and single ion magnetocrystalline anisotropy [37], as shown in Table 1. Magnetocrystalline anisotropy of *2b* site has the highest value than that of other sites, so the magnetocrystalline anisotropy of BaFe can be modified by the addition of other dopant elements, such as Co<sup>2+</sup>, Ti<sup>4+</sup>, Sn<sup>2+</sup>, Nb<sup>4+</sup>, and Zn<sup>2+</sup> [38-45]. Moreover, the coercivity of BaFe particles originates from the magnetocrystalline anisotropy and the shape anisotropy based on the platelet shape as given below:

$$H_c = \alpha \left( \frac{K_1}{M_s} - \Delta N_d M_s \right) \quad (1.20)$$

therefore, the coercivity of BaFe can be altered by controlling the magnetocrystalline anisotropy. The origin of magnetocrystalline anisotropy is spin-orbit coupling and orbit-lattice coupling, but spin-spin coupling weakly contributes to the magnetocrystalline anisotropy because exchange energy between spins is isotropic. The magnetocrystalline anisotropy constant of BaFe is  $3.3 \times 10^6$  ergs/cm<sup>3</sup> [37]. The total magnetic moment of BaFe per molecular is 20 μ<sub>B</sub> because of 8 ions spin in one direction and 4 ions spin in the other direction, as shown in Figure 1.9. The saturation magnetization of BaFe at room temperature is 72 emu/g due to the orbital motion of the electrons, and the Curie temperature is 732 K.

### 1.5.3. Recording characteristics of H-BaFe media

The effects of particle size on the media properties, recording characteristics of H-BaFe have been discussed by Fujiwara for perpendicular recording media [116]. In his study, the saturation magnetization of the H-BaFe particle is affected by the aspect ratio (diameter (*D*) to

thickness ( $t$ ) and the nonmagnetic layer on the surface of the hexagonal platelets. If the particle volume is kept constant, larger aspect ratio particles provide smaller magnetization ( $M_s$ ), due to the existence of a magnetically inactive layer with a thickness “ $s$ ” on the  $c$ -plane surfaces given as  $M_s \propto (t - 2s) / t$ . Moreover, the packing density is also affected by aspect ratio; therefore larger aspect ratio reduces the packing density of the H-BaFe medium.

The coercivity is also affected by the particle aspect ratio and particle packing density. The demagnetizing factor “ $N_d$ ” in equation (1.20) is dependent on the particle aspect ratio  $D/t$ ; a larger aspect ratio particle provides a larger demagnetizing factor resulting in smaller coercivity. Moreover, particle-to-particle interaction also has to be taken into account. Particle stacking tends to occur, especially for large aspect ratio particles. The stacked particle assembly reduces its effective demagnetizing factor, since the effective aspect ratio becomes smaller, resulting in higher coercivity. Experimental data, showing the relationship between coercivity and packing fraction done by Fujiwara, showed that the coercivity increases due to particle stacking as particle concentration is increased. However, small aspect ratio particles showed a decrease in coercivity as the packing density is increased. The mechanism for this opposite behavior for small aspect ratio particles has not been clearly explained. However, it is considered that the different type of particle aggregation, other than stacking, are dominant for small aspect ratio particles. It was shown that the wavelength response is also affected by particle size. As the particle size becomes larger, the wavelength response becomes poorer. In addition to the above characteristics, it was shown that using smaller particles better wavelength responses and better signal to noise ratio were obtained [116].

Hexagonal barium ferrite with diameter to thickness ratios (aspect ratio) variable in the range of 3-10 and with typical diameters ranging from 100 nm to about 20 nm have been

established as a good competitor to the advanced MP media [24-34,42-53]. Early in the 1980's, Fujiwara and Kubo used 80 nm H-BaFe particles to demonstrate the recording performances of a perpendicular magnetic tape [46-47]. The tape had a saturation magnetization of 125 emu/cm<sup>3</sup>, and a coercivity of 1250 Oe, respectively. Recording properties of longitudinally oriented particulate media with H-BaFe and Fe based MP was studied by Speliotis [48-51] which showed a low level output at the low-density region of the BaFe media when compared to the MP media. This problem was solved in the 1990's with the development of the high sensitivity magnetoresistive (MR) or giant magnetoresistive (GMR) sensor recording head. Since then, a number of material processing and technologies helped H-BaFe to be a good competitor with MP. As discussed in earlier sections to improve recording density and performance of magnetic tape a smaller particle size is desired which raises the concern for the thermal stability of the magnetic particles [22]. Unfortunately, reduction of particle size for MP becomes challenging because of the risks of losing the high coercivity that is essential for high recording density due to the need for a non-magnetic passivation layer [28]. On the other hand, barium, ferrite increased coercivity is an added advantage by allowing extremely small particle sizes. This possibility is one of BaFe greatest attractions. In collaboration with IBM-Fujifilm developed advanced BaFe media with a recording density of 6.67 Gb/in<sup>2</sup>, by using 21 nm H-BaFe particles which is more than 15 times the recording density of an LTO generation 3 tape [30]. Also, employing a GMR head they were able to demonstrate an areal density of 15 Gb/in<sup>2</sup> [31]. In addition, studies at Fujifilm Corporation has proven that more than 30 year archival period is possible with Fujifilm's unique barium ferrite particles used for StorageTek T10000 T2 tape media [53]. Fujifilm has demonstrated the chemical stability and superior storage performance of H-BaFe as compared to other MP in extreme environmental conditions [54]. More recently, the

use of finer barium ferrite particles, improved particle dispersion, and orientation control has enabled up to 29.5 Gb/in recording densities [31-34]. Figure 1.10 shows the TEM images and the magnetic properties comparison of the H-BaFe particles employed by Fujifilm to achieve the recording densities of 6.7 Gb/in<sup>2</sup> and the 29.5 Gb/in<sup>2</sup> recording densities [30, 34, 55-56].

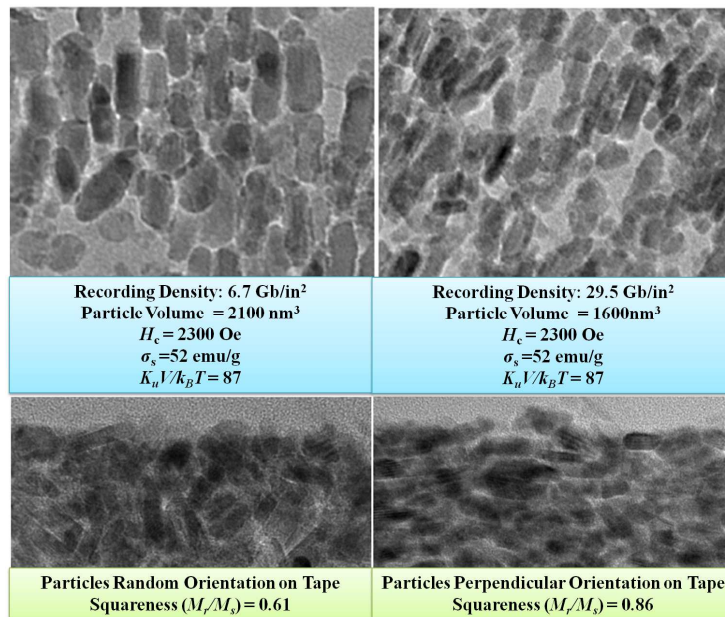


Figure 1.10 Advanced H-BaFe particles used by Fujifilm to achieve the recording densities of (a) 6.67 Gb/in<sup>2</sup> and (b) 29.5 Gb/in<sup>2</sup> [55-56].

Although, H-BaFe are continuing to show promising results to achieve higher recording densities compared to MP, the need for improving the medium noise, adequate SNR and dispersion of the particles is still an issue to be addressed [54-55,60-63]. Unfortunately, H-BaFe particles form poker-chip-like stacks due to mutual magnetic interaction during the dispersion process when making the magnetic tape for particulate recording media. Stacked H-BaFe particles make large unit volume in magnetization reversal process, thus stacked H-BaFe particles deteriorate recording capability because of large media noise, large surface roughness, poor recording resolution, and poor dispersion, as shown in Figure 1.11 [60-62, 106].

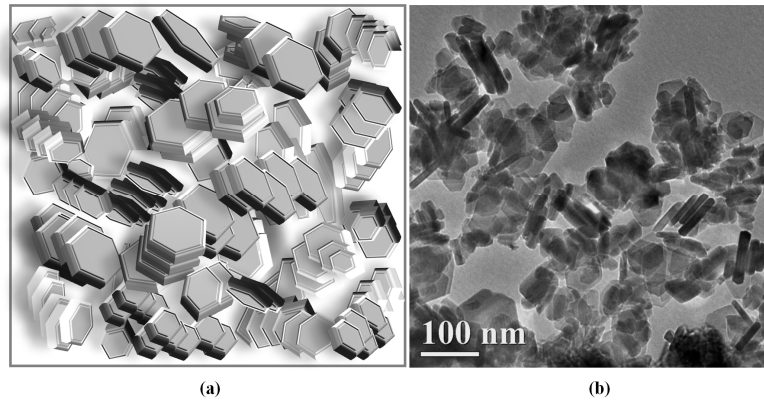


Figure 1.11 (a) Artist's drawings for particles dispersion of hexagonal shape [60-65] and (b) TEM micrograph of hexagonal barium ferrite.

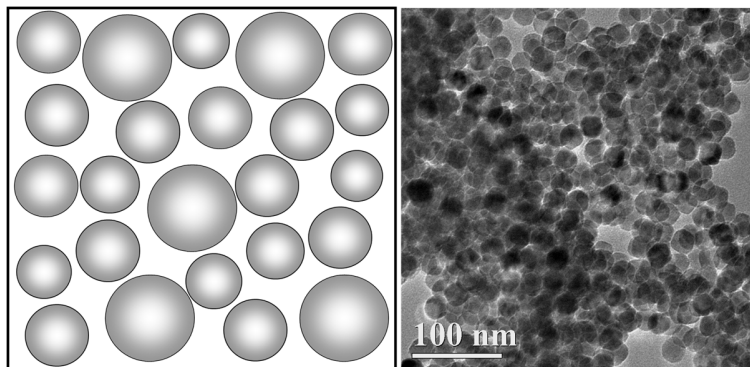


Figure 1.12 Artist's drawings for particles dispersion of spherical shape barium ferrite (S-BaFe) [60-62]

## 2.0. Objectives

One way to solve and improve the recording performance of H-BaFe media is employing substantially spherical barium ferrite (S-BaFe) particles. Spherical shaped particles have low aspect ratio 1:1 and only form a point-to-point contact, unlike the H-BaFe particles. Therefore, using S-BaFe particles not only decrease the degree of magnetic interaction between the particles but also can substantially increase the recording performance by improving the dispersion and SNR of the particles in magnetic media [60-62]. An artistic drawing showing the particles dispersion in spherical shaped barium ferrite is shown in Figure 1.12. Professor, Hong had previously developed S-BaFe particles that showed a weak magnetic particles-to-particle interaction ( $\Delta M$ ) by using 0.3  $\mu\text{m}$  sized S-BaFe particles [60-62]. Later, Dr. Gee from Prof. Hong's group was able to successfully synthesize 50- 60 nm S-BaFe which are still too big to meet the current requirements of high density recording media [64]. In this dissertation effort to further reduce the particle size of S-BaFe particles is studied and reported by using a unique adsorption-diffusion process. Two different approaches were used to achieve this objective.

First, 24-30 nm sized S-BaFe were synthesized from precursory nanosized spherical magnetite (S-Mag) [65] and cubic hematite nanoparticles ( $\alpha\text{-Fe}_2\text{O}_3$ ). The synthesis approach of the precursor nanoparticles was discussed in chapter 3 and chapter 4 followed by the adsorption-diffusion process in chapter 5. Secondly, in chapter 6 an alternative hydrothermal process was developed to synthesize S-BaFe nanoparticles that eliminate several processing steps used by the adsorption-diffusion process [66]. The as-synthesized S-BaFe particles from both the processes

have been evaluated for their magnetic and physical properties and the particles show promising results as future potential media for high density particulate recording.

### 3.0. Spherical magnetite nanoparticles (S-Mag)

#### 3.1. Introduction

Magnetite ( $\text{Fe}_3\text{O}_4$ ) nanoparticles have long been of scientific and technological interest because of their unique magnetic and electric properties [67-69]. The broad applications of magnetite nanoparticles include information storage [70], electronic devices [71], ferrofluid technology [72], catalysis [73] and pigments, etc. In particular, magnetite nanoparticles have attracted great attention for many important biomedical applications such as magnetic separation, drug delivery, cancer hyperthermia and magnetic resonance imaging (MRI) enhancement [74,75], due to their non-toxicity property [76] and high chemical stability. In this respect, magnetite nanoparticles are required to be water-soluble, monodisperse, superparamagnetic and easily to produce in large scale. To date, various techniques but most often chemical syntheses methods for preparing magnetite nanoparticles already have been reported, such as co-precipitation [77], micro-emulsions [78], solvothermal processing [79], and high-temperature organic phase decomposition [80-82]. As shown in Figure 3.1, magnetite, has an inverse spinel structure  $[\text{Fe}^{3+}]_A[\text{Fe}^{2+}\text{Fe}^{3+}]_B\text{O}_4$  with tetrahedral A sites and octahedral B sites [67]. It is a ferrimagnet and its conductivity results from the electron exchange between  $\text{Fe}^{2+}$  and  $\text{Fe}^{3+}$  ions.

#### 3.2. Experimental

For successful synthesis of S-BaFe particles the precursory spherical magnetite (S-Mag) particles shape, size and monodisperse nature is very important. We used a thermal decomposition method to synthesize monodispersed S-Mag nanoparticles developed by Park and

co-workers [82]. The synthesis process involved two steps. First an iron-oleate complex was prepared by reacting iron chlorides and sodium oleate, and secondly the decomposition of the iron-oleate complex in a high boiling point solvent in the temperature range between 240 and 320°C produced monodispersed S-Mag particles. The starting materials of Iron (III) chloride hexahydrate ( $\text{FeCl}_3 \cdot 6\text{H}_2\text{O}$ , 98 %), oleic acid (Aldrich, 90%), 1-octadecene (Aldrich, 90%, b.p. 317 °C) and sodium oleate (TCI, 95%) were used for the synthesis process with no further purification.

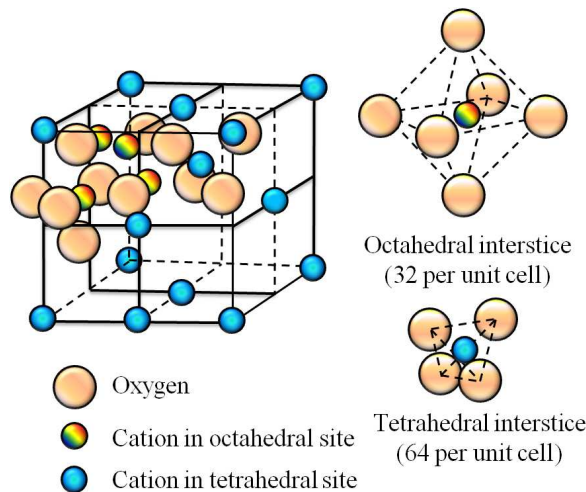


Figure 3.1 Spinel crystal structure [67].

The physical and magnetic properties of spherical magnetite were measured by several techniques. X-ray diffractometer (XRD) and transmission electron microscope (TEM) were used for measuring physical properties. Vibration sample magnetometer (VSM) was used to measure the magnetic properties of the as-synthesized nanoparticles and also Mössbauer spectroscopy was used to obtain the Mössbauer spectra of the nanoparticles. A brief description of the individual characterization methods used to evaluate both the precursory particles and the synthesized S-BaFe particles is given below.

X-ray diffractometer (XRD) is an efficient tool used to measure the crystalline phases, lattice constant, and miller indices of magnetic nanoparticles. XRD measurements were performed by a BRUKER D-8 ADVANCE system at room temperature. The magnetite nanoparticles were dispersed on a double sided tape which is pasted on a plastic sample holder puck and placed inside the slot allotted for measurement in the instrument. All the XRD scans were performed from 20-60° scan to obtain the data.

Morphology and particle size of magnetic nanoparticles were observed and estimated using an FEI TECNAI F20 transmission electron microscope (TEM). The nanoparticles were taken in a glass vial and were dispersed in a 100 % ethanol solution. The vial is then transferred into an ultrasonic water bath which operated at 40 kHz frequency to disperse the magnetic nanoparticles. A couple of drops of the dispersed particles is placed by using a glass pipette onto a 400 mesh Cu grid and it was allowed to dry to remove any organic content on the grid by placing on a hot plate. This grid containing the nanoparticles is used to observe the particles size and morphology under TEM.

The magnetic properties of nanoparticles were measured by a Model 1660 torque / vibrating sample magnetometer (VSM) from Digital Measurement System (DMS), ADE Technologies Inc. Magnetic nanoparticles were carefully put into a custom made cup style glass sample holder. Total weight of sample holder and nanoparticles was measured and then later subtracted the glass holder weight to get nanoparticles weight. The resonator in VSM oscillated with 75 Hz frequency in order to remove electrical interference with the normal 60 Hz of AC electrical frequency. The applied magnetic field was in the range of +10,000 Oe to -10,000 Oe. The magnetic moment was collected 100 times at each step of applied field and then made an average value to increase sensitivity of the magnetic moment.

Mössbauer spectra were obtained in constant mode at room temperature to observe the amount of  $\text{Fe}^{2+}$ ,  $\text{Fe}^{3+}$ , direction of spin, and magnetic hyperfine field. Sextets normally arise from the Mössbauer transition of the nucleus  $^{57}\text{Fe}$  in a magnetic field. A small distribution of magnetic fields contributing to one sextet can be taken into account by a correlated widening of the Lorentzian lines. The relative intensities of the Lorentzians are calculated under the assumption of a polycrystalline specimen.

### 3.2.1. Synthesis of iron oleate complex

The iron-oleate complex was first prepared by reacting 10.8 g of iron chloride (40 mmol) and 36.5 g of sodium oleate (120 mmol) in a solvent mixture composed of 80 ml ethanol, 60 ml distilled water and 140 ml hexane in a 1000 ml three neck bottom flask. The resulting solution was thoroughly stirred by using a magnetic stirrer bar and slowly heated to 70 °C by using a heating mantle with a temperature controller and kept at that temperature for 4 h. The solution turned in to a dark reddish organic complex. With no further delay, the organic complex is washed three times with 30 ml distilled water in a separatory funnel. The washing step is very critical to obtain the right iron-oleate complex. During the washing process ethanol and distilled water are collected as waste but the hexane remained in the iron-oleate complex is evaporated slowly by heating the three neck flask at 70°C until the iron-oleate complex turned into a dark waxy solid form.

### 3.2.2. Synthesis of magnetite nanoparticles

To the dark waxy solid formed 5.7 g of oleic acid (20 mmol) was added with 200 g of 1-octadecene at room temperature. This solution is then slowly heated at the rate of 3.2°C/min

using a temperature controller to 320 °C, and then kept at that temperature for 30 min. When the reaction temperature reached 320 °C, a severe reaction occurred and the initial transparent solution became turbid and brownish black in color. The resulting solution containing the nanocrystals was then cooled down to room temperature, and washed with a combination of ethanol and hexane to precipitate the magnetite nanoparticles. The washed and precipitated particles were then dried in an oven at 80 °C for 4 h. Figure 3.2 shows the flowchart and the experimental setup used to synthesis the S-Mag nanoparticles. The effect of using different solvents with respect to the size and shape of the S-Mag nanoparticles was also studied by using solvent solutions such as 1-eicosene (TCI, b.p. 330 °C) and trioctylamine (TCI, b.p. 365 °C) apart from 1-octadecene (Aldrich, 90%, b.p. 317 °C).

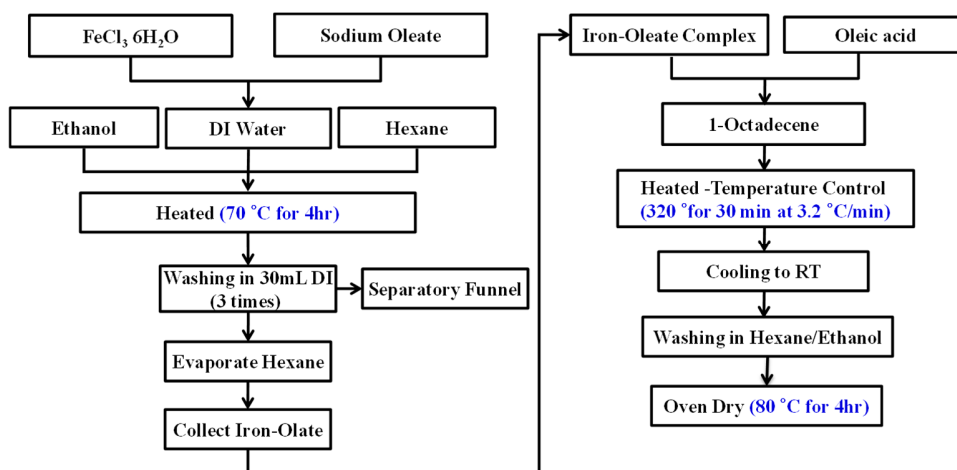


Figure 3.2 Flowchart and the experimental setup used to synthesise S-Mag nanoparticles.

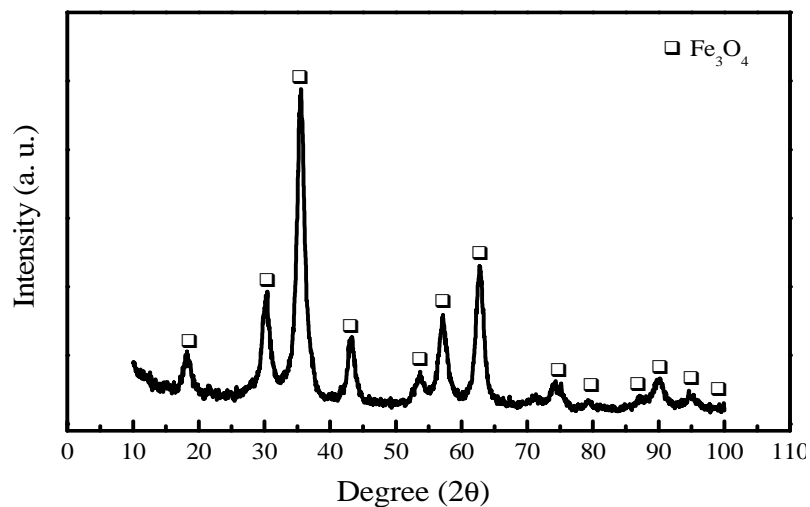


Figure 3.3 XRD patterns of spherical magnetite nanoparticles at room temperature.

### 3.3. Results and discussion

The collected magnetite particles ranged from 7- 30 nm depending on the decomposition temperature and aging period. In this synthesis process, aging was found to be a necessary step for the formation of iron oxide nanoparticles. Figure 3.3 shows the XRD patterns of the as-synthesized S-Mag nanoparticles revealing the cubic spinel structure of magnetite. The particle size and morphology of the magnetite nanoparticles was determined by FEI TECNAI F20 transmission electron microscope (TEM). Figure 3.4 shows the as-produced TEM images of the magnetite nanoparticles synthesized by using 1-octadecene as the solvent. The particles sizes ranged from 7-30 nm and are well-dispersed and are in spherical morphology. It was also found that by using other high boiling solvents such as 1-eicosene (TCI, b.p. 330 °C) and trioctylamine (TCI, b.p. 365 °C) the spherical morphology of the particles was not retained and also the particle size increased as shown in Figure 3.5 (a) and (b) respectively. This non-uniform size

and shape distribution of the particles can be explained by the higher reactivity of the iron-oleate complex in the solvent with a higher boiling point.

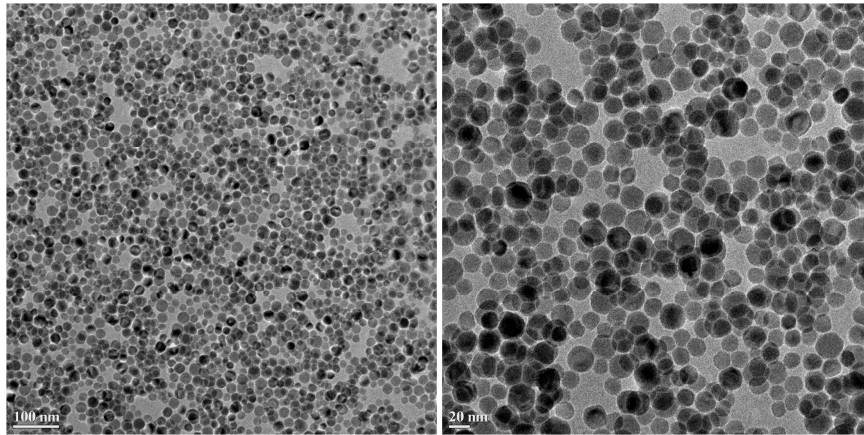


Figure 3.4 TEM micrographs of S-Mag nanoparticles.

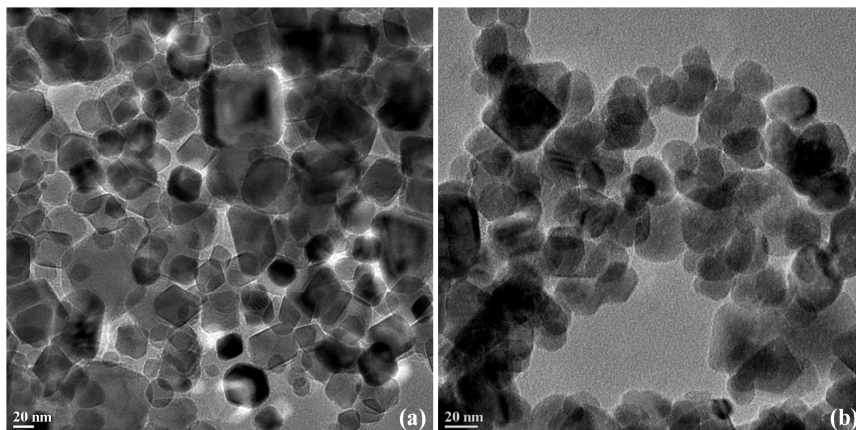


Figure 3.5 TEM micrographs of the S-Mag nanoparticles synthesized from (a) 1-eicosene and (b) trioctylamine solvents respectively.

Figure 3.6 shows the magnetic hysteresis curve of the as-synthesized S-Mag nanoparticles. The coercivity of these magnetite nanoparticles are nearly 0 Oe, as compared to the bulk value of 115-150 Oe [83]. This is due to the superparamagnetic behavior of nanosized spherical magnetite particles. The observed saturation magnetization ( $\sigma_s$ ) of the as-synthesized magnetite particles was 70 emu/g at room temperature, which is smaller than the bulk value of

92 emu/g [83]. This lower magnetization might be attributed to the smaller particle size that decreases the magnetic moment of the particles. To further confirm the superparamagnetic behavior of the spherical magnetite nanoparticles, Mössbauer spectra were obtained as shown in Figure 3.7. A large singlet spectrum was observed at room temperature, implying almost 50 % of the particles exhibit superparamagnetic behavior.

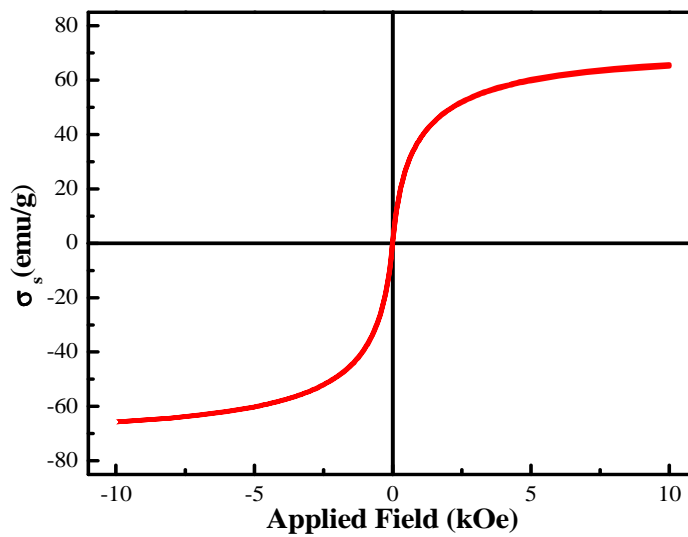


Figure 3.6 Magnetic hysteresis loop of as-synthesized S-Mag nanoparticles.

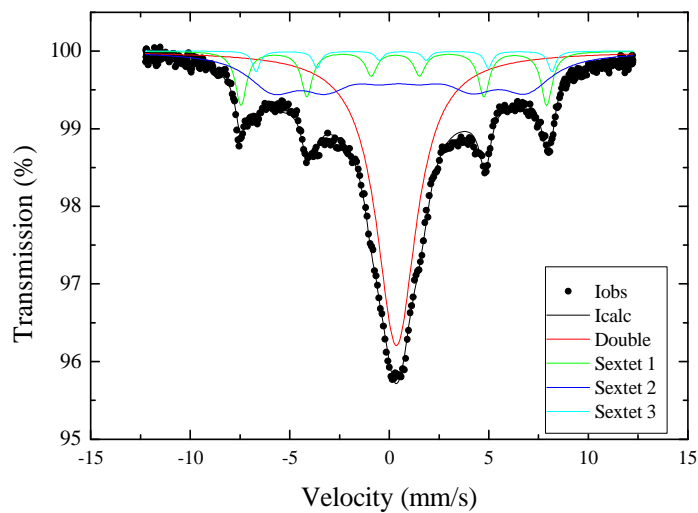


Figure 3.7 Mössbauer spectra of S-Mag nanoparticles.

## 4.0. Hematite nanocubes

### 4.1. Introduction

Hematite ( $\alpha\text{-Fe}_2\text{O}_3$ ) is the most stable iron oxide under ambient conditions and is commonly found in nature [84-86]. Its magnetic properties have been studied extensively both in bulk form and in the form of ultrafine particles [86]. Hematite ( $(R\bar{3}C$  or  $D_{3d}^6$ ); space group) has a corundum crystal structure, which can be indexed either rhombohedra ( $a = b = c$ ,  $\alpha = \beta = \gamma \neq 90$ ) bravais lattice or approximately a hexagonal lattice [84-85]. The unit-cell of hematite is shown in Figure 4.1, viewed in the [001] direction looking down the  $c$ -axis, with the basal plane in the plane of the page, and in the [110] direction, looking at the prism planes. In the unit cell, the Fe ions lie in the basal planes, with only two of three sites intersecting the  $c$ -axis being occupied. These  $c$ -axis pairs form iron bilayers within the crystal and have the smallest cation-cation separation [84-86]. The oxygen ions form distorted octahedra around the Fe ions. The deviation from the ideal hexagonal structure is visible when the unit cell is viewed in the [001] direction as shown in Figure 4.1.

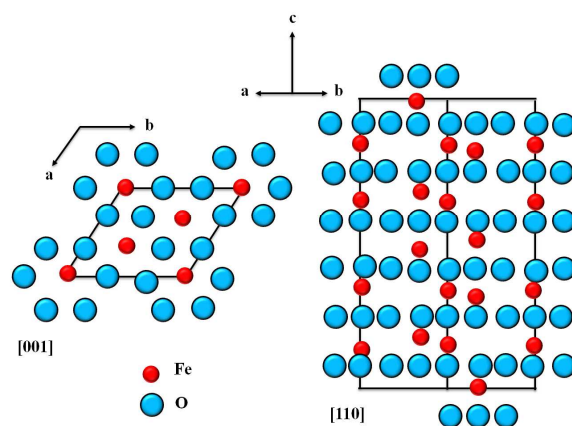


Figure 4.1 Unit cell of hematite viewed in the [001] and [110] directions [84-85].

Hematite can exhibit both ferromagnetic and antiferromagnetic behavior. A ferromagnetic material has a spontaneous magnetic moment, with electron spins aligned in a regular fashion with neighboring spins in one direction. In the case of antiferromagnetism, the electron spins are regularly aligned, but neighboring spins point in opposite directions. The iron atoms in the (001) basal planes of hematite are coupled ferromagnetically, and iron atoms in successive planes in the [001] direction are coupled antiferromagnetically [87-92]. Between 260 K and 950 K, hematite exhibits weak ferromagnetism due to slight spin canting (spins nearly in the basal plane). Below 260 K hematite is antiferromagnetic with the spins parallel to the c-axis. The Néel temperature (point at which the thermal energy is large enough to destroy the magnetic ordering of an antiferromagnetic material) is around 950 K for hematite. The Néel temperature is analogous to the Curie point, the temperature above which a ferromagnetic material loses its magnetic ordering [87-92].

Recently, nanoscale synthesis of hematite nanoparticles with different shapes and sizes has received great attention due to their unique properties which are different from the corresponding bulk materials. Many studies have been reported on the synthesis of hematite particles [92–104]. These studies show that the size and shape of the hematite particles strongly depends on factors, such as the concentration of  $\text{Fe}^{3+}$  ions, additives, pH, temperature, and aging time respectively. Moreover, particles synthesized with sol-gel, template, thermal oxidation, thermal synthesis all have produced particles with non-uniform size and shape distribution. On the other hand, hydrothermal precipitation method to produce monodisperse  $\alpha\text{-Fe}_2\text{O}_3$  particles of uniform shape, size, and composition, proved to be very effective. Hydrothermal precipitation method had received greater attention because this technology has several advantages such as

fast reaction time, effective control of particle shape, and low incorporation of impurities into the particles [102–104].

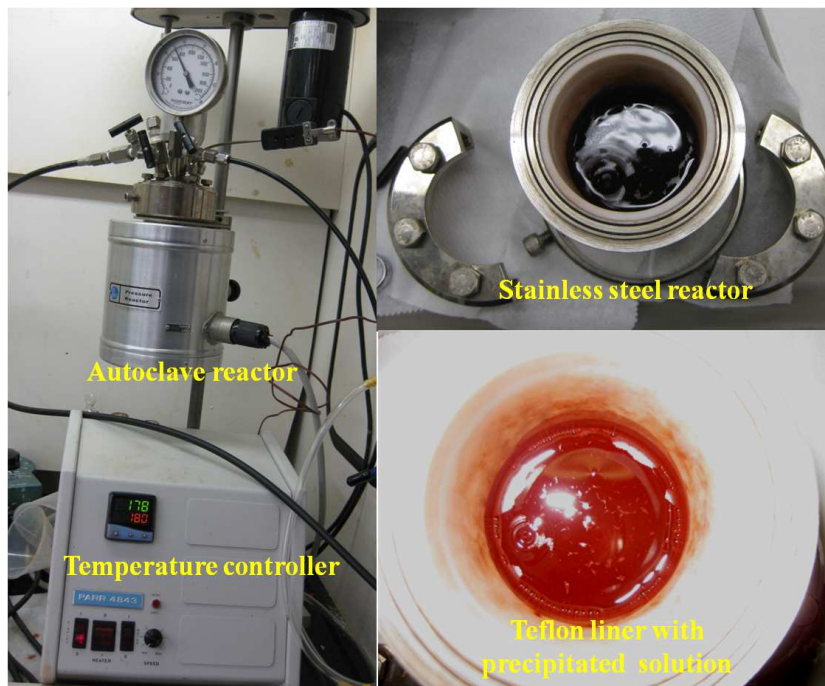
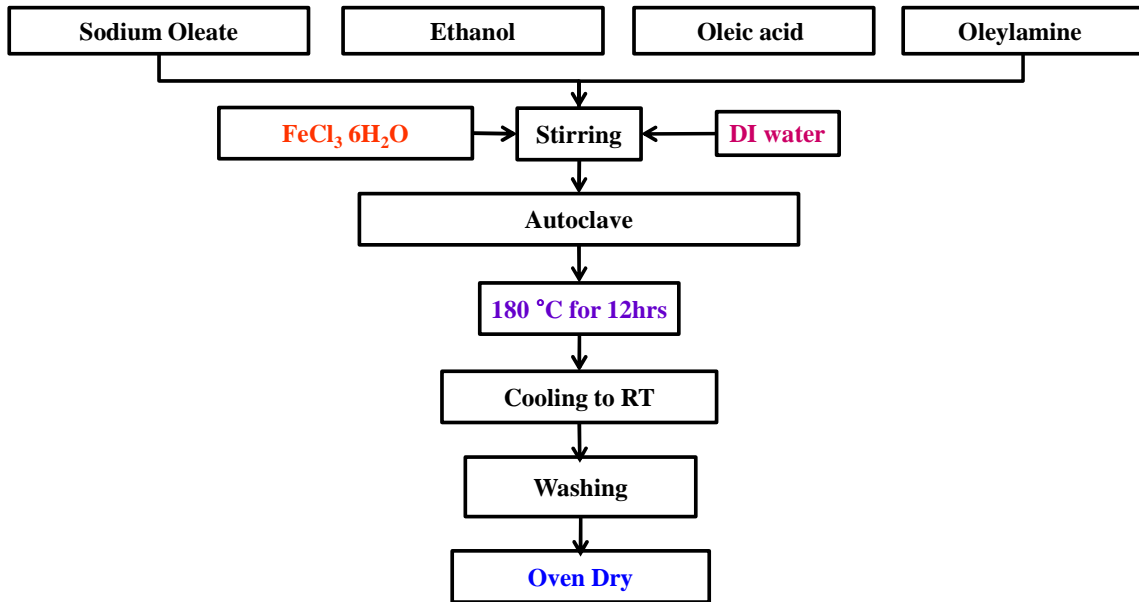


Figure 4.2 Flowchart and the experimental setup used to synthesize hematite nanocubes.

## 4.2. Experimental

Similar to the spherical magnetite particles synthesis the cubic hematite nanoparticles shape, size and monodisperse nature is critical for a successful synthesis of spherical barium ferrite particles. In order to synthesize uniform hematite nanocubes, we have modified and optimized the process developed by Wang and coworkers [104]. They used a hydrothermal process which resulted in uniform hematite nanocubes with an average size of 15 nm but a size screening process was needed to separate the crystals. Moreover, the production capacity was as small as 0.11 g/batch. With the modifications, we were able to scale-up the process to produce hematite nanocubes with uniform shape and narrow size distribution [105-107]. Figure 4.2 shows the flowchart and the experimental setup used to synthesis the hematite nanocubes. The average size of hematite nanocubes was 21 nm with an extremely narrow particle size distribution and uniform cubic shape. Production capacity was increased to 2.0 g/batch while maintaining antiferromagnetic properties of the nanocubes.

The raw materials used for the synthesis process are iron (III) chloride hexahydrate ( $\text{FeCl}_3 \cdot 6\text{H}_2\text{O}$ , 98 %), oleic acid (Aldrich, 90%), oleylamine (Aldrich, 90%) and sodium oleate (TCI, 95%) with no further purification. In a typical process, 7.6 g of  $\text{FeCl}_3 \cdot 6\text{H}_2\text{O}$  and 22.0g of sodium oleate are weighed accurately in a 250 ml Teflon liner container. To this mixture 60 ml of deionized water, 60 ml of ethanol and 60 ml oleylamine was added and mixed with a magnetic stirrer on a hot plate for 2 h. After continuous vigorous stirring for 2 h, a semi-thick metal oleate complex is formed in water. This complex inside the Teflon liner is placed in a stainless steel autoclave (Parr Instrument Company) and heated with a temperature controller to 180 °C and held for 12 h to obtain a reddish brown precipitate at the bottom of the Teflon liner. This

precipitate after cooled down to room temperature is washed several times with a combination of hexane and ethanol and dried in an oven at 80 °C for 6-10 h to obtain the nanocubes.

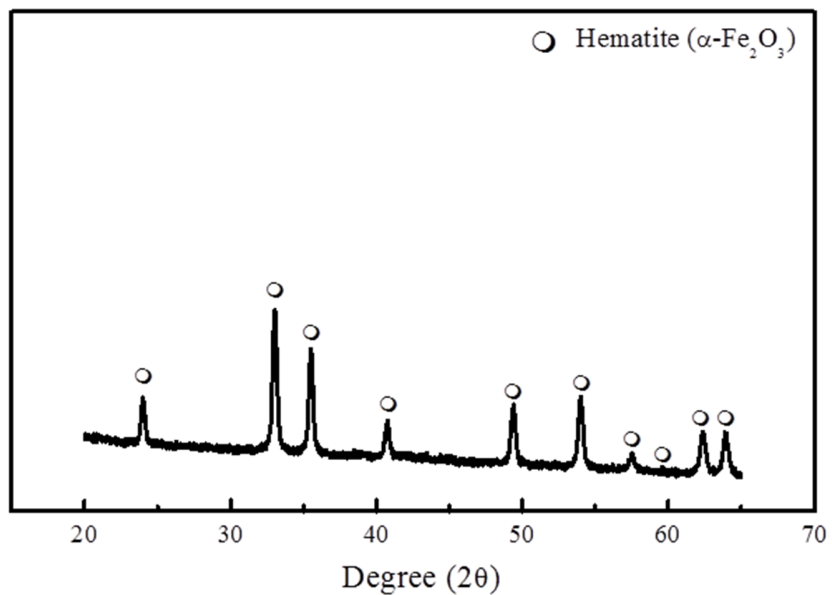


Figure 4.3 XRD patterns of hematite nanocubes at room temperature.

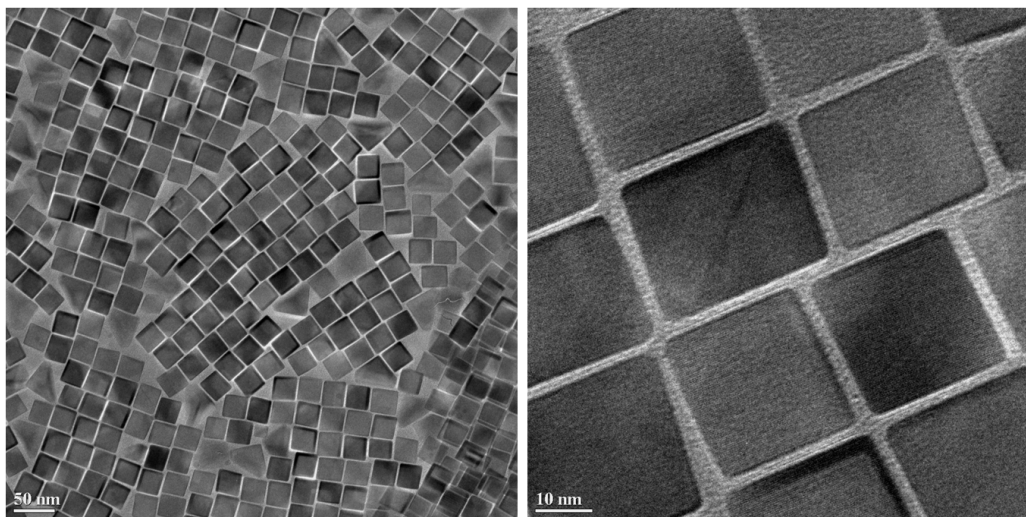


Figure 4.4 TEM micrographs of the as-synthesized hematite nanocubes.

### 4.3. Results and discussion

Figure 4.3 shows the XRD patterns of the as-produced hematite ( $\alpha$ - $\text{Fe}_2\text{O}_3$ ) nanocubes. The recorded and indexed diffraction pattern coincides with the peaks characteristic of the hematite phase. The particle size and morphology of the hematite nanoparticles was determined by FEI TECNAI F20 transmission electron microscope (TEM). Figure 4.4 shows the as-produced TEM images of the hematite nanocubes. The particles sizes ranged from 20-25 nm and are well-dispersed and are in cubic morphology. It was found that in order to obtain uniform hematite nanocubes the concentration ratio of  $\text{FeCl}_3$ /sodium oleate (CFe/SO) plays a major factor. A set of experiments were performed by keeping the sodium oleate concentration fixed at 22.0 g but varying the  $\text{FeCl}_3$  amount from 5 to 11 g which gives the concentration ratio of CFe/SO = 0.22 to 0.50. When CFe/SO is lower than 0.25 the product mainly consists of zero-dimensional nanoparticles scattered in a form of matrix as shown in Figure 4.5(a), which implies that the precursors possibly are nuclei of hematite surrounded by oleate surfactants of several nanometers. With a gradual increase of the concentration of  $\text{FeCl}_3$ , the shapes of the synthesized products turn to cubic at CFe/SO = 0.34 as seen in the Figure 4.5 (b), with further increase in the concentration ratio pseudo cubic and pseudo spherical shaped particles are formed with an increased particle size from 21 nm to 60 nm as seen in the Figure 4.5 (c) and Figure 4.5 (d), respectively. Thus, different morphologies of  $\alpha$ - $\text{Fe}_2\text{O}_3$  nanoparticles were obtained by varying the CFe/SO ratio from 0.20 to 0.50. The ratio of CFe/SO = 0.34 gave the best results with uniform hematite nanocubes between the size ranges of 20-25 nm. The increased particle size at higher CFe/SO concentration ratio may be attributed to the lower sodium oleate content in the reaction per  $\text{Fe}^{3+}$  ions that cannot inhibit the growth rate of the final hematite crystal formed suggesting an increase in the particle size and shape respectively.

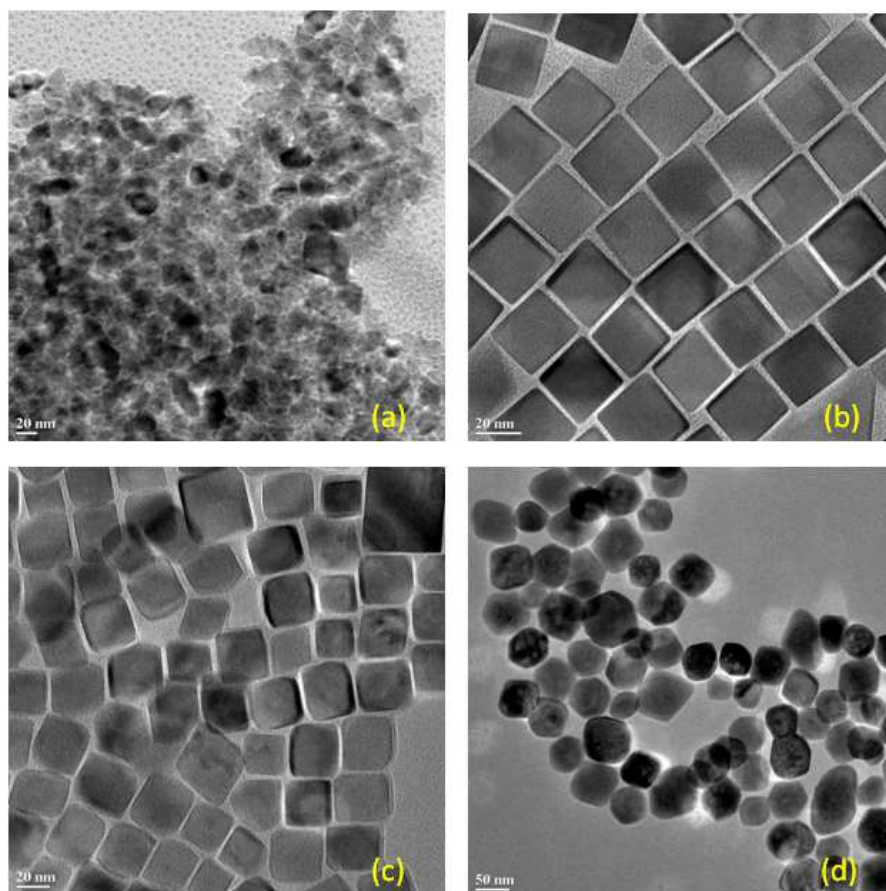


Figure 4.5 TEM images of the hematite products obtained with  $\text{FeCl}_3$ / sodium oleate (CFe/SO) ratio (a) CFe/SO = 0.22 (b) CFe/SO = 0.34 (c) CFe/SO = 0.40 and (d) CFe/SO = 0.50.

Magnetic hysteresis loops were obtained for the as-synthesized hematite nanocubes by using a VSM at room temperature. Figure 4.6 shows the hysteresis loops of the hematite particles synthesized with various CFe/SO ratios. For particles with CFe/SO = 0.22 a saturation magnetization ( $\sigma_s$ ) and coercivity ( $H_c$ ) values of 0.45 emu/g and 55 Oe at 10 kOe, are obtained. On the other hand, for particles obtained with CFe/SO = 0.50 a saturation magnetization ( $\sigma_s$ ) and coercivity ( $H_c$ ) values of 1.09 emu/g and 124.41 Oe at 10 kOe, are obtained. This increase in the  $\sigma_s$  and  $H_c$  values is mainly attributed to the increasing volume of the particles with respect to the shape and size respectively as confirmed from the TEM images. Figure 4.6 (b) shows the

hysteresis loop of 20-25 nm (CFe/SO = 0.34) hematite nano cubes with a saturation magnetization ( $\sigma_s$ ) and coercivity ( $H_c$ ) values of 0.47 emu/g and 77 Oe respectively.

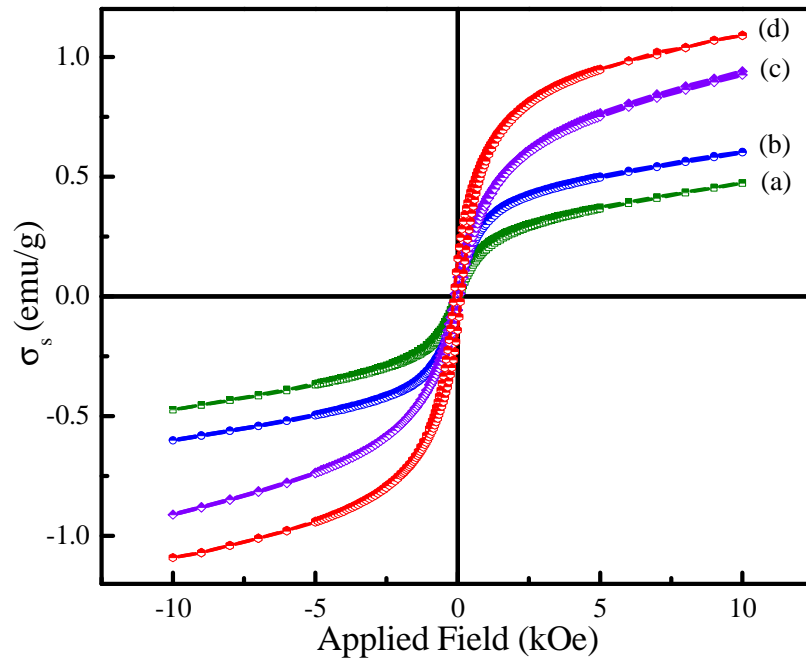


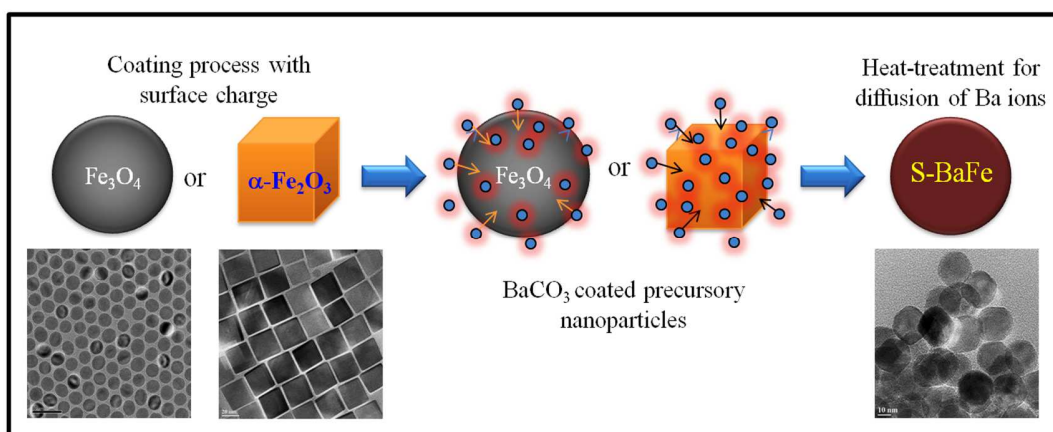
Figure 4.6 Room-temperature hysteresis loops of the hematite particles with FeCl<sub>3</sub>/sodium oleate (CFe/SO) ratio (a) CFe/SO = 0.22 (b) CFe/SO = 0.34 (c) CFe/SO = 0.40 and (d) CFe/SO= 0.50.

## 5.0. Spherical barium ferrite (S-BaFe)

### 5.1. Introduction

Spherical barium ferrite particles (S-BaFe) were synthesized using the precursors of spherical magnetite (S-Mag) and hematite nanocubes described in the previous two chapters. Also, a successful attempt was made to produce S-BaFe nanoparticles by developing a new hydrothermal process by eliminating the steps and expenditure involved to produce the precursory particles of S-Mag and hematite nanocubes.

Step I: Adsorption of Ba-carbonate on hematite nanocube or spherical magnetite particle



Step II: Diffusion of barium into hematite nanocube or spherical magnetite particle to form spherical barium ferrite nanoparticles

Figure 5.1 Experimental process for the synthesis of S-BaFe nanoparticles

### 5.2. Experimental

Well-dispersed spherical magnetite (S-Mag) which were synthesized by decomposition of the iron-oleate complex in a high boiling point solvent and 20-25 nm sized uniform hematite

nanocubes synthesized by a modified hydrothermal process were used as the precursors to synthesize S-BaFe nanoparticles [105-107]. The conversion process can be divided into two steps as shown in Figure 5.1. First, adsorption of BaCO<sub>3</sub> onto S-Mag or cubic hematite particles and secondly, diffusion of barium ions into the precursory particles of S-Mag or cubic hematite particles by heat-treatment to form S-BaFe nanoparticles. In a typical process, a colloidal BaCO<sub>3</sub> is prepared by adding Ba(NO<sub>3</sub>)<sub>2</sub> to a solution comprising of 100 ml ethanol (200 % proof) and 100 ml deionized water (VWR 18 Ωcm<sup>-1</sup>) in a 500 ml beaker. This solution is mechanically stirred at 500 rpm for 2-4 h so that the Ba(NO<sub>3</sub>)<sub>2</sub> is completely dissolved. Later, NaOH, with 50 ml deionized water and 50 ml ethanol is added and vigorously stirred for another hour. Carefully cleaned and dried precursory particles of Fe<sub>3</sub>O<sub>4</sub> or cubic hematite are weighed and slowly added to the solution while maintaining continuous stirring. The solution is further stirred for an hour before adding Na<sub>2</sub>CO<sub>3</sub> with additional 50 ml deionized water and 50 ml ethanol to bring the final volume to 400 ml as shown in the process flow chart of Figure 5.2. Sometimes additional (~100 ml) of the DI water is added. At this point, the beaker is sealed with parafilm tape and the solution is vigorously stirred for 12h to improve dispersion of the precursory particles in the solution as shown in Figure 5.2.

Finally, after the coating process completed, the mechanical stirrer is stopped, and the colloidal dispersion is left idle for few minutes. A precipitate containing the coated precursory particles slowly settled down at the bottom of the beaker. This precipitate is carefully collected by filtering using a Whatman® 541 and 42 (24cm diameter) filter paper by drying in an oven to collect the particles. When dried, a thin sheet of white precipitate like matrix containing the precursory particles was collected from the filter paper which is later ground in a mortar and pestle for annealing at various temperatures in the range of 700–900 °C for 1–2 hr in a tube

furnace with oxygen atmosphere. Heat-treatment conditions and mol ratio of composition were optimized by considering both magnetic and physical properties of S-BaFe particles. It is important that the precursory particles be well dispersed in the solution to obtain good S-BaFe particles. Ethanol played a significant role in the process of dispersion of the magnetite and hematite precursor particles. During the later runs to optimize the process further the particles containing the solution is sometimes placed in an ultrasonic bath to disperse the particles occasionally and mechanically stirred again. These particles were oven dried at 80 °C for 12 h and heat-treated

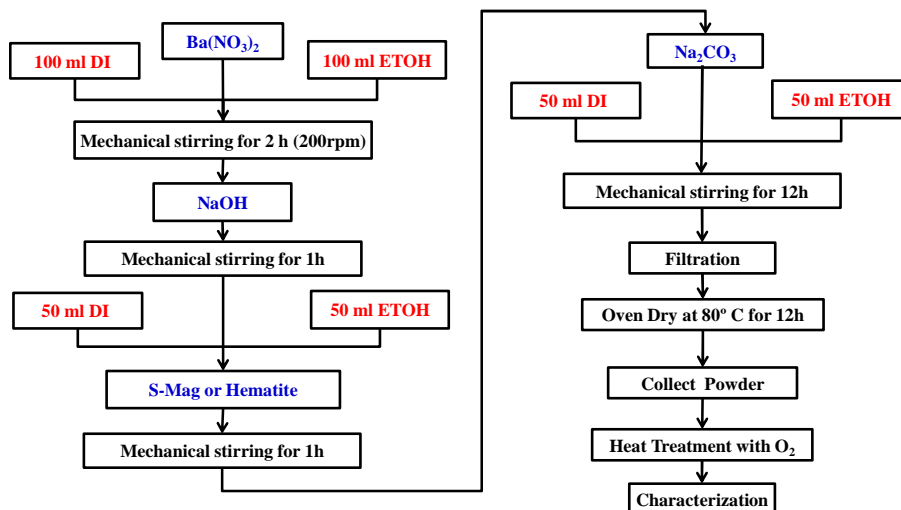


Figure 5.2 Flowchart and the experimental setup used to synthesize S-BaFe nanoparticles.

Remanence curves and  $\Delta M$  plots were used to study the magnetic interactions between the S-BaFe particles by using vibration sample magnetometer (VSM). There are two basic remanence curves: the isothermal remanence curve (IRM) and the DC demagnetization curve (DCD). The IRM is measured on previously demagnetized particles. The particles are then subjected to a positive applied field at which point the magnetization is measured. The applied field is then removed, and the remanent magnetization is measured. The cycle is then repeated, incrementing the positive applied field until saturation is reached. Plotting  $M_r$  against the previously applied positive field  $H$  gives the IRM curve. The DCD remanence curve is measured similarly by first saturating the sample in a positive applied field and then applying a known reverse field at which point a measurement is taken. The reverse field is then reduced to zero, and the remanent magnetization is measured. The process is then cycled with an incremented reverse field until negative saturation is reached. The relationship between IRM and DCD for an assembly of non-interacting single domain particles is given by Stoner-Wohlfarth as  $\Delta M = \text{DCD} - (1 - 2(\text{IRM}))$  [20]. The  $\Delta M$  curves for the as-synthesized S-BaFe particles were plotted by using the VSM which gives us valuable information on the mutual magnetic interactions between the particles. For the measurement, S-BaFe nanoparticles were embedded in a non-magnetic paraffin wax and melted the wax at 60 °C while applying a field of 10 kOe. This process allowed the S-BaFe particles to align themselves in the applied field direction and stay in that direction on cooling to room temperature. Moreover, the thermal stability  $K_u V/k_B T$  for the S-BaFe nanoparticles was also determined by using the DCD remanence curves at different time scales of an applied field by using VSM. Microstructure, particle size, and particle size distribution of the S-BaFe nanoparticles were observed by X-ray diffraction pattern (XRD) and transmission electron microscope (TEM) at the room temperature. Magnetic properties of S-

BaFe particles were determined by VSM and also Mössbauer spectra of the S-BaFe were measured.

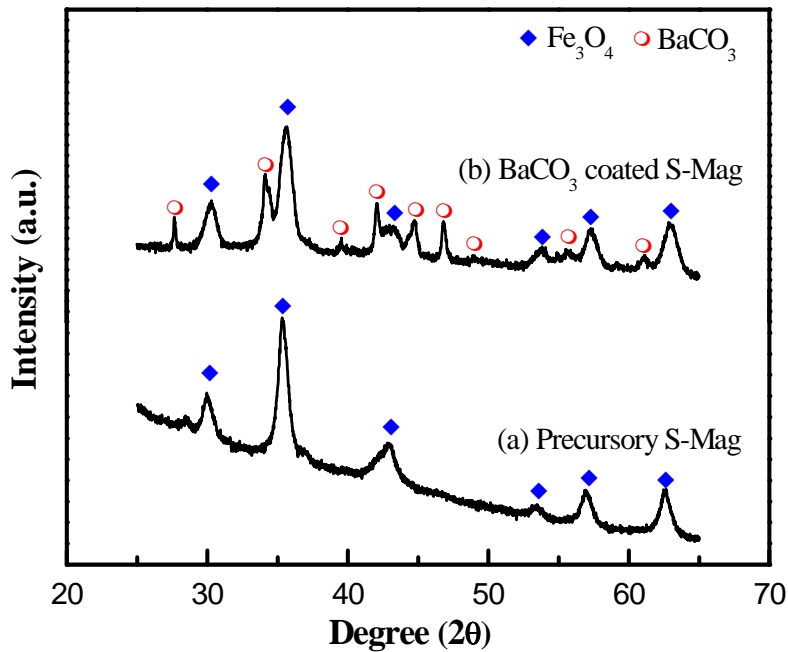
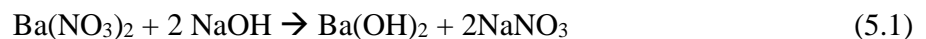


Figure 5.3 XRD patterns of the as-collected S-Mag nanoparticles (a) before BaCO<sub>3</sub> coating and (b) after BaCO<sub>3</sub> coating onto the S-Mag particles respectively.

### 5.3. Results and discussion

#### 5.3.1. S-BaFe synthesized from S-Mag precursor particles

The Ba(NO<sub>3</sub>)<sub>2</sub> dissolved in deionized water, and the ethanol solution reacts with the NaOH to form Ba(OH)<sub>2</sub>. The chemical reaction involved in the formation of Ba(OH)<sub>2</sub> can be represented as below:



it was previously determined that the iron oxide particle have a negative surface charge in the base region, and the precipitated Ba(OH)<sub>2</sub> particle have a positive charge in the base region [108]. While both the particles are suspended in the solution, they are attracted to each other and,

as a result, the absorption of  $\text{Ba}(\text{OH})_2$  particles onto the S-Mag particles surface is achieved. To obtain colloidal  $\text{BaCO}_3$  the particles that are already coated with the  $\text{Ba}(\text{OH})_2$  are reacted with  $\text{Na}_2\text{CO}_3$  to form  $\text{BaCO}_3$  colloidal particles coated on top of the S-Mag nanoparticles. The chemical reaction involved in the formation of  $\text{BaCO}_3$  can be represented as below:

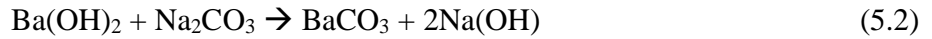


Figure 5.3 shows the XRD patterns of S-Mag ( $\text{Fe}_3\text{O}_4$ ) particles before and after  $\text{BaCO}_3$  coating process. Fig. 5.3 (b) clearly shows the extra peaks that correspond to  $\text{BaCO}_3$  phase. This confirms that the S-Mag particles are uniformly coated with the  $\text{BaCO}_3$  phase which will affect the subsequent conversion process to S-BaFe particles.

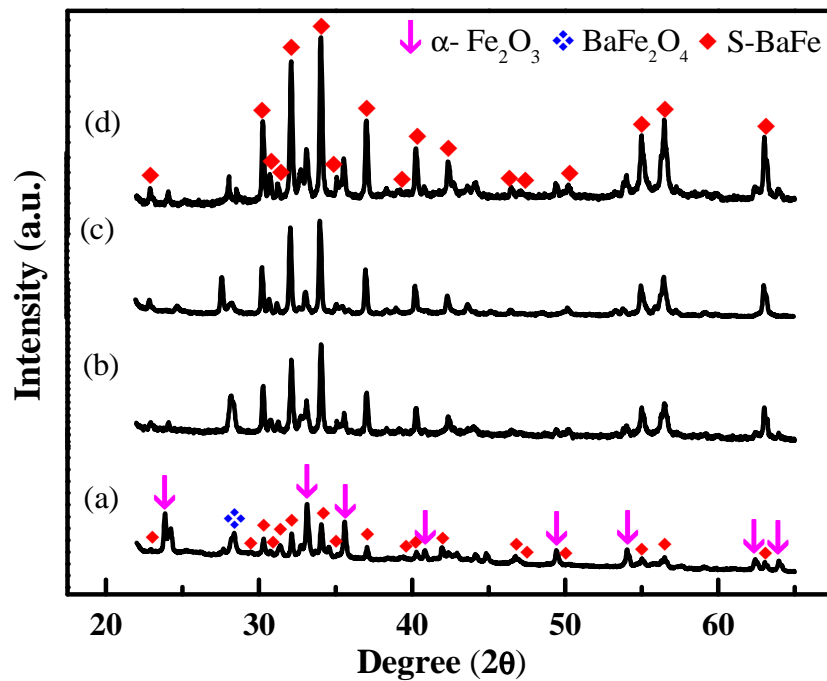


Figure 5.4 XRD patterns of S-BaFe as a function of various heat-treated temperatures; (a) 650 °C for 2 h, (b) 700 °C for 2 h, (c) 800 °C for 2 h, and (d) 900 °C for 2 h.

With regard to conversion of S-Mag to S-BaFe, the BaCO<sub>3</sub> coated S-Mag are heat-treated at various temperatures between 650-900 °C under oxygen atmosphere. During the heat-treatment process barium ions (Ba<sup>2+</sup>) in colloidal form diffuse into magnetite particle to convert to BaFe particles. It is well-known that Fe<sub>3</sub>O<sub>4</sub> can be oxidized to γ-Fe<sub>2</sub>O<sub>3</sub>, which can be further transformed into α-Fe<sub>2</sub>O<sub>3</sub> at a higher temperature [83]. It has been previously reported that the formation mechanism of barium ferrite by the solid state reaction takes place in two different steps [109]. First, the BaCO<sub>3</sub> decomposes into BaO and CO<sub>2</sub> with the formation of monoferrite (BaFe<sub>2</sub>O<sub>4</sub>) and second, the diffusion of Ba<sup>2+</sup> into the iron oxide to form barium ferrite (BaFe<sub>12</sub>O<sub>19</sub>). The reaction involved in this transformation can be expressed as follows:



Figure 5.4 shows the X-ray diffraction (XRD) pattern of BaFe heat-treated at various temperatures. With increasing the heat-treatment temperature, BaFe particles attained a higher degree of crystallinity. However, secondary phases of hematite (α-Fe<sub>2</sub>O<sub>3</sub>) and the spinel BaFe<sub>2</sub>O<sub>4</sub> are observed as seen in in Figure. 5.4. TEM was used to observe the particle size and shape distribution of the synthesized S-BaFe nanoparticles by dispersing the particles in methanol. Figure 5.5 shows the TEM images of the S-BaFe nanoparticles that were heat-treated at 900 °C for 2 h. These particles exhibit spherical morphology and have a diameter of about 24 - 30 nm. To further confirm the crystal structure and the phase of S-BaFe nanoparticles, high-resolution TEM (HR-TEM) images were taken (University of Texas-Dallas) with electron diffraction patterns. From the diffraction patterns, the inter-planar lattice distance and angular relationship confirm that the synthesized spherical particles well match with the simulated diffraction pattern of hexagonal BaFe<sub>12</sub>O<sub>19</sub> as shown in Figure 5.6.

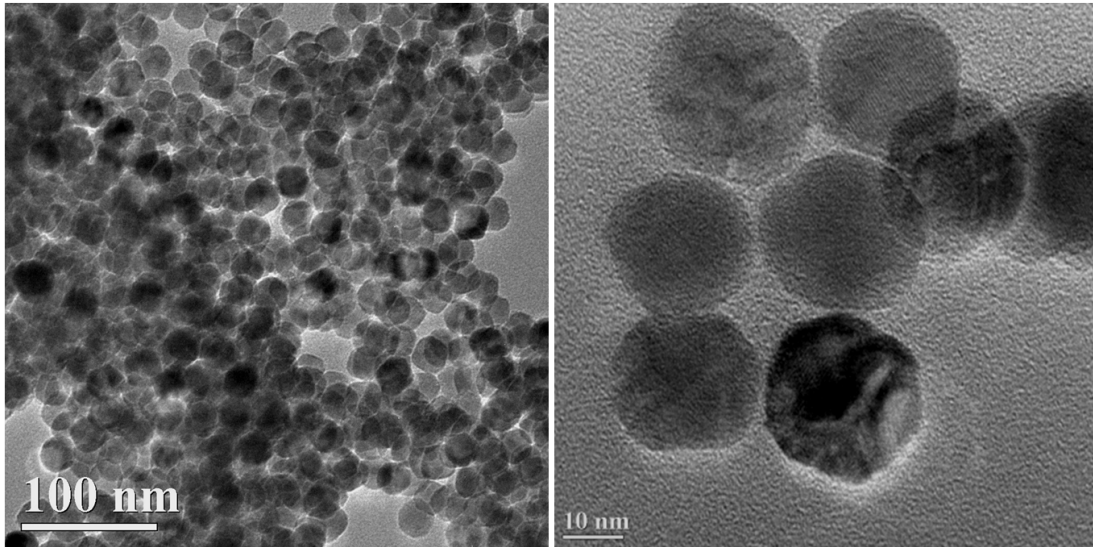


Figure 5.5 TEM micrographs of S-BaFe nanoparticles heat-treated at 900 °C for 2 h.

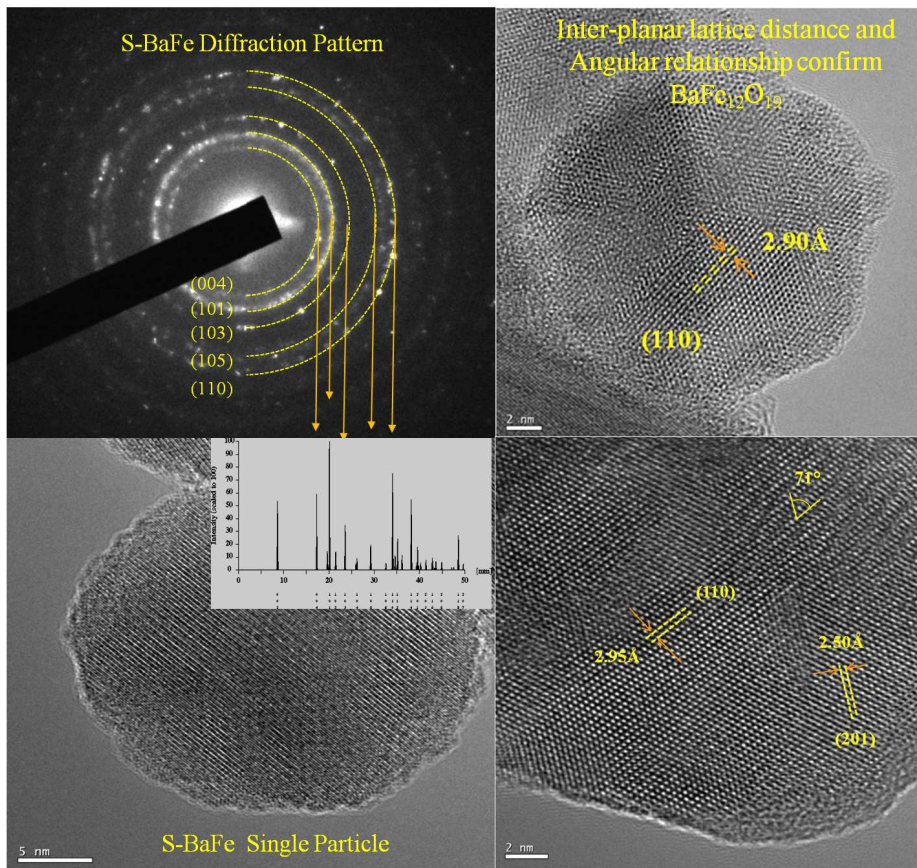


Figure 5.6 HR-TEM electron diffraction patterns of S-BaFe nanoparticles.

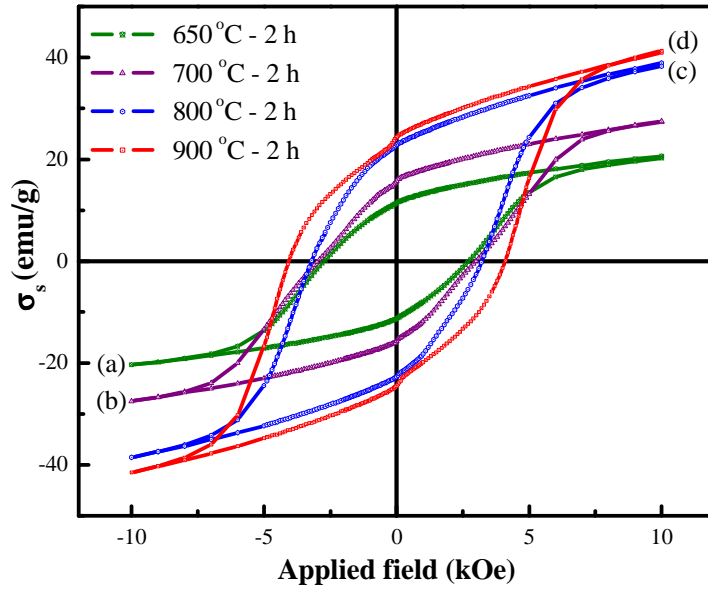


Figure 5.7 Magnetic hysteresis loops of S-BaFe nanoparticles as a function of various heat-treated temperatures.

Figure 5.7 shows the magnetic hysteresis loops of S–BaFe nanoparticles as a function of various heat-treatment temperatures. The higher the heat-treatment temperature, the greater the magnetization of the S-BaFe particles. This is attributed due to the improved crystallinity of barium ferrite phase with respect to the temperature. The particles that are heat-treated at 900 °C has 41.4 emu/g of saturation magnetization ( $\sigma_s$ ) and 4075 of coercivity ( $H_c$ ). The heat-treatment temperature dependence of magnetic properties are summarized in Table 5.1.

Temperature	650 °C	700 °C	800 °C	900 °C
Magnetic property	2 h	2 h	2 h	2 h
$\sigma_s$ (at $H_{app} = 10$ kOe) (emu/g)	20.6	27.3	38.9	41.4
$\sigma_r$ (emu/g)	11.4	15.7	22.5	24.3
$H_c$ (Oe)	2076	3089	3241	4075

Table 5.1 Magnetic properties of barium ferrite nanoparticles at various heat treatment temperatures.

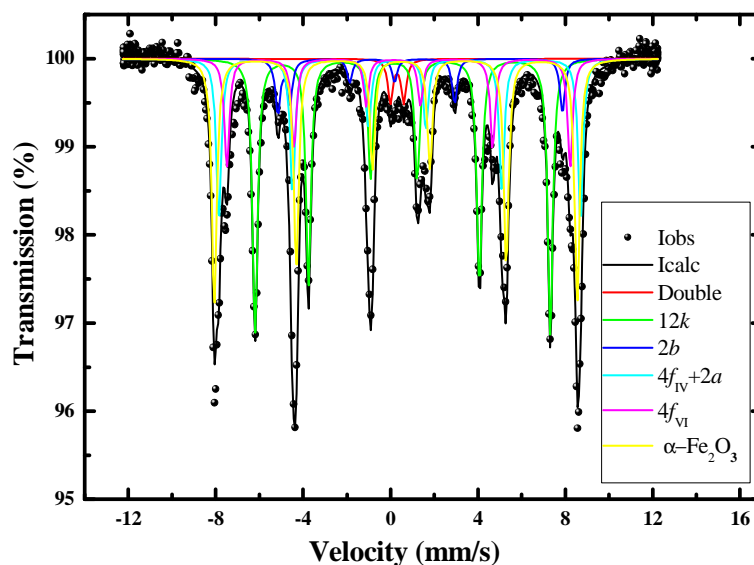


Figure 5.8 Mössbauer spectra of S-BaFe nanoparticles heat-treated at 900 °C for 2 h.

Room temperature Mössbauer spectra were taken for the S-BaFe nanoparticles which were heat-treated at 900°C for 2h. Mössbauer spectra were contributed by the magnetic hyperfine field from  $\text{Fe}^{3+}$  in five distinct crystallographic sites in the hexa-ferrite structure as shown in Figure. 5.8. Four of these sites, which are  $12k$ ,  $4f_{IV}$ ,  $2a$ , and  $2b$ , may be identified, but the weak  $2a$  spectrum is buried under the  $4f_{VI}$  spectrum. Also, in the spectrum some amount of hematite phase is also present. The results of Mössbauer characterization are in good agreement with the XRD patterns presented in Figure. 5.4 to confirm the  $\text{BaFe}_{12}\text{O}_{19}$  phase and also the S-BaFe nanoparticles are not superparamagnetic, but ferrimagnetic.

To study the magnetic interaction of the S-BaFe nanoparticles, 80 nm H-BaFe [60-63] particles and 24 nm S-BaFe nanoparticles [65] were embedded in non-magnetic paraffin wax and heated to melt the wax at 60 °C while applying a field of 10 kOe. The embedded samples were characterized by using VSM to plot the  $\Delta M$  curve. Figure 5.9 shows the  $\Delta M$  plot for the S-BaFe and H-BaFe nanoparticles with the respective TEM micrographs of the particles shown in the

insets. It is clearly seen from the plot that the platelet H-BaFe shows a strong large positive peak, which is attributed to the strong magnetic interaction fields occurring in poker-chip–like stacks of the platelet-shaped particles [60-63]. On the other hand, S-BaFe powder shows a strong negative peak. This means that there is a weak particle-to-particle interaction. However, the broad switching field distribution observed in the plot is attributed to the presence of residual hematite ( $\alpha\text{-Fe}_2\text{O}_3$ ) and  $\text{BaFe}_2\text{O}_4$  phases and also non uniform orientation, and/or poor crystallinity in of the S-BaFe powder.

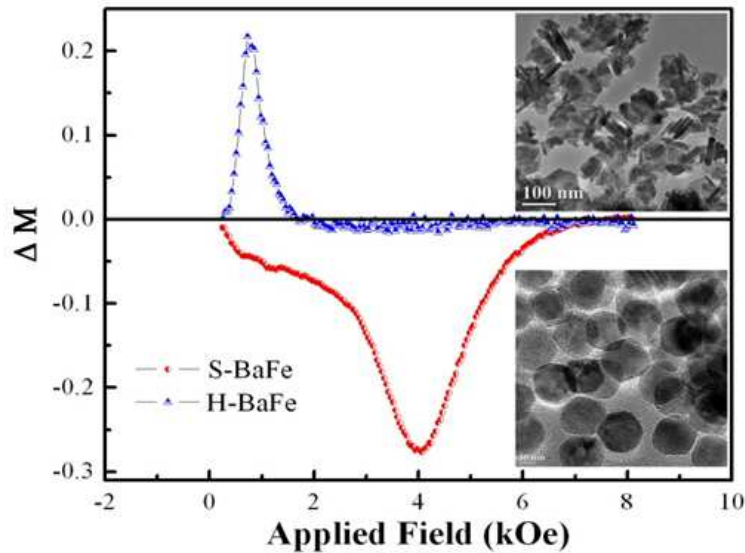


Figure 5.9  $\Delta M$  curve of spherical barium ferrite (S-BaFe) and hexagonal barium ferrite (H-BaFe) nanoparticles.

Thermal stability factor ( $K_u V/k_B T$ ) for the S-BaFe nanoparticles was determined by measuring the dynamic remanent coercivity measurements. The DCD remanence curves at different time scales of an applied field were obtained from VSM. Due to the thermal relaxation of the system, with an increase in the duration of the applied field, the remanent coercivity ( $H_{cr}$ ) decreases. The thermal stability factor,  $K_u V/k_B T$ , can be obtained from Sharrock's formula for 3D randomly oriented particles as [110]:

$$H_{cr}(t) = H_a \left[ 1 - \left[ \frac{k_B T}{K_u V} \ln \left( \frac{At}{\ln 2} \right) \right]^n \right] \quad (5.5)$$

where  $H_a$  is the intrinsic coercive field for a random distribution of non-interacting particles with uniaxial anisotropy constant  $K_u$  and  $V$  is the particle volume. The exponent  $n$  depends on the model of the energy barrier. In the present case,  $n = 2/3$  is used to account for the 3D random orientation of the particles. The attempt frequency  $A$  is taken to be  $10^9 \text{ s}^{-1}$ .  $k_B$  is the Boltzmann constant and  $T$  is the absolute temperature.  $t$  is the time needed for a constant field equaling to  $H_{cr}$  to reduce the magnetization from remanent saturation to zero. The values of  $H_a$  and  $K_u V/k_B T$  are obtained by fitting the  $H_{cr}$  and  $t$  values to the equation above as shown in Figure 5.10. From this analysis, a stability factor of  $K_u V/k_B T \approx 107$  is estimated for these S-BaFe nanoparticles.

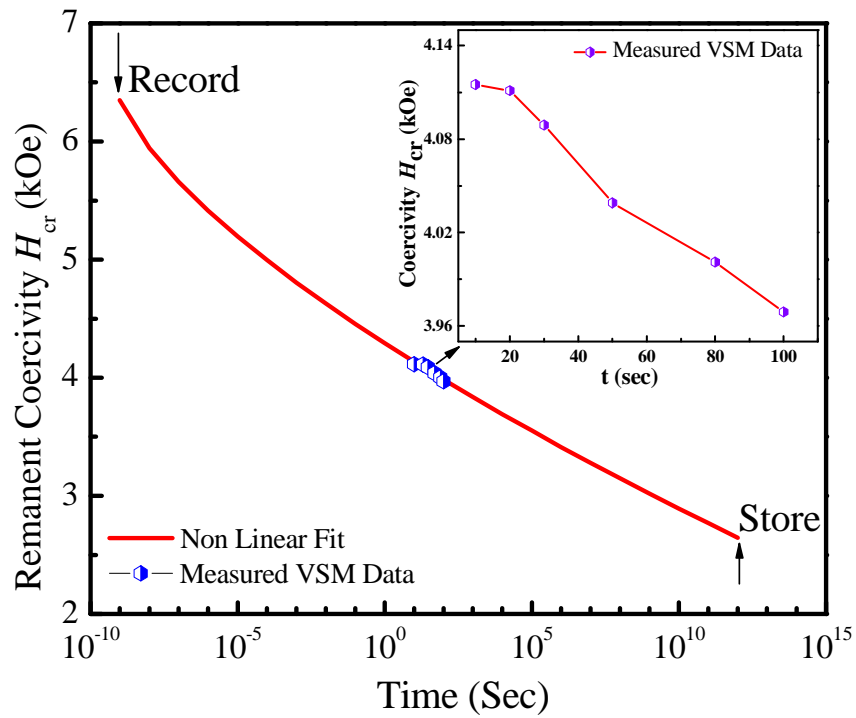


Figure 5.10 Remanent coercivity as a function of time measured by VSM and fitted curve using Sharrock's equation [110].

### 5.3.2. S-BaFe synthesized from hematite nanocubes

The cubic hematite nanoparticles were also coated with the BaCO<sub>3</sub> employing the same process as described in the previous section for the conversion of S-Mag particles to S-BaFe particles. Figure 5.11 shows the magnetite hysteresis loop of the precursory hematite nanocubes used for the conversion process before and after the BaCO<sub>3</sub> coating process. The inset in the Figure 5.11 also shows the TEM micrograph of the precursory hematite nanocubes used for the process. It is interesting to observe that there is a change in the magnetic properties before and after the coating process. The saturation magnetization ( $\sigma_s$ ) decreased from 0.92 emu/g to 0.45 emu/g and the coercivity increased from 99.04 Oe to 196.61 Oe, respectively. This change in the magnetic properties can be attributed to the BaCO<sub>3</sub> absorption on the hematite nanocubes decreasing the net magnetization of the hematite particles.

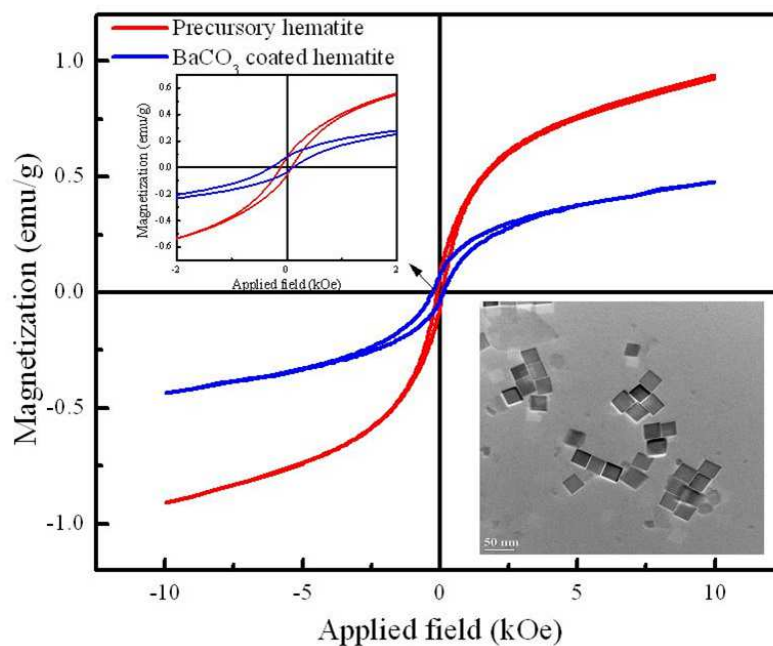


Figure 5.11 Magnetic hysteresis loops of the precursory hematite nanocubes before and after BaCO<sub>3</sub> coating.

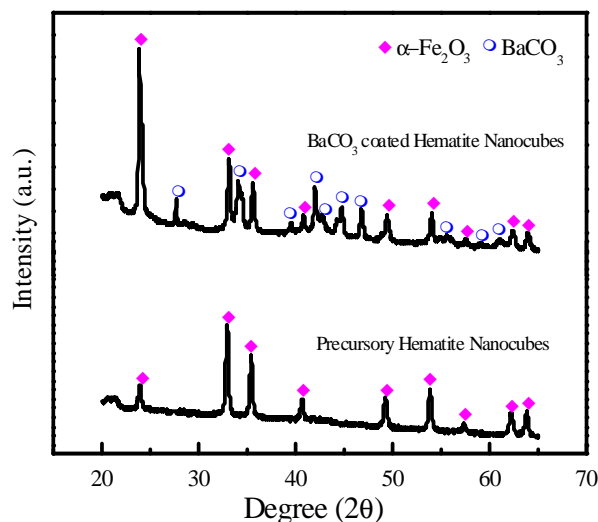


Figure 5.12 XRD patterns of the precursory hematite nanocubes before and after BaCO<sub>3</sub> coating.

Figure 5.12 shows the XRD patterns of the hematite nanocubes before and after BaCO<sub>3</sub> coating process. From the XRD patterns, it is clear that the extra peaks correspond to the BaCO<sub>3</sub> phase which is in good agreement with the magnetic hysteresis loops shown in Figure 5.11. To further understand the phase transformation and kinetics involved we performed thermogravimetry (TG) analysis on the as-coated hematite nanocubes in the temperature range from 20 °C to 700 °C. Figure 5.13 shows the change in weight percentage as a function of temperature for the as-coated hematite nanocubes and it can be observed that at 50 °C there is a sudden drop in the weight percent due to the evaporation of the residual moisture and/or ethanol on the colloidal particles. The second major weight loss occurs from 270 °C to 450 °C, which can be attributed to the evaporation of the residual nitrate and organic matter in the precursory coated hematite nanocubes. The further reduction at 600 °C indicates a complete thermal decomposition of the precursory particles and the nucleation of the crystalline of BaFe<sub>12</sub>O<sub>19</sub>. However, due to the limitations of the temperature range on the TGA instrument, higher temperature (> 700°C) could not be performed for the as-coated hematite nanocubes.

With regard to the conversion of cubic hematite nanoparticles to S-BaFe, the as-coated precursory particles were heat-treated at various temperatures between 650-900°C under oxygen atmosphere.

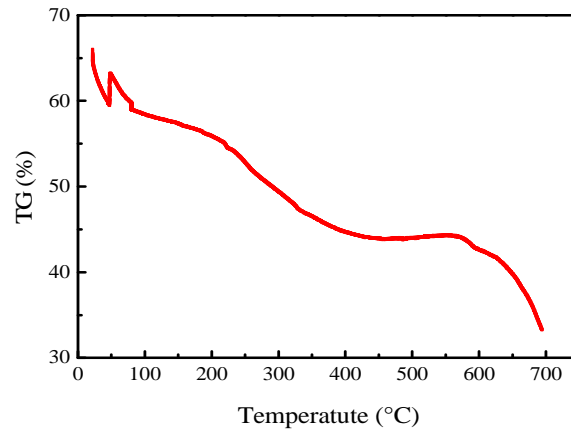


Figure 5.13 Thermogravimetry analysis curve showing the percentage weight as a function of temperature for the as-coated hematite nanocubes.

Figure 5.14 shows the X-ray diffraction patterns of precursory barium ferrite powder annealed in the oxygen atmosphere at various temperatures. It is evident from the XRD pattern that the crystallization of  $\text{BaFe}_{12}\text{O}_{19}$  is enhanced as the annealing temperature is raised above 800 °C. However, a small amount of intermediate phases such as  $\alpha\text{-Fe}_2\text{O}_3$  and  $\text{BaFe}_2\text{O}_4$  still exist in the final powders. As described earlier in the previous chapter during the annealing process, barium ions ( $\text{Ba}^{2+}$ ) in colloidal form diffuse into the cubic hematite nanoparticles, and the hematite particles are converted to the S-BaFe nanoparticles. The formation mechanism of barium ferrite by the solid state reaction takes place in two different steps. First, the decomposition together with the formation of monoferrite, and second the diffusion of  $\text{Ba}^{2+}$  into the iron oxide to form barium ferrite [109]. The reaction involved in the transformation is given below:



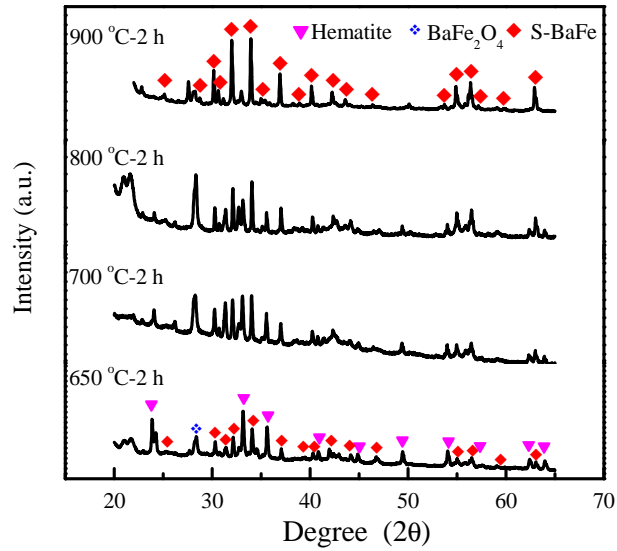


Figure 5.14 XRD patterns of S-BaFe as a function of various heat-treated temperatures; (a) 650 °C for 2 h, (b) 700 °C for 2 h, (c) 800 °C for 2 h, and (d) 900 °C for 2 h.

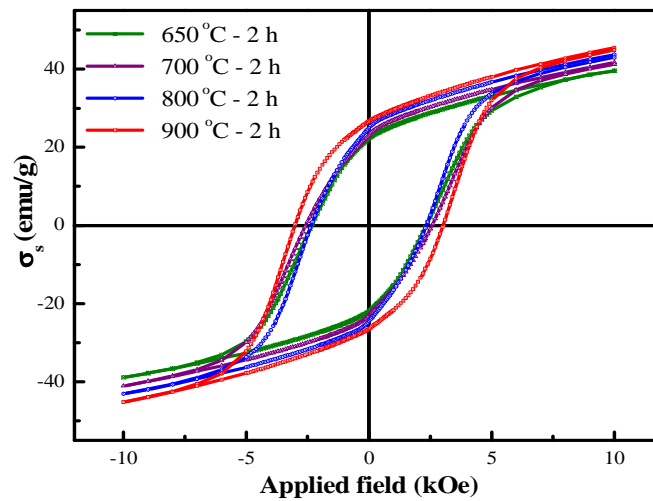


Figure 5.15 Magnetic properties of S-BaFe nanoparticles as a function of various heat-treated temperatures.

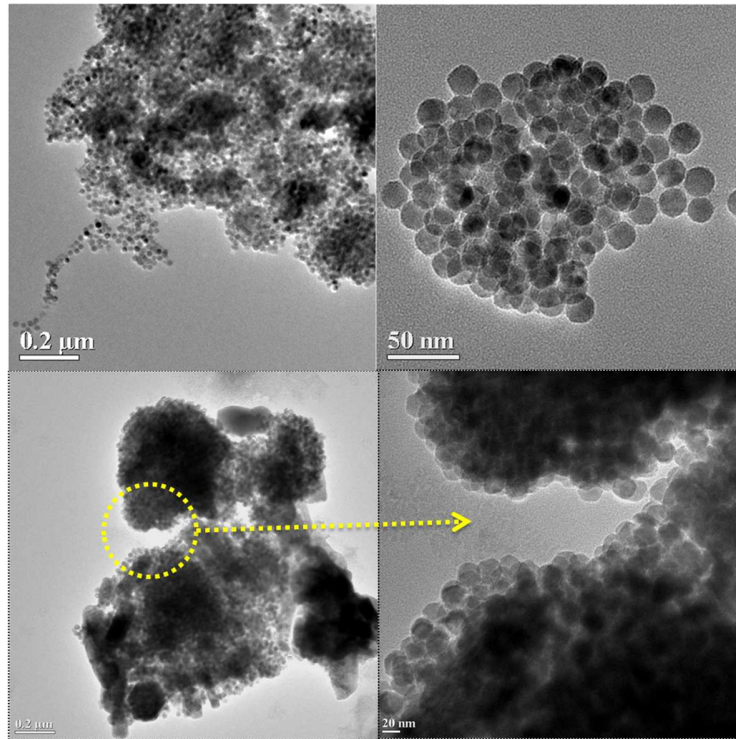


Figure 5.16 TEM micrographs of S-BaFe nanoparticles heat-treated at 900 °C for 2 h.

Figure 5.15 shows the magnetic properties of the spherical barium ferrite nanoparticles as a function of various heat-treated temperatures. The particles heat-treated for a 2 h period at 900 °C show the maximum saturation magnetization ( $\sigma_s$ ) of 45.4 emu/g with an intrinsic coercivity ( $H_c$ ) of 3015 Oe at a maximum applied field of 10 kOe. It is evident from the plot that the saturation magnetization enhancement is directly related to the higher amount of  $\text{BaFe}_{12}\text{O}_{19}$  formed as the temperature was raised, which was confirmed by the XRD pattern. The magnetic properties of the samples heat-treated at 650 °C, 700 °C, and 800 °C are 39.6 emu/g, 41.7 emu/g, and 43.7 emu/g, respectively and the coercivities ranged from 2300 Oe to 2400 Oe. The morphology of the synthesized S-BaFe particles was observed by TEM. Figure 5.16 shows the TEM micrographs of the S-BaFe nanoparticles heat-treated at 900 °C for 2 h. The shapes of the particles are spherical, and the size ranged from 20-22 nm, respectively. The conversion of cubic

hematite to S-BaFe is still under investigation . However, we assume that during the heat-treatment process surface diffusion of Ba ions occurs at elevated temperatures causing atomic re-arrangement in the particles, and the surface of the cubic structure undergoes deformation by the process, of surface melting and an inter-particle coalescing. This might follow up forming islands of small crystal nuclei of barium ferrite in the matrix. And as the temperature is increased, the crystal grows transforming into a spherical shape which has the lowest surface tension and a stable shape as shown in the TEM images of Figure 5.16. This type of transformation was earlier reported for Pt crystals from cubic/tetrahedral to spherical morphology [117].

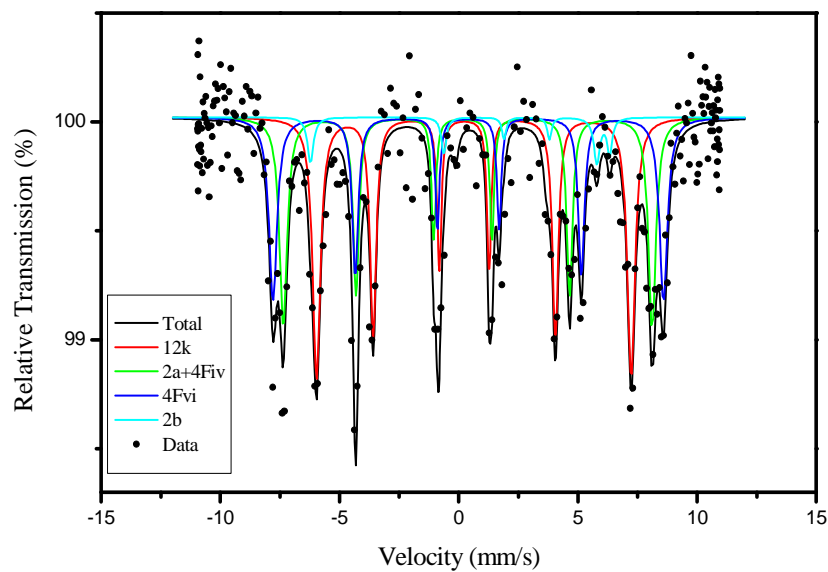


Figure 5.17 Mössbauer spectra of S-BaFe nanoparticles heat-treated at 900 °C for 2 h.

Room temperature Mössbauer spectra were performed on the particles heat-treated at 900 °C for 2 h as shown in the Figure. 5.17. Mössbauer spectra were contributed by the magnetic hyperfine field from  $\text{Fe}^{3+}$  in five distinct crystallographic sites in the barium ferrite structure. All the five sites, which are 12k, 2a, 2b, 4f<sub>IV</sub> and 4f<sub>VI</sub> are identified. Mössbauer spectrum clearly demonstrates that the synthesized S-BaFe particles show no superparamagnetic phase.

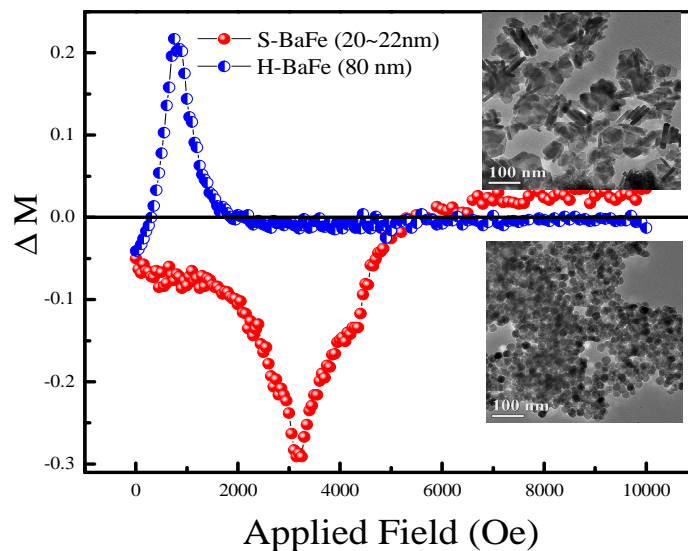


Figure 5.18  $\Delta M$  curve of spherical barium ferrite (S-BaFe) and hexagonal barium ferrite (H-BaFe) nanoparticles.

To study the dispersibility and the magnetic interaction of the spherical barium ferrite particles the barium ferrite powders are mixed in nonmagnetic paraffin. The mixture of the paraffin and the particles are subjected to a melting temperature around 60 °C while orienting in the presence of a strong magnetic field of 10 kOe. The samples were subsequently cooled down below the melting temperature of paraffin in this field to have magnetic orientation. The oriented particles were characterized by using VSM to plot the  $\Delta M$  curve to understand the particle interactions. We compared our results to hexagonal barium ferrite platelet shaped (H-BaFe) particles, previously developed by the authors [60-63] which are ~ 80 nm in size. Figure 5.18 shows the  $\Delta M$  plot for the S-BaFe and H-BaFe particles with the respective TEM micrographs shown in the inset. It is clearly seen from the plot that the platelet H-BaFe shows a strong large positive peak, which is attributed to the strong positive magnetic interaction fields occurring in poker-chip-like stacks of the platelet-shaped particles [60-63]. On the other hand, S-BaFe

particles show a different behavior which is a strong negative peak which confirms that there is only a point- to- point contact between the particles and are well-dispersed in the paraffin matrix without any stacks formation unlike the H-BaFe particles. However, we observe a broad switching field distribution due to the presence of residual hematite and other monoferrite phase in the final barium ferrite powders.

## 6.0. S-BaFe synthesis from worm-shaped hematite nanoparticles

### 6.1. Introduction

The adsorption-diffusion process described in the previous sections although obtained S-BaFe nanoparticles it involves several processing steps as well as higher heat treatment temperatures, which causes the S-BaFe particles to agglomerate and sometimes nonuniform size distribution due to non-dispersed precursory particles during the coating process. In this section, an alternative hydrothermal process was developed and optimized to synthesize pseudo S-BaFe nanoparticles. In this process, we first produce intermediate worm-shaped antiferromagnetic hematite particles (60 nm in length and 20 nm in width) containing a small amount of spinel barium iron oxide that are in turn converted to ultrafine, ferrimagnetic S-BaFe nanoparticles (25-45 nm in diameter) [66]. We also report the magnetic properties and thermal stability of resulting S-BaFe nanoparticles that are suitable for future high-density magnetic recording media applications.

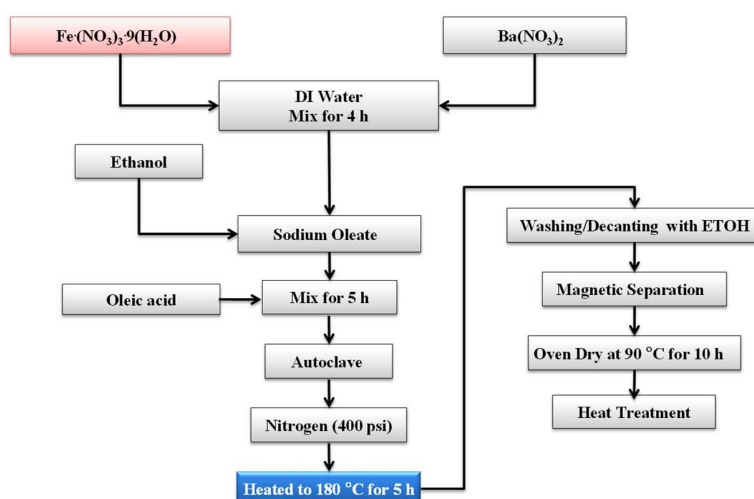


Figure 6.1 Flowchart showing the process to synthesize S-BaFe nanoparticles.

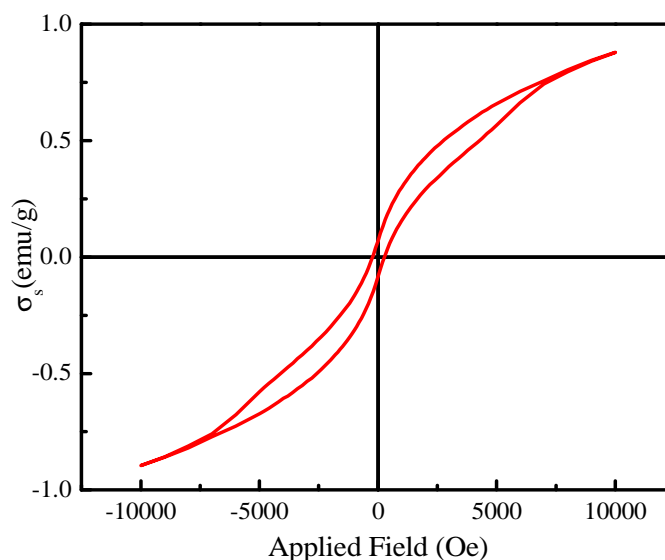


Figure 6.2 Magnetic properties of as-collected oven dried precursor nanoparticles.

## 6.2. Experimental

A hydrothermal process was employed to synthesize the worm-shaped antiferromagnetic hematite particles as shown in the flowchart of Fig 6.1. In a typical process a mixture comprising of  $\text{Ba}(\text{NO}_3)_2$  and  $\text{Fe}(\text{NO}_3)_3 \cdot 9(\text{H}_2\text{O})$  dissolved in 60 mL distilled water, 60 mL ethanol and 10 mL oleic acid with sodium oleate, was autoclaved at  $180^\circ\text{C}$  for 5-12 h and cooled to the room temperature. After the autoclaving step is completed, the brownish red precipitates at the bottom of the Teflon liner of the autoclave were collected and washed with a combination of ethanol and hexane. The resulting precipitates were dried in an oven for 8-10 h at  $90^\circ\text{C}$ . The dried fine particles comprising hematite ( $\alpha\text{-Fe}_2\text{O}_3$ ) coated with barium iron oxide ( $\text{BaFe}_2\text{O}_4$ ) were subjected to heat-treatment at various temperatures to be converted to ultrafine S-BaFe particles. The collected precursory and S-BaFe particles were characterized by X-ray powder diffraction (XRD) to identify crystalline phases. Transmission electron microscopy (TEM) analyses were performed to assess the particles morphology and crystallinity. The specific saturation magnetization, coercivity, and dynamic remanent coercivity of the S-BaFe

nanoparticles were measured at room temperature by vibrating sample magnetometry (VSM) at a maximum applied field of 10 kOe.

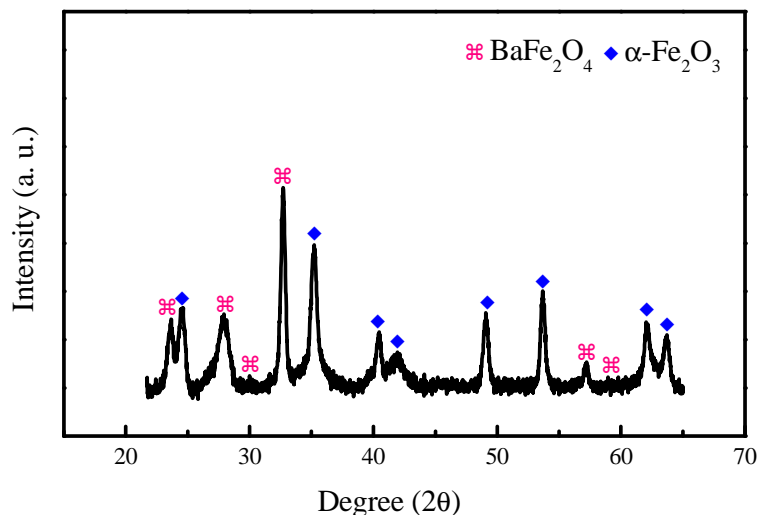


Figure 6.3 XRD patterns of the as-collected oven dried nanoparticles.

### 6.3. Results and discussion

Figure 6.2 shows the hysteresis loop of the oven-dried as-collected precursor particles obtained from the autoclave, which show typical hematite-like magnetic properties. The saturation magnetization of the as-collected particles is 0.78 emu/g at 10 kOe, and the coercivity is 250 Oe. Figure 6.3 shows the XRD pattern of the as-collected precursor particles. The pattern confirms that the precursor particles are composed of hematite ( $\alpha$ -Fe<sub>2</sub>O<sub>3</sub>) and spinel monoferrite (BaFe<sub>2</sub>O<sub>4</sub>). It is understood that during the hydrothermal process, iron nitrate reacted with the barium nitrate to form hematite and monoferrite. The morphology of the as-collected precursor particles observed by TEM shows a worm-like particle shape with a length of 60 nm and width of 20 nm as shown in Figure 6.4. There was no significant change in the shape and size of the particles with longer reaction time. To convert the precursor worm-shaped particles ( $\alpha$ -Fe<sub>2</sub>O<sub>3</sub>/BaFe<sub>2</sub>O<sub>4</sub>) to spherical barium ferrite (S-BaFe) nanoparticles, the precursor particles were

heat-treated at various temperatures. During the process of heat treatment, BaFe<sub>2</sub>O<sub>4</sub> reacted with hematite (α-Fe<sub>2</sub>O<sub>3</sub>) to form barium ferrite (BaFe<sub>12</sub>O<sub>19</sub>) [109].

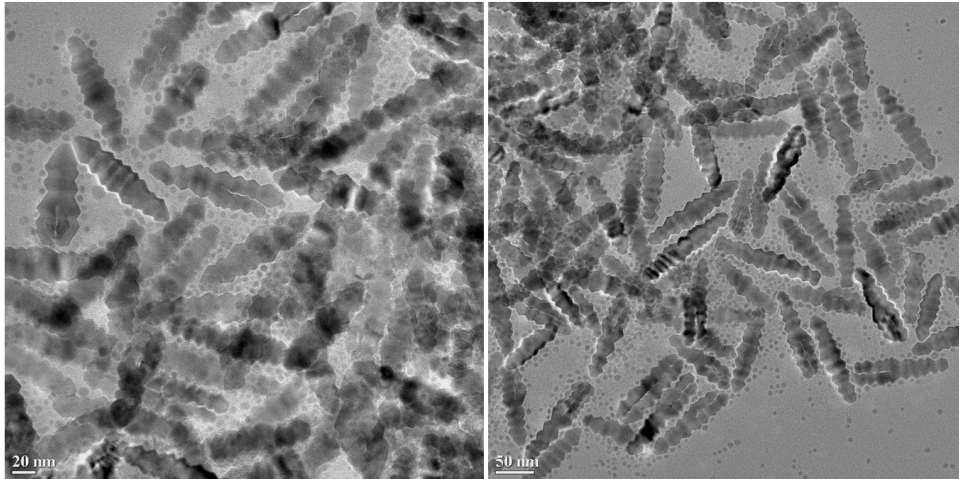
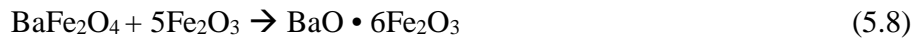


Figure 6.4 TEM micrographs of as-collected oven dried nanoparticles.

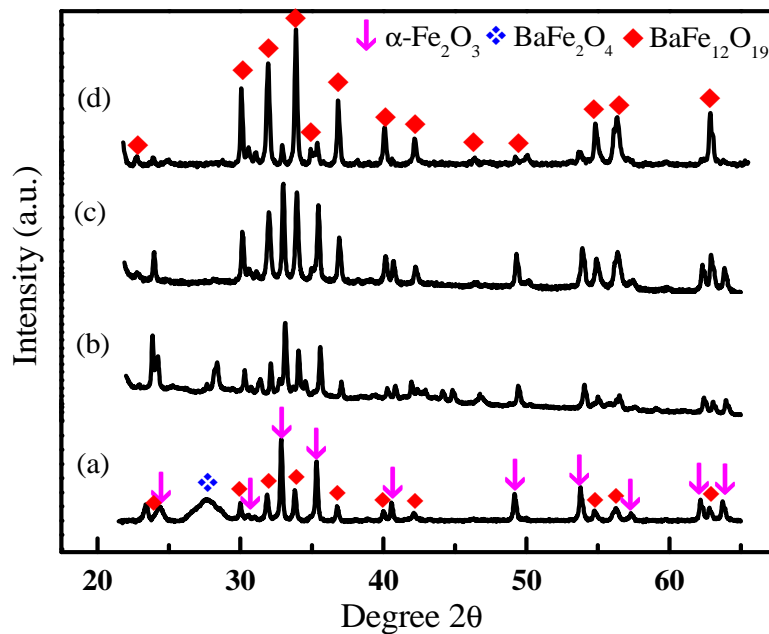


Figure 6.5 XRD patterns of S-BaFe as a function of various heat-treatment temperatures (a) 680°C, (b) 700°C, (c) 750°C, and (d) 800°C for 2 h.

Figure 6.5 shows the X-ray diffraction patterns of the heat-treated particles from 680 to 800°C for 2 h in air. The intensities of X-ray peaks, corresponding to the phases of  $\alpha$ -Fe<sub>2</sub>O<sub>3</sub> and BaFe<sub>2</sub>O<sub>4</sub>, weaken as the temperature increases from 680°C to 800°C. Barium ferrite phase with an insignificant amount of the hematite phase was observed from S-BaFe nanoparticles heat-treated at 800°C as shown in Figure 6.5 (d). The morphology of the synthesized BaFe particles was observed by a TEM. The BaFe particles exhibited spherical morphology, and the size ranged from 25 to 45 nm as shown in Figure 6.6. The magnetic hysteresis loop of S-BaFe nanoparticles annealed at 800°C for 2 h showed a saturation magnetization ( $\sigma_s$ ) of 50.7 emu/g and coercivity ( $H_c$ ) of 4311 Oe at a maximum applied field of 10 kOe. The hysteresis loop resembles the one proposed by Stoner Wohlfarth [111] for an assembly of non-interacting, single magnetic domain, and uniaxial particles having their axes randomly oriented as showing in Figure 6.7. Therefore, we can conclude that our S-BaFe nanoparticles are well-separated, hold their single-domain structure and are not interacting with each other. This confirms again the advantage of our previously proposed S-BaFe [60-66] over the hexagonal BaFe platelets, which have been used for extremely high-density recording tape.

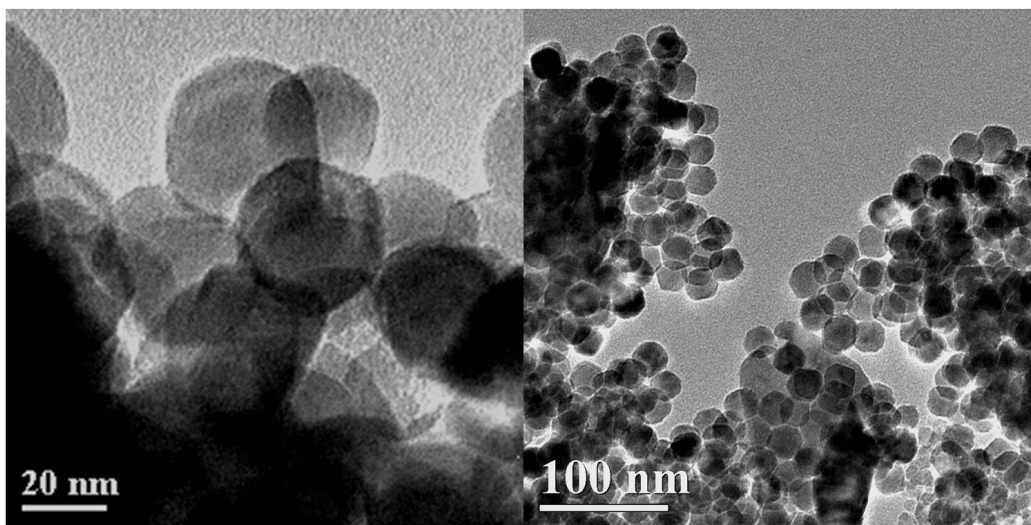


Figure 6.6 TEM micrographs of S-BaFe nanoparticles heat-treated at 800°C for 2 h.

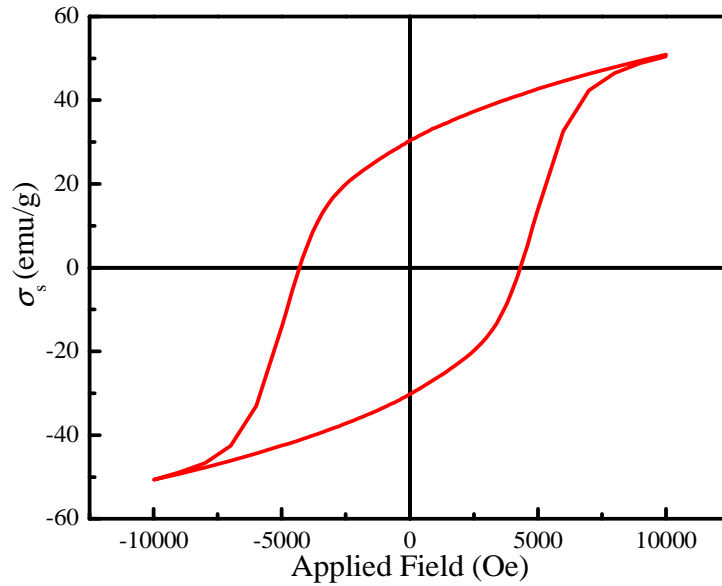


Figure 6.7 Magnetic hysteresis loop of S-BaFe heat-treated at 800°C for 2 h.

The shape-transformation mechanism, from the worm shape of antiferromagnetic particles to the spherical shape of ferrimagnetic barium ferrite nanoparticles, is not yet understood. The saturation magnetization of  $\sigma_s$  (50.7 emu/g) is much lower than the theoretical value of 72 emu/g [83] for bulk single crystal barium ferrite. This is attributed to the smaller size of the particles than the magnetic single domain size of 0.1  $\mu\text{m}$  and small degree of crystallinity due to the lower heat-treatment temperature. This low-heat treatment temperature led to the incomplete crystallization of barium ferrite, leaving behind existence of a small amount of the hematite phase in S-BaFe powder as confirmed by the XRD pattern in Figure 6.5. Moreover, it has been proposed that the relatively small magnetization in fine particles arises due to the surface effects such as spin canting and sample inhomogeneity [112]. The effect of annealing temperature on the magnetic properties of S-BaFe particles is presented in Figure 6.8. The saturation magnetization enhancement is directly related to the higher amount of  $\text{BaFe}_{12}\text{O}_{19}$  crystallinity as the temperature was increased, which is in good agreement with the XRD pattern.

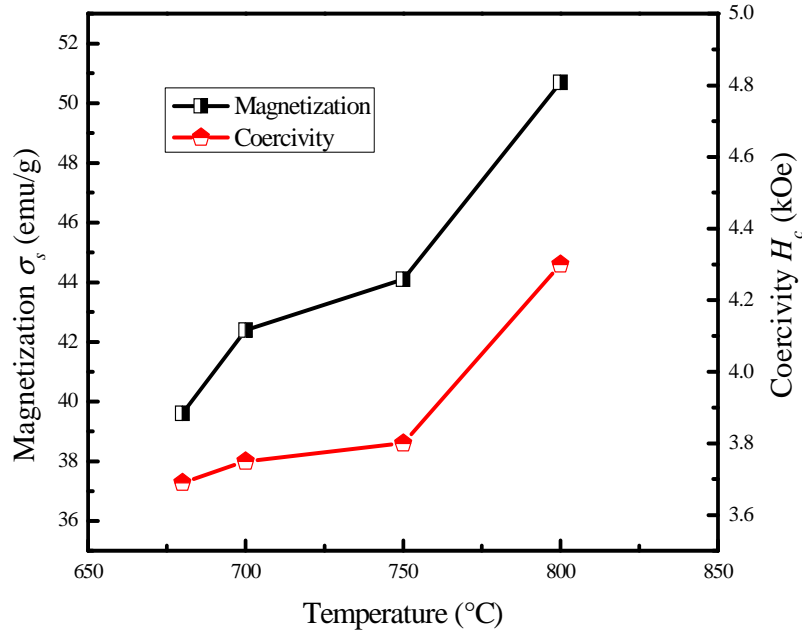


Figure 6.8 Magnetic properties as a function of heat-treatment temperatures of S-BaFe nanoparticles.

The magnetic properties of the samples heat-treated at 680°C, 700°C, 750°C, and 800°C are 39.6 emu/g, 42.4 emu/g, 44.1 emu/g, and 50.7 emu/g, respectively, and the coercivity ranges from 3600 Oe to 4300 Oe. In order to evaluate archival stability of information data storage media, the thermal stability factor  $K_u V / k_B T$  for the synthesized S-BaFe nanoparticles was determined by performing the dynamic remanent coercivity measurements with VSM. DC-demagnetization measurement (DCD) at different time scales for an applied field were performed on S-BaFe particles. Due to thermal relaxation of the particles, remanent coercivity ( $H_{cr}$ ) decreases with an increase in the duration time of the applied field. The thermal stability factor,  $K_u V / k_B T$ , can be obtained from Sharrock's formula for 3D randomly oriented particles as:

$$H_{cr}(t) = H_a \left[ 1 - \left[ \frac{k_B T}{K_u V} \ln \left( \frac{At}{\ln 2} \right) \right]^n \right] \quad (5.9)$$

where  $H_o$  is the intrinsic coercive field for a random distribution of non-interacting particles with uniaxial anisotropy constant  $K_u$  and  $V$  is the magnetic activation volume. The exponent  $n$  depends on the model of the energy barrier. In the present case,  $n = 2/3$  is used to account for the 3D random orientation of the particles. The attempt frequency  $A$  is taken to be  $10^9\text{s}^{-1}$ .  $k_B$  is the Boltzmann constant and  $T$  is the absolute temperature.  $t$  is the time needed for a constant field equaling to  $H_{cr}$  to reduce the magnetization from remanent saturation to zero. The values of  $H_a$  and  $K_uV/k_B T$  are obtained by fitting the  $H_{cr}$  and  $t$  values to the equation above as shown in Figure 6.9. From this analysis, a stability factor of  $K_uV/k_B T \approx 81$  is estimated for the S-BaFe nanoparticles which is high enough to maintain archival property of data storage media.

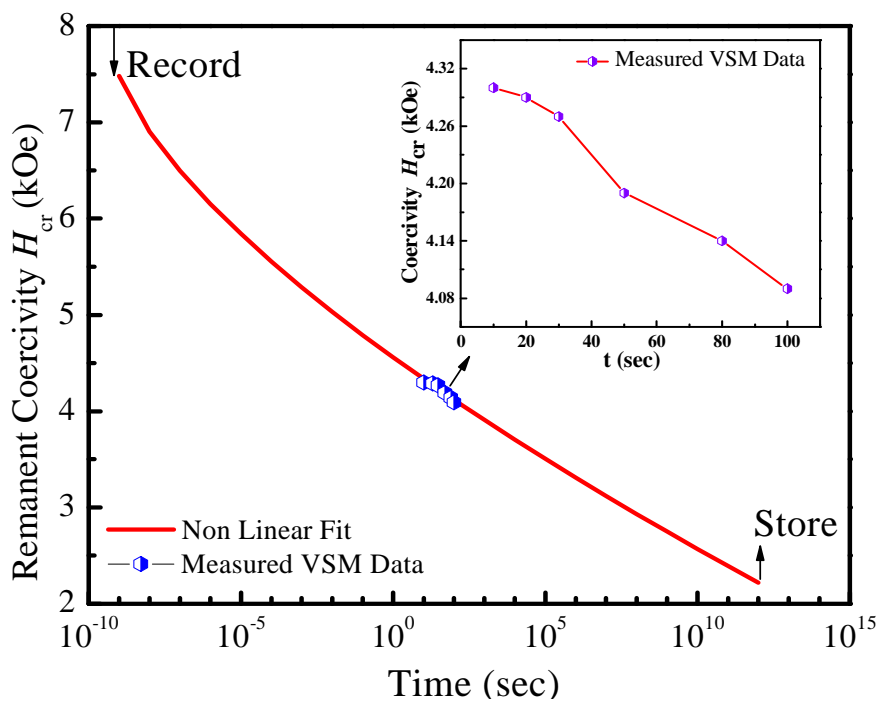


Figure 6.9 Remanent coercivity as a function of time measured by VSM and fitted curve using Sharrock's equation [110].

Also, to study the particle shape effect on the activation volume of the synthesized S-BaFe particles we calculated and compared the activation volumes of S-BaFe with that of the H-BaFe particles. By using the thermal stability factor of 81 an activation volume ( $V$ ) of  $1961 \text{ nm}^3$  is obtained using  $K_u = H_k M_s / 2x$  [13] where  $H_k = 7500 \text{ Oe}$  and  $M_s = 228 \text{ emu/cc}$  (density of barium ferrite =  $4.5 \text{ g/cc}$ ) at room temperature and  $x = 0.5$  [110]. On the other hand, for  $21 \text{ nm}$  (physical volume =  $2200 \text{ nm}^3$ ) H-BaFe particles a  $V$  of  $4559 \text{ nm}^3$  is expected from  $K_u = 7.9 \times 10^5 \text{ erg/cc}$  and  $K_u V / k_B T = 87$  at room temperature [31]. The difference in volume for the S-BaFe particles can be understood by two reasons. First, our preliminary results show that the S-BaFe particle may actually be an H-BaFe particle surrounded by a non-magnetic  $\text{Fe}_x\text{O}_y$  shell [113-114] which causes the magnetic volume much smaller than geometric volume. Secondly, it has been previously reported that an increase in activation volume is expected if the mutual particle-to-particle interaction is greater in the medium [115]. In our case, due to the spherical nature of the particles mutual particle-to-particle interaction is much weaker; therefore a lower  $V$  is expected. This was previously confirmed in our work, which showed a weak particle-to-particle interaction when compared to H-BaFe nanoparticles [60-63]. Understanding the mechanisms for the phase and crystallographic transformation from  $\alpha\text{-Fe}_2\text{O}_3$  to S-BaFe will give us more information to evaluate these particles, which is currently under investigation.

## PART II. HEXAFERRITE SINGLE CRYSTALS

### I. Introduction

There has been an increasing demand for ferrite materials in high-frequency applications such as telecommunications and radar systems as microwave technology requires higher frequencies and bandwidths up to 100 GHz [1-6]. Ferrites are nonconducting oxides and therefore allow total penetration of electromagnetic fields, in contrast with metals, where the skin effect severely limits the penetration of high-frequency fields [7-8]. At such high frequencies, domain walls are unable to follow the fields (dispersion of domain walls typically occurs about 10 GHz), and absorption of microwave power takes place by spin dynamics. The usual geometry is to align spins first with a DC magnetic field  $H$  and apply the microwave field perpendicular to  $H$ . The spins precess around their equilibrium orientation at the frequency of the microwave field. Since their invention, hexagonal ferrites have received considerable attention for the next generation of millimeter wave ferrite devices [3-5]. For example, M-type barium hexaferrite ( $\text{BaFe}_{12}\text{O}_{19}$ , BaM) has a high saturation magnetization ( $4\pi M_s$ ) and large uniaxial magnetocrystalline anisotropy ( $H_A$ ) which allows microwave devices such as circulators and isolators operate in the range above 40 GHz without an external bias magnetic field [4-5]. Besides the M-type, there are several other hexagonal ferrite groups such as Y, W, X, U and Z-Type [7-9]. These ferrites have complicated crystal structures but are very much interrelated in terms of their individual stacking of the spinel (S) and hexagonal (R) blocks to form the crystal structures. The composition and formation of these ferrites can be understood from the ternary

phase diagram of BaO, FeO, and MeO system, where Me is one of the divalent metals which form spinel structure with iron oxide as shown in Figure 1.1. For example, the W-type hexaferrites with the chemical formula of  $\text{BaMe}_2\text{Fe}_{16}\text{O}_{27}$  can be represented as  $W = M + S$ , where,  $M = \text{BaFe}_{12}\text{O}_{19}$  or  $\text{BaO} \cdot 6\text{Fe}_2\text{O}_3$ , and  $S$  (spinel) =  $2 \text{Me}^{2+}\text{Fe}_2\text{O}_4$  or  $2\text{MeO} \cdot 2\text{Fe}_2\text{O}_3$ , (where  $\text{Me} = \text{Fe}, \text{Co}, \text{Mn}, \text{Ni}, \text{Cu}, \text{Mg}, \text{Zn}$  representing the metal cations) respectively. Similarly, The Y-type hexaferrite with the composition,  $\text{Ba}_2\text{Me}_2\text{Fe}_{12}\text{O}_{22}$ , also called as planar hexaferrite comprises a combination of the stacks S and T blocks, where  $T = \text{Ba}_2\text{Fe}_8\text{O}_{14}$ . Another planar hexaferrite is the Z-type hexaferrite with the composition  $3\text{BaO} \cdot 2\text{MeO} \cdot 12\text{Fe}_2\text{O}_3$ , can be constructed by  $Z = M + Y$ . Table 1.1 shows the different hexaferrite compositions and their crystal structure and stacking orders respectively.

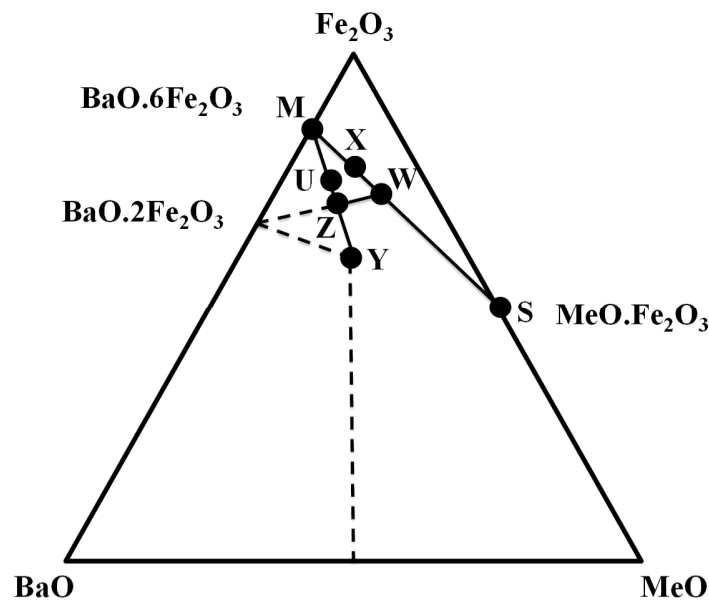


Figure 1.1 Chemical composition diagram showing how the hexagonal ferrites are derived from the spinel  $\text{MeO} \cdot \text{Fe}_2\text{O}_3$  structure [9].

Hexaferrite Type	Composition (Chemical Formula)	Stacking Order	Interrelation
M	$\text{Ba}^{2+}\text{Fe}_{12}\text{O}_{19}$ or $\text{BaO}\cdot 6\text{Fe}_2\text{O}_3$	RSR*S*	M
W	$\text{Ba}_2^{2+}\text{Me}_2^{2+}\text{Fe}_{16}\text{O}_{27}$ or $\text{BaO}\cdot 2\text{MeO}\cdot 8\text{Fe}_2\text{O}_3$	RSSR*S*S*	M+S
Y	$\text{Ba}_2^{2+}\text{Me}_2^{2+}\text{Fe}_{12}\text{O}_{22}$ or $2\text{BaO}\cdot 2\text{MeO}\cdot 6\text{Fe}_2\text{O}_3$	TSTSTS	Y
Z	$\text{Ba}_3^{2+}\text{Me}_2^{2+}\text{Fe}_{24}\text{O}_{41}$ or $3\text{BaO}\cdot 2\text{MeO}\cdot 12\text{Fe}_2\text{O}_3$	RSTSR*S*T*S*	M+Y
U	$\text{Ba}_4^{2+}\text{Me}_2^{2+}\text{Fe}_{36}\text{O}_{60}$ or $4\text{BaO}\cdot 2\text{MeO}\cdot 18\text{Fe}_2\text{O}_3$	RSR*S*T*S*	2M+Y
X	$\text{Ba}_2^{2+}\text{Me}_2^{2+}\text{Fe}_{28}\text{O}_{46}$ or $2\text{BaO}\cdot 2\text{MeO}\cdot 14\text{Fe}_2\text{O}_3$	RSR*S*S*	2M+S

Table 1.1 Chemical composition and interrelation of hexagonal ferrites, where S =  $\text{Fe}_6\text{O}_8$  (spinel), R =  $\text{BaFe}_6\text{O}_{11}$  (hexagonal), and T =  $\text{Ba}_2\text{Fe}_8\text{O}_{14}$  (hexagonal). The asterisk (\*) indicates that the corresponding sub-unit is rotated  $180^\circ$  around the hexagonal  $c$ -axis [9].

In the next few sections of this chapter, the magnetic crystal structures of the M and Y-type hexaferrites will be discussed followed by some background information on the important magnetic, microwave and applications of these hexaferrites.

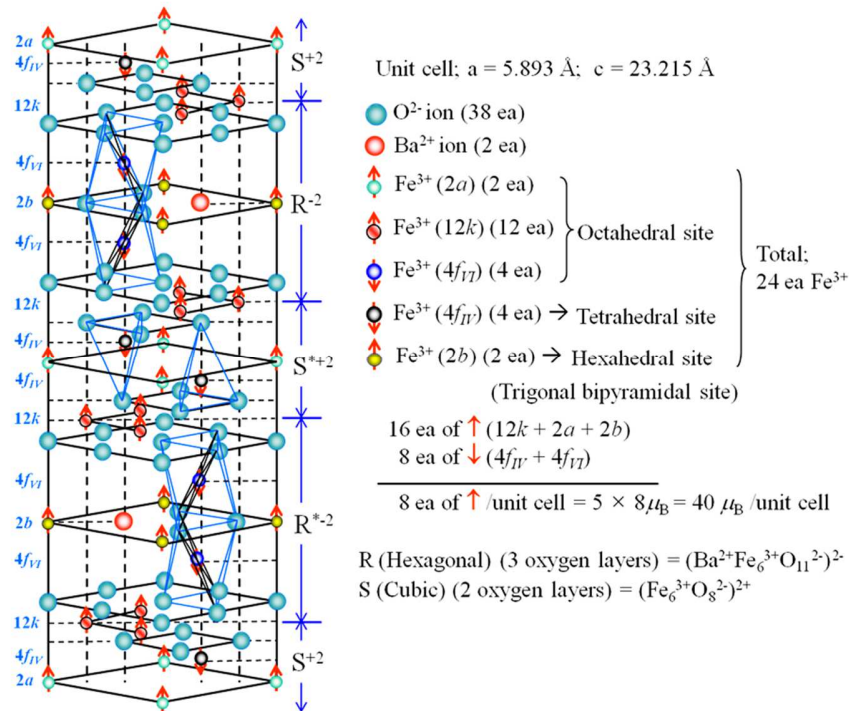


Figure 1.2 Magnetic structure of barium ferrite BaM ( $\text{BaFe}_{12}\text{O}_{19}$ , BaFe) [10].

### 1.1. M-type barium ferrite (BaM)

Barium ferrite (BaM) has the same crystal structure as magnetoplumbite ( $\text{PbFe}_{7.5}\text{Mn}_{3.5}\text{Al}_{0.5}\text{Ti}_{0.5}\text{O}_{19}$ ), which consist of both the hexagonal closed-packed (HCP) and the face-centered-cubic structures as shown in Figure 1.2. In the BaM unit cell the oxygen atoms are close-packed with the Ba and Fe ions in the interstitial sites. There are ten layers of oxygen atoms along the  $c$ -axis which is the magnetic easy axis. The structure is built up from smaller units: a cubic block S, having the spinel-type structure, and a hexagonal block R, containing the  $4fVI$ , and  $12k$ , respectively [9-11]. The structure is symbolically described as  $\text{RSR}^*\text{S}^*$  where R is a three-layer block, two  $\text{O}_4^-$  containing one  $\text{BaO}_3$  with composition  $(\text{Ba}^{2+}\text{Fe}_6^{3+}\text{O}_{11}^{2-})^2$ , and S is a two  $\text{O}_4^-$  layer block with composition  $(\text{Fe}_6^{3+}\text{O}_8^{2-})^{2+}$ , where the asterisk means that the corresponding block has been turned  $180^\circ$  around the hexagonal  $c$ -axis. The smaller  $\text{Fe}^{3+}$  ions are arranged in five different kinds of interstitial sites. Three are octahedral sites  $12k$ ,  $4fVI$ , and  $2a$ , one is a tetrahedral site,  $4fIV$ , and the last one is a site in which the ferric ion is surrounded by five oxygen atoms forming a trigonal bipyramid,  $2b$ . Each crystal site has a different number of  $\text{Fe}^{3+}$  ion per molecular and single ion magnetocrystalline anisotropy [12], as shown in Table 1.2. Magnetocrystalline anisotropy of  $2b$  site has the highest value than that of other sites, so the magnetocrystalline anisotropy of BaFe can be modified by the addition of other dopant elements, such as  $\text{Co}^{2+}$ ,  $\text{Ti}^{4+}$ ,  $\text{Sn}^{2+}$ ,  $\text{Nb}^{4+}$ , and  $\text{Zn}^{2+}$  [13-19]. The total magnetic moment of BaM per molecular is  $20 \mu_B$  because of 8 ions spin in one direction and 4 ions spin in the other direction, as shown in Figure 1.2. The saturation magnetization of BaM at room temperature is  $72 \text{ emu/g}$  due to the orbital motion of the electrons, and the Curie temperature is  $732 \text{ K}$  [8-9].

	2a	2b	4fIV	4fVI	12k
Position	Octahedral	Hexahedral	Octahedral	Tetrahedral	octahedral
Number of Fe <sup>3+</sup> ion/molecular	1	1	2	2	6
K <sub>1</sub> (cm <sup>-1</sup> /ion)	0.23	1.40	0.18	0.51	-0.18
Spin direction	up ↑	up↑	down↓	down↓	up↑

Table 1.2 Barium ferrite magnetic site and calculated K<sub>1</sub> for Fe<sup>3+</sup> by single ion anisotropy model [12].

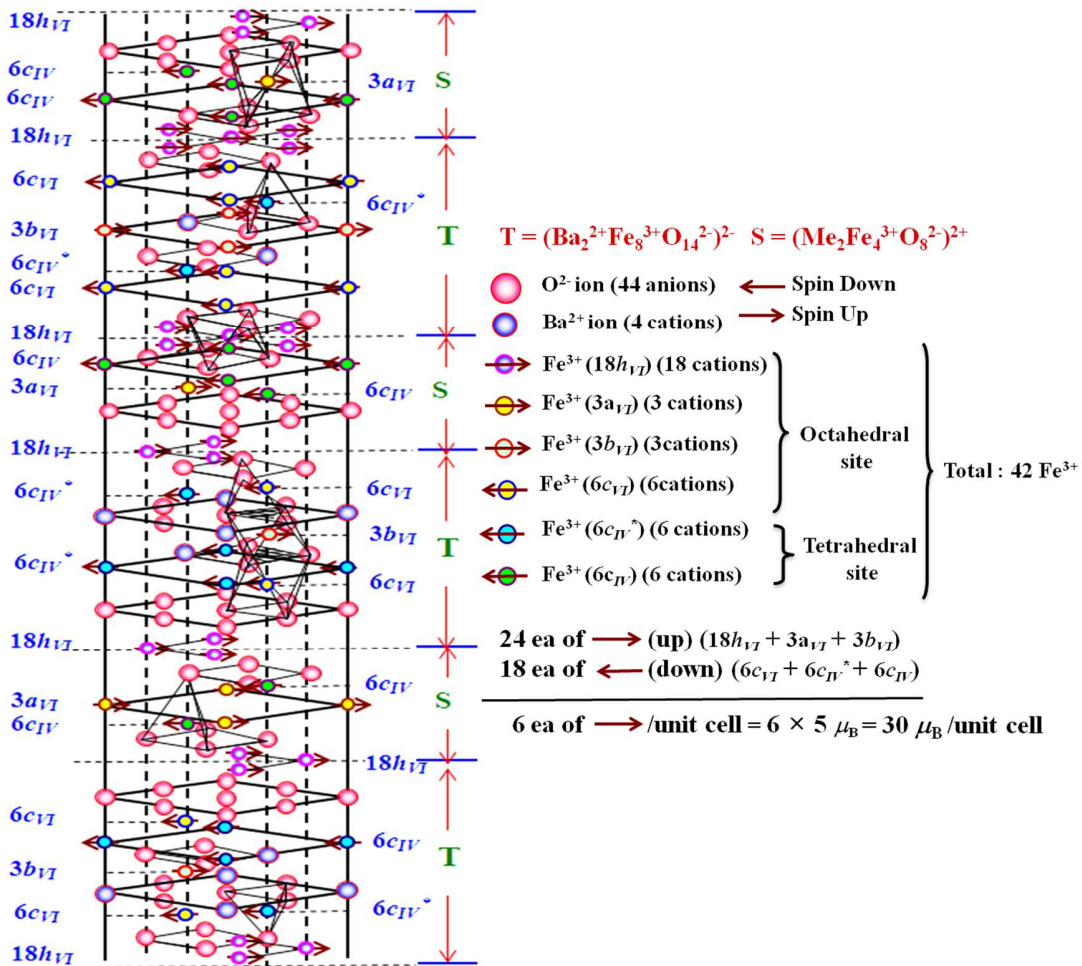


Figure 1.3 Magnetic structure of Y-Type hexaferrites (Ba<sub>2</sub>Me<sub>2</sub>Fe<sub>12</sub>O<sub>22</sub>) [9].

## 1.2. Y-type barium ferrite

Among the hexaferrites, Y-type hexaferrite  $\text{Ba}_2\text{Me}_2\text{Fe}_{12}\text{O}_{22}$  (Me = Zn, Mg, Co, Mn, Cu, Ni) is unique due to its in-plane (planar) magnetization bounded to the basal plane of the crystal structure [9]. This unique planar nature of the Y-type hexaferrite satisfies the requirement for next generation ferrite phase shifters and isolators, since planar circuits are easy to be fabricated and integrated with semiconductor devices [20-21]. The crystal  $\text{Ba}_2\text{Me}_2\text{Fe}_{12}\text{O}_{22}$  belongs to the space group  $\text{R}\bar{3}\text{m}$  and is constructed from a stacking of the spinel block S ( $\text{Me}_2\text{Fe}_4^{3+}\text{O}_8^{2-}$ )<sup>2+</sup> and the T ( $\text{Ba}_2^{2+}\text{Fe}_8^{3+}\text{O}_{14}^{2-}$ )<sup>2-</sup> block along the *c*-axis as shown in Figure 1.3. These blocks consist of close-packed oxygen and barium layers with metal ions occupying the tetrahedral and the octahedral sites. At room temperature, the *c*-axis unit cell length is 43.584 Å and has 18 oxygen layers. There are four octahedral sites consisting of  $18h_{VI}$ ,  $3a_{VI}$ ,  $3b_{VI}$ ,  $6c_{VI}$ ,  $6c_{IV}$  and  $4f_{VI}$ , and two tetrahedral sites of  $6c_{IV}^*$  and  $6c_{IV}$ . The total magnetic moment of Y-type hexaferrites per molecular can be calculated from the 24 ions spin in one direction and 18 ions spin in the other direction, resulting in 6 ions which gives 30  $\mu_B$ /unit cell as shown in Figure 1.3. Recently there has been a great interest for substituting metal cations for  $\text{Fe}^{3+}$  and  $\text{Ba}^{2+}$  in Y-type hexaferrites to tailor their magnetic and physical properties of these ferrites [22-27] For example, saturation magnetization ( $\sigma_s$ ) of polycrystalline  $\text{Ba}_2\text{Zn}_2\text{Fe}_{12}\text{O}_{22}$  (Zn-Y) hexaferrite was increased by substituting  $\text{Co}^{2+}$  and  $\text{Cu}^{2+}$  for  $\text{Zn}^{2+}$  from 30 emu/g to 36 emu/g [22], but large magnetic loss was observed.  $\text{Sr}^{2+}$  substitution for  $\text{Ba}^{2+}$  in polycrystalline  $\text{Ba}_{2-x}\text{Sr}_x\text{Zn}_2\text{Fe}_{12}\text{O}_{22}$  hexaferrite showed a decrease in  $\sigma_s$  and increase in permittivity with Sr content from  $x = 1.0$  to 1.5 [23]. Savage et al. showed that a small quantity of  $\text{Mn}^{2+}$  substitution in single crystalline Zn-Y decreased the ferrimagnetic resonance (FMR) linewidth to 3.8 Oe at 9 GHz [24]. Also, Y-type hexaferrites single crystals of the composition  $\text{Ba}_2\text{Mg}_2\text{Fe}_{12}\text{O}_{22}$  (Mg-Y) and  $\text{Sr}_{1.5}\text{Ba}_{0.5}\text{Zn}_2\text{Fe}_{12}\text{O}_{22}$  (SrBa-Y)

showed a strong response to electric polarization and magnetization at room temperature which opens a potential for room temperature magnetoelectric (ME) devices and also magnetically controlled electro-optical devices [25-26]. Chun et al. showed that a small amount of Al substitution into SrBa-Y hexaferrite remarkably decrease the critical magnetic field ( $B$ ) for switching electric polarization ( $P$ ) from 1 T down to 1 mT, and the ME susceptibility is greatly enhanced to reach a giant value of  $2.0 \times 10^4$  ps/m at an optimum  $x = 0.08$  compared to  $4.3 \times 10^1$  ps/m for  $x = 0$  [27].

### 1.3. Magnetic and microwave properties of hexagonal ferrites

#### 1.3.1. Saturation magnetization

In hexaferrites the ferrimagnetic ordering is as a result of superexchange interactions between the magnetic ions. Oxygen ions are usually positioned between the magnetic cation ion elements. The divalent oxygen anions ( $O^{2-}$ ) have no net magnetic moment, because they have a completely filled sub shells. The strongest interaction takes place when the  $Fe^{3+}$  to  $O^{2-}$  to  $Fe^{3+}$  bond approaches angles close to 180 degree. However, when the angle is close to 90 degrees, direct exchange predominates. For M-type barium ferrite the saturation magnetization at room temperature was obtained to be  $4\pi M_s = 4770$  gauss and the Néel temperature is around 740 K [8-9]. Among the Y-type hexaferrites  $Ba_2Zn_2Fe_{12}O_{22}$  (Zn-Y) has the highest saturation magnetization of  $4\pi M_s = 2850$  gauss at room temperature while  $Ba_2Ni_2Fe_{12}O_{22}$  (Ni-Y) has the lowest saturation magnetization of be  $4\pi M_s = 1600$  gauss at room temperature respectively [8-9].

### 1.3.2. Magnetocrystalline anisotropy field

The total energy of the magnetic system depends on the individual orientation of the magnetic moments in the crystal. The energy density of the anisotropic components ( $F_A$ ) has 2 and 6-fold symmetry, and can be written as the equation below [8-9].

$$F_A = K_1 \sin^2 \theta + K_2 \sin^4 \theta + K_3 \sin^6 \theta + K_4 \sin^6 \theta \cos^6 \phi + \dots \quad (1.1)$$

The angles,  $\theta$  and  $\phi$ , given in the Eq (1.1) represent the angles between  $c$ -axis and magnetization vector and also the projection of the magnetization vector in the basal plane and the basal axes respectively. For BaM,  $K_2$ ,  $K_3$ ,  $K_4$ , etc. are negligible, because BaM has strong uniaxial anisotropy along the  $c$ -axis. For Y-type hexaferrites where the magnetization is in the preferred plane the combination of  $K_1 + 2K_2$  is measured.

In general,  $H_A$  is defined as the magnetocrystalline anisotropy field.  $H_A$  for uniaxial materials where the magnetization is along the  $c$ -axis is given by,  $H_A = 2K_1/M_s$  and if the magnetization is in the basal plane or in-plane of the crystal then,  $H_A = -2(K_1 + 2K_2)/M_s$ . For, BaM  $K_1$  at 300 K was found to be  $3.2 \pm 0.1 \times 10^6$  ergs/cm<sup>3</sup> and  $K_1 + 2K_2$  for Zn-Y hexaferrites is  $-1.0 \times 10^6$  ergs/cm<sup>3</sup> [8-9]. The magnetocrystalline anisotropy field at 300 K for BaM is 17 kOe, and for Zn-Y hexaferrites is 9.0 kOe, respectively [8-9]. The value of  $H_A$  was found to be temperature dependent, and  $H_A$  vanished near the Néel temperature.

### 1.3.3. Magnetic domains, coercive field, and remanence

Ferromagnetic or ferrimagnetic materials get their magnetic properties not only because their atoms carry a magnetic moment but also because the material is made up of small regions known as magnetic domains. In each domain, all of the atomic dipoles are coupled together in a preferential direction. The magnetic domains are separated by a thin “wall”, also called Bloch

wall, in which the direction of the magnetization gradually changes from one orientation to another [8]. In general, barium ferrite single crystals have multi-domains, so that the net magnetization of the BaM single crystal exhibit zero moment at no applied external magnetic field. Therefore, coercivity ( $H_c$ ) is found to be near zero for BaM single crystal. However, the magnetization reaches saturation,  $4\pi M_s$ , for  $H \sim H_A$  or  $H_c \sim H_A$ . The study of magnetic domain patterns in bulk single crystals of hexaferrite is very interesting and is discussed in detail later in Chapter 7 of this dissertation.

The remanence moment ( $M_r$ ), is the residual magnetic moment with no external field. For instant, single domain material should have  $M_r \sim M_s$  [8]. In the case of multi-domains single crystal of barium ferrite  $M_r$  is  $\sim 0$  gauss. In order to prepare BaM materials for which  $M_r \sim M_s$ , either demagnetization factors ( $N_x$ ,  $N_y$ , and  $N_z$ ) or coercive field ( $H_c$ ) should be zero or equal to  $4\pi M_s$ , respectively. However, large  $H_c$  usually indicate high magnetic loss (large ferrimagnetic resonance linewidth,  $\Delta H$ ), which is also detrimental for preparing low loss magnetic materials and devices.

#### 1.3.4. Microwave properties-permeability tensor and ferromagnetic resonance

For an applied magnetic field  $\vec{B}$  in a magnetic material, the magnetic dipole moments of electrons in atoms and molecules can be aligned to produce a magnetic polarization or magnetization  $\vec{M}$ . The total magnetic flux density  $\vec{B}$  is given by:

$$\vec{B} = \mu_0 (\vec{H} + \vec{M}) \quad (1.2)$$

for a linear, isotropic magnetic material, the magnetisation  $\vec{M}$  is linearly related to the applied field  $\vec{H}$  by :

$$\vec{M} = \chi_m (\vec{H}) \quad (1.3)$$

where  $\chi_m$  is the magnetic susceptibility of the medium. Combining equations (1.2) and (1.3), we obtain

$$\vec{B} = \mu_0 (1 + \chi_m) \vec{H} = \mu \vec{H} \quad (1.4)$$

where  $\mu_0$  is the permeability of the magnetic material. For anisotropic magnetic materials, such as hexaferrites equation (1.4) assumes a tensor form written as:

$$\begin{bmatrix} B_x \\ B_y \\ B_z \end{bmatrix} = \begin{bmatrix} \mu_{xx} & \mu_{xy} & \mu_{xz} \\ \mu_{yx} & \mu_{yy} & \mu_{yz} \\ \mu_{zx} & \mu_{zy} & \mu_{zz} \end{bmatrix} \begin{bmatrix} H_x \\ H_y \\ H_z \end{bmatrix} \quad (1.5)$$

The equation (1.5) is also called as the magnetic permeability tensor of the ferrite. This can be derived by considering the microscopic behavior of a ferrimagnetic material and its interaction with a microwave signal which is described below.

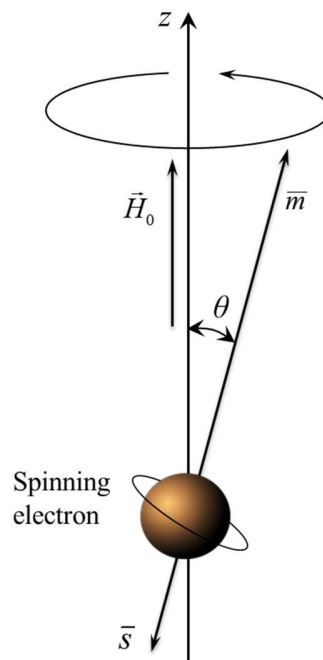


Figure 1.4 Spin magnetic dipole moment and angular momentum vectors for a spinning electron [29].

## Permeability Tensor

The magnetic properties of a material are due to the existence of magnetic dipole moments, which arise primarily from electron spin. From quantum mechanical considerations, the magnetic dipole moment of an electron due to its spin is given by [28-29]:

$$m = \frac{e\hbar}{2m_e} \quad (1.6)$$

where  $\hbar$  is the ratio of the Planck's constant divided by  $2\pi$ ,  $e$  is the charge of the electron and  $m_e$  is the mass of an electron. The contribution of the magnetic moment by the orbital motion of the electron is ignored as it is insignificant compared to the contribution from its spin. The electron spin angular momentum given by

$$s = \frac{\hbar}{2} \quad (1.7)$$

the gyromagnetic ratio is given by

$$\gamma = \frac{m}{s} = \frac{q}{m_e} = 1.759 \times 10^{11} \text{ C/kg} \quad (1.8)$$

with the spin angular momentum opposite in direction to the magnetic moment as shown in Figure 1.4, we can write,

$$\vec{m} = -\gamma\vec{s} \quad (1.9)$$

if an external magnetic field  $H_0$  is applied in the  $z$ -direction, a torque  $\tau$  will be introduced on the magnetic moment, given by

$$\vec{\tau} = \vec{m} \times \vec{B}_0 = -\mu_0\gamma\vec{s} \times \vec{H}_0 \quad (1.10)$$

using the classical relation that torque is equal to the rate of change of angular momentum

( $\tau = \frac{ds}{dt}$ ), we then obtain

$$\frac{d\vec{M}}{dt} = -\mu_0 \gamma \vec{m} \times \vec{H}_0 \quad (1.11)$$

if there are  $N$  magnetic dipoles per unit volume, the total magnetization  $\vec{M}_{tot}$  is

$$\vec{M}_{tot} = n\vec{M} \quad (1.12)$$

and so the equation (1.11) becomes

$$\frac{d\vec{M}_{tot}}{dt} = -\mu_0 \gamma \vec{M}_{tot} \times \vec{H}_{tot} \quad (1.13)$$

where  $\vec{H}_{tot}$  is the internal magnetic field.

Suppose we apply a modulated alternating magnetic field  $\vec{H}$  in an arbitrary direction to the static magnetic field  $\vec{H}_0 = H_0 \vec{z}$  in the  $z$ -direction where the modulated field can represent an electromagnetic wave passing through the material. The modulated field will cause a precession of the magnetic dipoles about the  $\vec{H}_0$  axis. For simplicity, we can assume that there is no demagnetization effects and that the crystal anisotropy (magnetostriction) is zero. Hence, the total magnetic field (assuming  $|\vec{H}_0| \gg |\vec{H}|$ ) is

$$\vec{H}_{tot} = H_0 \vec{z} + \vec{H}, \quad (1.14)$$

with the corresponding total magnetization vector  $\vec{M}_{tot}$  given by

$$\vec{M}_{tot} = M_s \vec{z} + \vec{M}, \quad (1.15)$$

where  $M_s$  is the saturation magnetization due to the static field and  $\vec{M}$  is the alternating magnetization due to the modulated field. Here, we have assumed that  $H_0$  is large enough to saturate the magnetization. Putting equations (1.14) and (1.15) into the equation of motion (1.13), we obtain the following three coupled equations of motion:

$$\frac{dM_x}{dt} = -\mu_0 \gamma M_y (H_0 + H_z) + \mu_0 \gamma H_y (M_s + M_z), \quad (1.16)$$

$$\frac{dM_y}{dt} = \mu_0 \gamma M_x (H_0 + H_z) + \mu_0 \gamma H_x (M_s + M_z), \quad (1.17)$$

$$\frac{dM_z}{dt} = -\mu_0 \gamma M_x H_y + \mu_0 \gamma H_x M_y. \quad (1.18)$$

to simplify the above equations, we note that  $|\vec{H}||\vec{M}| \ll |H_0||\vec{M}|$  and  $|\vec{H}||\vec{M}| \ll |\vec{H}||M_s|$  so that we can

ignore all products of the components of  $\vec{M}$  and  $\vec{H}$ . Along with defining  $\omega_0 = \mu_0 \gamma H_0$  (resonance

frequency) and  $\omega_m = \mu_0 \gamma M_s$  (magnetization frequency), we have the following simplified

equations of motion:

$$\frac{dM_x}{dt} = -\omega_0 M_y + \omega_m H_y, \quad (1.19)$$

$$\frac{dM_y}{dt} = \omega_0 M_x - \omega_m H_x, \quad (1.20)$$

$$\frac{dM_z}{dt} = 0. \quad (1.21)$$

solving equations (1.19) and (1.20) for  $M_x$  and  $M_y$  gives

$$\frac{d^2 M_x}{dt^2} + \omega_0^2 M_x = -\omega_m \frac{dH_y}{dt} + \omega_0 \omega_m H_x, \quad (1.22)$$

$$\frac{d^2 M_y}{dt^2} + \omega_0^2 M_y = -\omega_m \frac{dH_x}{dt} + \omega_0 \omega_m H_y. \quad (1.23)$$

assuming that the  $\vec{H}$  field has a time dependence of  $e^{j\omega t}$ , we can then rewrite equations (1.22)

and (1.23) into the following phasor form:

$$(\omega_0^2 - \omega^2) M_x = j\omega_m \omega H_y + \omega_0 \omega_m H_x, \quad (1.24)$$

$$(\omega_0^2 - \omega^2) M_y = -j\omega_m \omega H_x + \omega_0 \omega_m H_y, \quad (1.25)$$

from (1.24) and (1.25), we can then easily obtain matrix form as follows:

$$\begin{bmatrix} M_x \\ M_y \\ M_z \end{bmatrix} = \begin{bmatrix} \chi_{xx} & \chi_{xy} & 0 \\ \chi_{yx} & \chi_{yy} & 0 \\ 0 & 0 & 0 \end{bmatrix} \begin{bmatrix} H_x \\ H_y \\ H_z \end{bmatrix}, \quad (1.26)$$

where,

$$\chi_{xx} = \frac{\omega_m \omega_0}{(\omega_0^2 - \omega^2)} = \chi_{yy}, \quad (1.27)$$

$$\chi_{xy} = \frac{j\omega\omega_m}{(\omega_0^2 - \omega^2)} = -\chi_{yx}, \quad (1.28)$$

in order to obtain the tensor permeability, we have  $\vec{B} = \mu_0(1 + \chi)\vec{H}$ . Hence,

$$\vec{B} = \mu_0 \left( \begin{bmatrix} 1 & 0 & 0 \\ 0 & 1 & 0 \\ 0 & 0 & 1 \end{bmatrix} + \begin{bmatrix} \chi_{xx} & \chi_{xy} & 0 \\ \chi_{yx} & \chi_{yy} & 0 \\ 0 & 0 & 0 \end{bmatrix} \right) \vec{H} = [\mu]\vec{H}, \quad (1.29)$$

where,

$$[\mu] = \begin{bmatrix} \mu & j\kappa & 0 \\ -j\kappa & \mu & 0 \\ 0 & 0 & \mu_0 \end{bmatrix} \quad (z\text{-biased}), \quad (1.30)$$

with the Polder tensor elements given by

$$\mu = \mu_0 \left( 1 + \frac{\omega_m \omega_0}{(\omega_0^2 - \omega^2)} \right), \quad (1.31)$$

$$\kappa = \mu_0 \frac{\omega\omega_m}{(\omega_0^2 - \omega^2)}, \quad (1.32)$$

similarly, the tensor permeability  $[\mu]$  for  $\vec{H}_0$  in the  $\bar{x}$  and  $\bar{y}$  directions are given by

$$[\mu] = \begin{bmatrix} \mu_0 & 0 & 0 \\ 0 & \mu & j\kappa \\ 0 & -j\kappa & \mu \end{bmatrix} \quad (x\text{-biased}), \quad (1.33)$$

$$[\mu] = \begin{bmatrix} \mu & 0 & -j\kappa \\ 0 & \mu_0 & 0 \\ j\kappa & 0 & \mu \end{bmatrix} \text{ (y-biased),} \quad (1.34)$$

It is important to note that the permeability tensor is anti-symmetric, a condition which is necessary for nonreciprocal microwave devices such as the circulators and isolators.

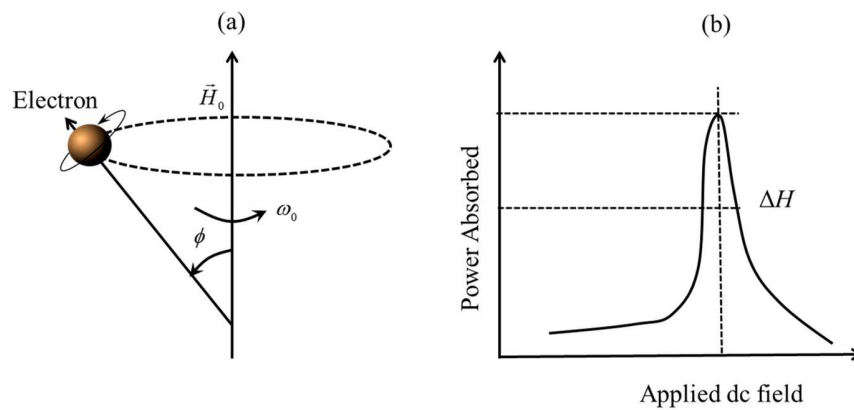


Figure 1.5 (a) Precession of a spinning unpaired electron at frequency  $\omega_0$  about a static dc magnetic field (b) resonance absorption curve as a function of applied magnetic field.

### Ferromagnetic Resonance

In many microwave applications, the microwave excitation is in the form of a plane-polarized wave having both magnetic and electric field components whose directions are perpendicular to each other. This plane polarized wave is propagated through a metallic waveguide whose dimensions are fixed by the wave-length, which in turn is determined by the microwave frequency in the application. The linearly polarized wave can be considered to be composed of a combination of two counter-rotating circularly-polarized waves, one designated by a effective permeability,  $\mu^+$ , called as right-hand circularly polarized (RHCP) wave represented as [28-29]:

$$\mu^+ = \mu_0 \left( 1 + \frac{\omega_m}{(\omega_0 - \omega)} \right) = \mu + \kappa, \quad (1.35)$$

and another designated by an effective permeability,  $\mu^-$ , called as left-hand circularly polarized field (LHCP) represented as

$$\mu^- = \mu_0 \left( 1 + \frac{\omega_m}{(\omega_0 + \omega)} \right) = \mu - \kappa, \quad (1.36)$$

these circularly polarized waves interact differently with magnetic dipole moments, depending on the direction of magnetization of the magnetized ferrite. The maximum coupling of the energy from the RF signal to the ferrite material will occur at ferrimagnetic resonance. If the direction of rotation or the frequency of the RF signal is changed, minimum coupling will occur. The uniform precession of the magnetic moments in the presence of an external bias field, satisfying the resonance condition of  $\omega_0 = \gamma H$ , is called ferromagnetic resonance. This effect is illustrated in Figure 1.5 where the electron is shown precessing with frequency  $\omega$  about the internal static dc field  $\vec{H}_0$  at an angle  $\phi$ . If the incident RF wave is of the same sense of polarization and the same frequency as the precession, then energy is coupled from the wave to increase  $\phi$  and the precession is maintained. The frequency  $\omega_0$  is called the resonance frequency and depends on the strength of the internal dc field in the ferrite and is in turn a function of the externally applied field and the internal demagnetizing field. A plot of power absorbed as a function of applied field at constant frequency results in the resonance absorption line shown in Figure 1.5 (b); the width of the resonance line is of great importance in the design of ferrite non-reciprocal devices since it implies the magnetic losses not only at resonance but also in the immediate vicinity. The parameter representing this width is the resonance linewidth ( $\Delta H$ ), measured at a point where the absorption is half its maximum value. It is desirable that  $\Delta H$ , be

minimized, implying maximum absorption, and this consideration is particularly valid in the case of the resonance circulator and isolators, where it is necessary to obtain a maximum ratio of attenuation in the isolation direction to that in the transmission direction [28].

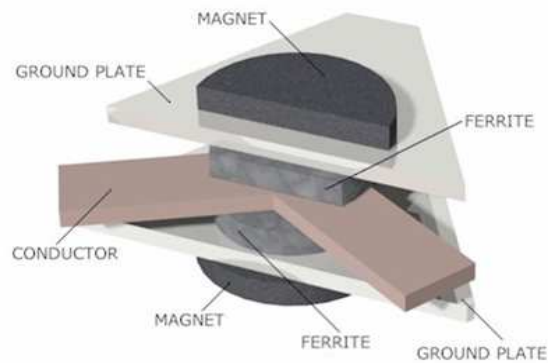


Figure 1.6 General schematic of a Y-junction stripline circulator [31].

#### 1.3.5. Applications of hexaferrites for microwave devices

The most important microwave device, utilizing the nonreciprocity of ferrites, is the circulator as shown in Figure 1.6. A circulator is a three or more port non-reciprocal device transmitting energy from one of its ports to an adjacent port while decoupling the signal from the third port [32-33]. In stripline type, two ferrite disks, one located on each side of the conductor. This makes the junction behave like a resonant cavity supporting two modes, clockwise and counter clockwise. The principle of operation of the circulator is to make use of the difference in propagation velocity in two directions in the ferrite. As described in an earlier section, the sense of the rotation of the magnetic moment is determined by the direction of the bias field. Thus, by changing the bias field direction, the interaction between RF field and the material can be controlled. For one direction of the field, the ferrite transmits the RF field, for the other direction absorbs it. As shown in Figure 1.7, the RF energy entering port 1 leaves port 2, while port 3 is

decoupled, the energy entering port 2 leaves port 3, while port 1 is decoupled; and power entering port 3 leaves port 1, while port 2 is decoupled.

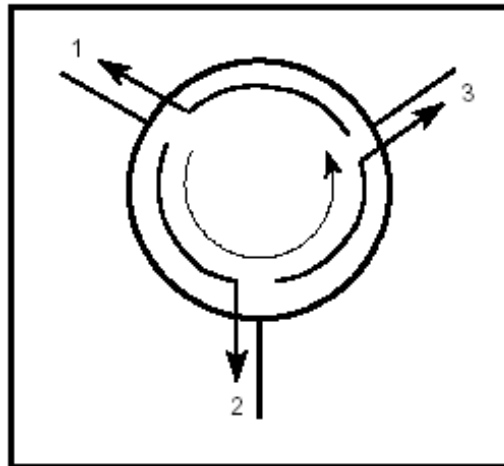


Figure 1.7 Energy flow diagram of the ferrite disk related to the port of the Y-junction circulator [30].

Due to limitations by losses, microwave ferrite devices such as circulators and isolators operate in a particular frequency range. High insertion loss can occur at very low biasing magnetic fields since the applied magnetic field is not sufficient to fully saturate or align the individual magnetic domains of the ferrite material. Circulators are designed to operate in the above resonance region, where magnetic losses are low. However, high magnitude of the internal magnetic field  $H_{in}$  is required to increase gyromagnetic resonance frequency  $\omega_0$ . The internal magnetic field in the ferrite is given by:

$$H_i = H_0 - H_d + H_A \quad (1.37)$$

where  $H_0$  is the applied magnetic field,  $H_d$  is the demagnetization field ( $4\pi N_d M_s$ ), and  $H_A$  is the anisotropy field. From the equation (1.37) a ferrite having a small anisotropy field needs a large applied magnetic field to cancel the demagnetization field from the shape of the ferrite sample.

Therefore, using a ferrite material having a high  $H_A$  is beneficial for microwave devices so that a high resonance frequency can be achieved and also minimizing the large external bias field needed for operation. Figure 1.8 shows the plot of anisotropy field  $H_A$  and the applied magnetic field  $H_0$  dependences of FMR frequency for a uniaxial barium ferrite sphere given by [34]:

$$f_{\text{resonance}} = \left( \frac{2.8 \text{ MHz}}{\text{Oe}} \right) (H_A + H_0) \quad (1.38)$$

from the plot, we can see that the resonance frequency of ferrite increases with increasing both anisotropy and applied magnetic fields respectively. Therefore, a ferrite (BaM) with high uniaxial anisotropy has a high resonance frequency, thereby high operating frequency of the RF device with a moderate external bias field or no magnetic field (self-biased) can be realized. On the other hand, a large external magnetic field is required to operate a RF device using a YIG material in the above resonance region.

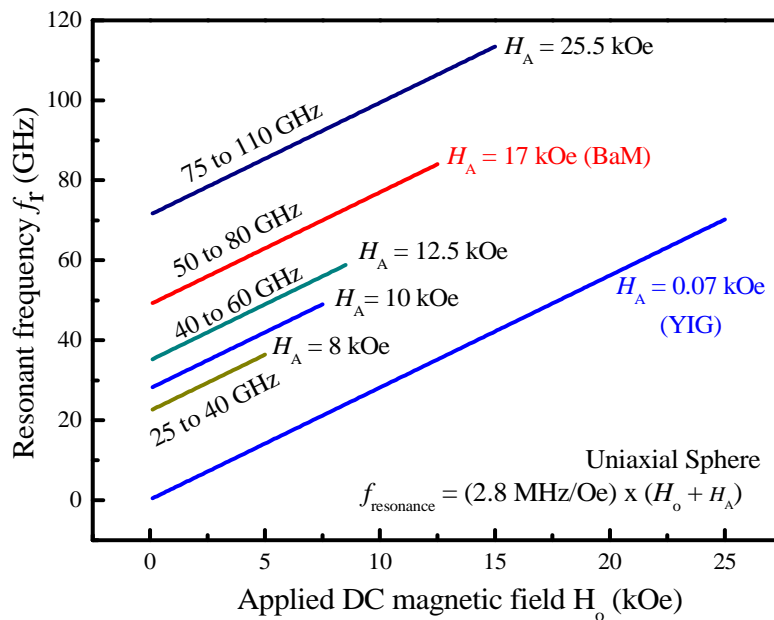


Figure 1.8 Ferrite resonance frequency as a function of dc magnetic field for various values of the anisotropy field [34].

Most recently, polycrystalline hexaferrites are being explored for their self-biased properties [54-55,69]. Traditional, Y-junction circulators need strong external bias fields provided by an external permanent magnet (Figure 1.6). As a result, size, weight and cost is increased, which is unfavorable when the trend towards miniaturization of ferrite devices is necessary. One way to realize this is to design and fabricate devices without any external permanent magnets which are called as “self-biased”. The requirements to achieve a self-bias state for a ferrite is to have a large remanent magnetization ( $M_r$ ), a large coercivity ( $H_c$ ) and a small demagnetization factor ( $N_d$ ). The relation between  $H_c$  and the demagnetization field ( $H_d = 4\pi N_d M_s$ ) needs to be satisfied to meet self-bias condition given as  $H_c > 4\pi N_d M_s$ . The coercivity in turn is given as  $H_c = C \left( \frac{2k}{M_s} \right) - N_d M_s$ . Where,  $K_1$  is the magnetic crystalline anisotropy constant,  $M_s$  is the saturation magnetization, and  $C$  is a coefficient. Single crystals of BaM thick films cannot be used for self-biased applications due to their negligible coercivity and remanence. Therefore, an external bias magnetic field needs to be applied to the film for use in RF circulator applications. On the other hand, oriented polycrystalline hexagonal ferrite can be used for the self-biased devices due to their large remanent magnetization and coercivity values. The demagnetization factor is moreover controllable by fabricating large out-of-plane uniaxial magnetic anisotropy ( $c$ -axis oriented) in the hexagonal ferrite.

## 2.0. Objectives

For RF devices such as circulators the most important magnetic parameters which include the saturation magnetization ( $4\pi M_s$ ), anisotropy field ( $H_A$ ) and FMR linewidth ( $\Delta H$ ) are critical to obtaining low insertion losses and high RF performance. The insertion loss means energy loss of RF input signal during the signal transmission to the output port. The FMR linewidth is associated with magnetic loss characteristics and depends on the intrinsic damping constant and extrinsic properties such as crystal quality, grain size and distribution, porosity, morphology, etc. Single crystal hexagonal barium ferrites possess a large uniaxial magnetic anisotropy and exhibit a narrow FMR linewidth due to its high crystallinity, low defect, and porosity. Therefore, single crystal barium ferrites are an excellent candidate for high-performance RF device applications with a moderate external bias field. This part of the dissertation is written in several chapters based on the authors published journal articles, with each chapter having its objective, literature review, and bibliography.

In chapter 3 a novel modified liquid phase epitaxy deposition (LPE) technique as a means of growing high quality thick BaM films onto semiconductor substrates was developed and the magnetic and microwave properties were discussed [35].

In chapter 4, 5 and 6 bulk single crystals of M and Y-type hexaferrite were grown in platinum crucibles by doping with several cation elements [36-38] using a high-temperature furnace. The improved magnetic and microwave properties were reported and discussed. Finally, in chapter 7, the study of magnetic domain patterns in bulk BaM single crystals on the basal and the prism plane were studied by using a magnetic force microscopy (MFM) technique [39].

### 3.0. Liquid phase epitaxy growth of BaM films

#### 3.1. Introduction

The realization of monolithic microwave integrated circuits (MMIC) is limited due to the difficulties in integrating bulk single crystal ferrite in semiconductor devices. One way to realize this is by growing thick BaM single crystalline films on semiconductor substrates. During the past few decades, several researchers worked on growing thick BaM film by various deposition techniques [40-44]. The most successful technique to grow thick BaM film is a flux method, referred to as an isothermal dipping method, namely liquid phase epitaxy (LPE) [42-44]. Liquid-phase epitaxy (LPE) is a process in which a single crystal film layer is grown from a dilute molten solution onto a flat oriented single crystal substrate. Deposition of the BaM on (111) MgO substrate by the LPE process resulted in the growth of 22.5  $\mu\text{m}$  thick BaM film [43], indicating that the deposition rate is too low for circulator application which require thick films  $> 100 \mu\text{m}$  [2]. The maximum attainable growth rate reported for BaM films deposited on  $\alpha\text{-Al}_2\text{O}_3$  (0001) substrate is 100  $\mu\text{m/h}$  [44]. However, the grown BaM films are magnetically in-plane oriented, and also, a seed layer was needed to achieve the above growth rate. Furthermore, the growth rate of BaM film deposited onto  $\text{Gd}_3\text{Ga}_5\text{O}_{12}$  (GGG) substrate by the LPE technique was limited to 45  $\mu\text{m/h}$  [42].

Selecting the right substrate to grow BaM film is also challenging. In this work we choose GGG substrate to grow the BaM thick film. GGG has a cubic structure with a lattice constant of 12.383  $\text{\AA}$  [45], and in the (111) direction the lattice constant is  $\sqrt{2} \times 12.383 = 17.512 \text{\AA}$ . However, BaM has a lattice constant of 5.89  $\text{\AA}$  which is almost 3 times lower than that of the

(111) oriented GGG substrate. Therefore, the lattice mismatch between the (111) GGG substrate and the  $a$ -axis corresponding to the 3 unit cells on the basal plane of the BaM can be given as:

$$\text{Lattice mismatch (\%)} = \frac{3a_{\text{BaM}} - a_{(111)\text{GGG}}}{3a_{\text{BaM}}} \cong 0.9 \%. \text{ In addition, the thermal expansion coefficient}$$

of GGG and BaM are  $9.2 \times 10^{-6}/^{\circ}\text{C}$  and  $10 \times 10^{-6}/^{\circ}\text{C}$ , respectively. The smaller thermal expansion coefficient difference between the substrate and the BaM film enables an epitaxial growth and avoids strains and cracking during the LPE growth. On the other hand, the thermal expansion coefficient of (0001) sapphire and MgO (111) substrate are  $7.8 \times 10^{-6}/^{\circ}\text{C}$  and  $13.6 \times 10^{-6}/^{\circ}\text{C}$ , respectively, that are too low (sapphire) or high (MgO) to grow thick BaM films which will lower the growth rate and also the quality of the films [42]. Yttrium iron garnet (YIG) films were successfully grown onto (111) oriented GGG substrates with a very high growth rate of  $\sim 60 \mu\text{m/h}$  [46-47], and also, it was previously reported that a very high growth rate can be expected by employing GGG substrates to deposit thick BaM films when compared to other substrates of MgO or sapphire [42]. In this chapter, we report out-of-plane oriented BaM thick films grown by LPE technique to achieve a growth rate of  $72 \mu\text{m/h}$  using GGG substrate with a flux system of  $\text{Fe}_2\text{O}_3 - \text{BaCO}_3 - \text{Na}_2\text{CO}_3$ .



Figure 3.1 Liquid phase epitaxy system.

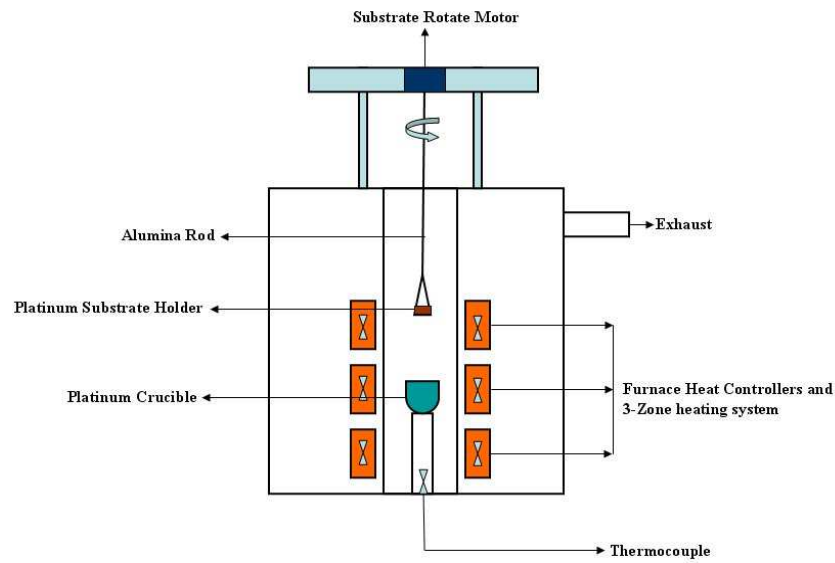


Figure 3.2 Schematic of LPE system.

### 3.2. Experimental

The growth of thick BaM films was performed by using an LPE system shown in Figure 3.1. The system is a custom build with a substrate loading system and a temperature controlled unit. It incorporates 3 zone heating with 3 independent heating elements and is also equipped with 5 type R thermocouple sensors (3 sensors for the 3 heating element, 1 sensor as a comparison sensor and 1 for over temperature protection). The flat zone consisting of the heating elements is 12" long, and the maximum wafer that can be processed inside the furnace is 3inch in diameter. The furnace chamber is further closed from the bottom and the top by thick porous alumina ceramics. A ceramic pedestal is constructed from separate pieces on the chamber bottom to raise the crucible position and to diminish thermal losses via the non-heated bottom region. The substrate is mounted with a platinum substrate holder attached to an alumina rod. The alumina rod is connected to lifting and rotation motors, which provide the substrate with vertical and axial movements as shown in Figure 3.2. The furnace is also equipped with an exhaust vent

area to capture and vent high-temperature gasses and a shutter mechanism for the alumina sample rotating shaft to pass through. The temperature inside the furnace is measured with an R-type thermocouple connected to a Eurotherm® temperature controller. It allows us to control the temperature with great precision. However, the displayed temperature does not represent the actual temperature inside the liquid solution but only shows the temperature close to the thermocouple tip.

BaM flux melt was prepared from a mixture of iron oxide ( $\text{Fe}_2\text{O}_3$ ), barium carbonate ( $\text{BaCO}_3$ ) and sodium carbonate ( $\text{Na}_2\text{CO}_3$ ) [48]. The mole ratio of 63.17 ( $\text{Fe}_2\text{O}_3$ ): 10.53 ( $\text{BaCO}_3$ ): 26.3 ( $\text{Na}_2\text{CO}_3$ ) were used for the growth of the BaM thick film. The mixture was ground and followed by calcination at 980 °C for 12 h. A platinum crucible was used to hold the melt. The crucible was heated initially to melt the mixture at an elevated temperature and was replenished with the mixture at regular intervals until all the carbonates decomposed into oxides and  $\text{CO}_2$ . After decomposition of the carbonates was complete, the crucible was shifted to the LPE system where it was re-heated to a temperature of 1250 °C and held for 10-12 h to homogenize the melt. Prior to dipping the substrate into the melt, the temperature of the furnace is slowly cooled to the growth temperature ranged from 1162 to 1150 °C. The substrate was preheated at a position of 5-10 mm above the melt for 20 min in order to reach thermal equilibrium with the solution, and it was slowly dipped into the melt to allow the growth of the BaM film. The melt was cooled at 4.5 °C/h during the growth, while maintaining rotation of the substrate at 20 to 50 rpm to avoid depletion of the melt content in the crucible and also to minimize the temperature gradient in the melt. A detailed flow chart of the LPE process is shown in Figure 3.3. Also, during the LPE growth by the vertical dipping technique, the substrate was only partially immersed in the liquid solution. This approach has been chosen because of two main reasons.

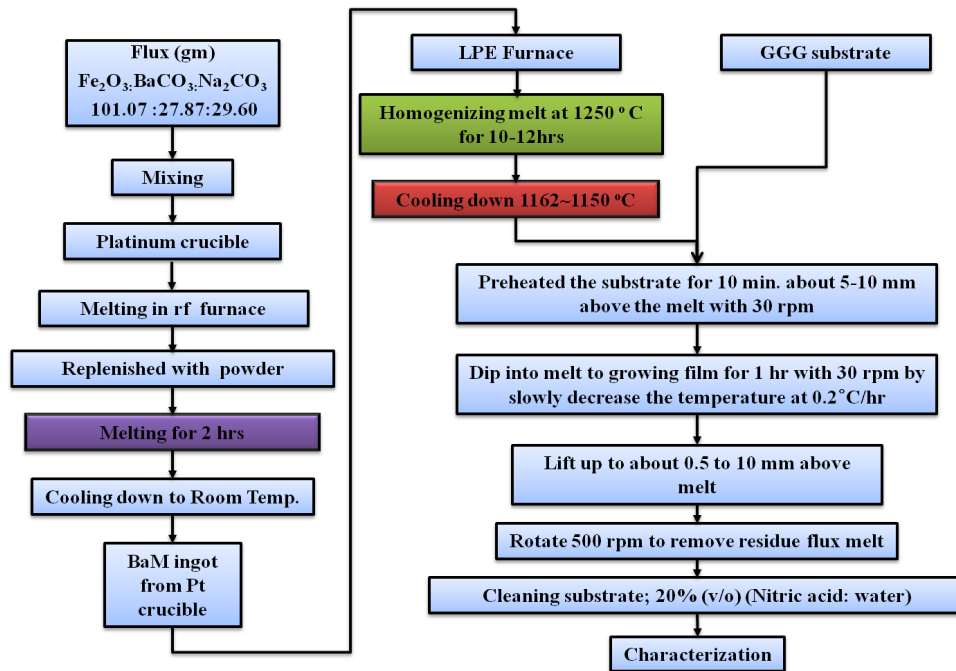


Figure 3.3 Flow chart of the LPE process to grow BaM thick films.

First, preliminary test experiments showed that at the interface where the substrate was in contact with the platinum (Pt) clamp fixture when immersed in the solution, the substrate always cracked. This occurs because of thermal shocks induced by the difference in thermal conductivities of BaM and Pt. However, when the substrate was partially dipped in the melt, the Pt wires stay above the liquid level and no substrate cracking was observed. Secondly, the non-immersed part of the substrate did not exhibit any layer growth, but only local surface contamination due to the solution evaporation that occurs. Therefore, the uncovered surface can also be used as a reference plane to measure precisely the layer thickness. This method was used to achieve a higher growth rate of the thick BaM film. After the removal of the deposited substrate from the melt, it was cleaned in a solution of hot dilute nitric acid to remove non-ferrite residues.

The thick BaM ferrite films were characterized for their magnetic and physical properties by a vibrating sample magnetometer (VSM), X-ray diffraction (XRD), and scanning electron microscopy (SEM). The microwave properties of the thick BaM films were characterized by an FMR measurement system by a standard field-swept shorted waveguide technique with an AC field modulation and lock-in detection [49]. The sample is attached on the side wall of the shorted waveguide and adjusted to the maximum ac magnetic field position. The static magnetic field is applied parallel to the easy axis of the BaM film which is the perpendicular direction to the sample film surface. In addition, to minimize the linewidth broadening caused by the modulation field, the smallest modulation field was chosen in the lock-in technique.

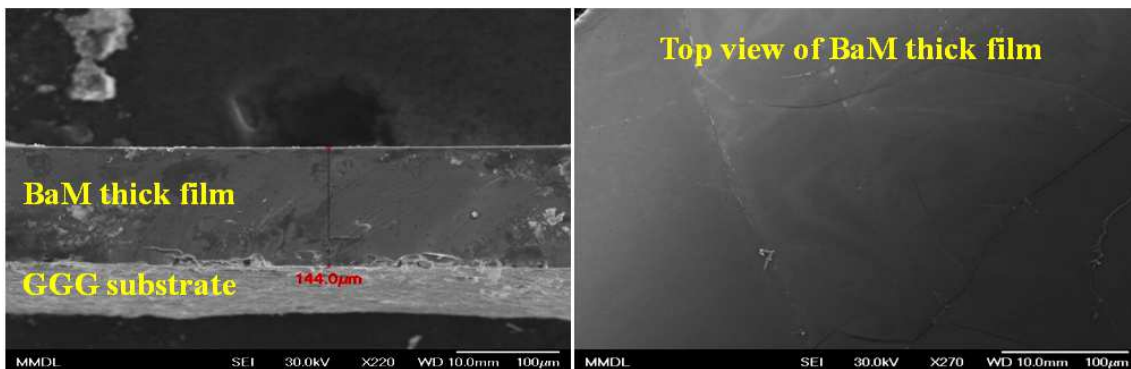


Figure 3.4 Scanning electron micrograph showing the cross sectional area and the top view of 144  $\mu\text{m}$  thick LPE processed BaM film.

### 3.3. Results and discussion

After two hours of LPE growth, the total thickness of BaM film on GGG substrate was measured to be 144  $\mu\text{m}$  by cross-sectional morphology of SEM as shown in Figure 3.4. The growth rate of the BaM films on the GGG substrate is 72  $\mu\text{m}/\text{h}$ , which is the highest known growth rate achieved by the LPE technique. This higher growth rate, as compared to the previously reported rate of 45  $\mu\text{m}/\text{h}$  [8], may be attributed to the use of a new flux system of

$\text{Fe}_2\text{O}_3$  -  $\text{BaCO}_3$  -  $\text{Na}_2\text{CO}_3$  and partial immersion of substrate in the melt of  $\text{Fe}_2\text{O}_3$  -  $\text{BaO}$  -  $\text{Na}_2\text{O}$ .

The crystal structure of the BaM thick film was confirmed by an X-ray diffractometer. The crystalline film reflects all the (000*l*) planes of BaM, which identifies the *c*-axis orientation of the BaM thick film as shown in Figure. 3.5 The crystalline orientation was also determined by the magnetic torque curves which were taken on the thick BaM film at an applied field of 10 kOe. The plane of the disk was rotated both clockwise (CW) and counter-clockwise (CCW) in the applied field. As shown in Figure 3.6, the film exhibits a uniaxial symmetry when the applied field is normal to the film plane near  $10^\circ$  and  $190^\circ$ . This implies that the anisotropy energy is minimum in the easy direction of the magnetization. The curves corresponding to the angles of  $100^\circ$  and  $280^\circ$  show a positive slope, implying hard alignment of the magnetization in the in-plane direction at 10 kOe.

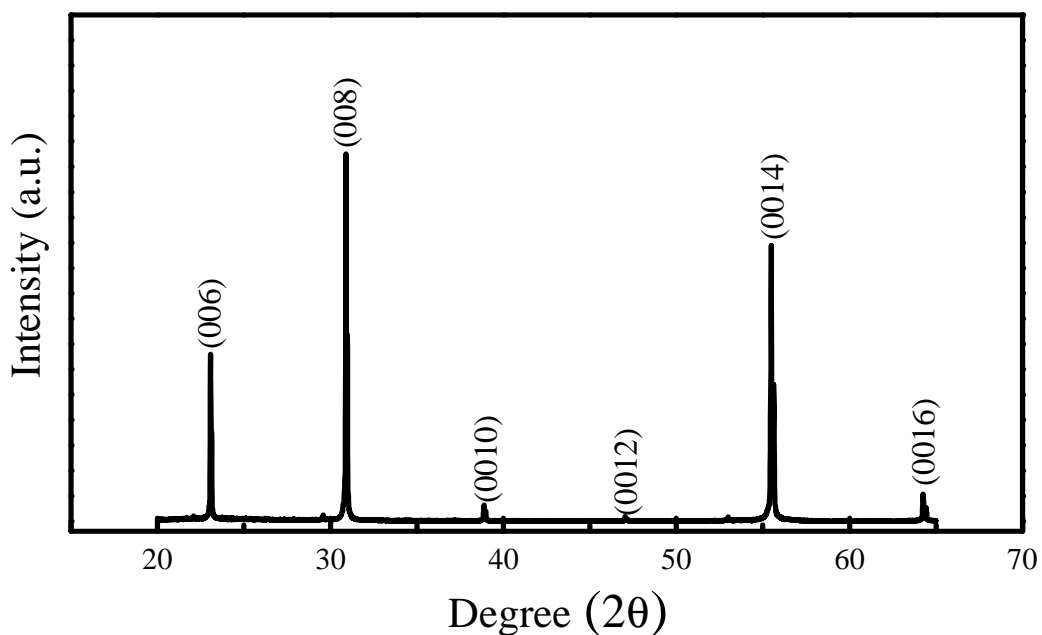


Figure 3.5 X-ray diffraction pattern of 144  $\mu\text{m}$  thick BaM film on (111) GGG substrate.

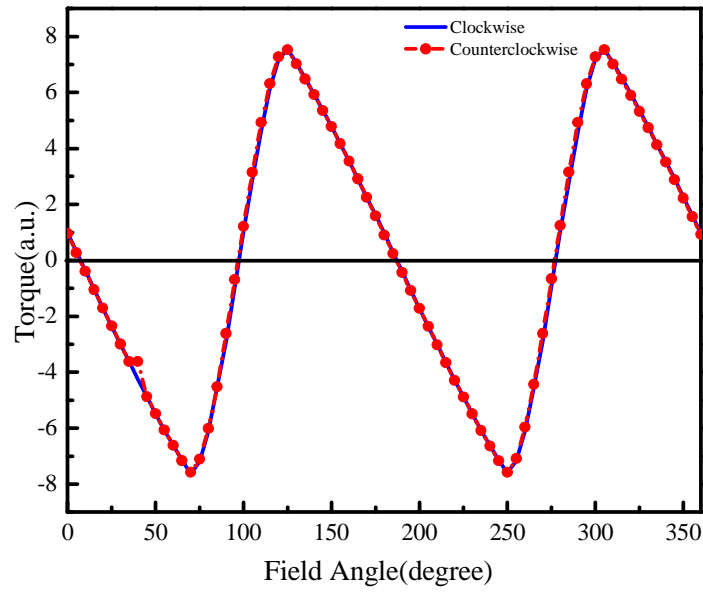


Figure 3.6 Torque measurement of 144  $\mu\text{m}$  thick BaM film on (111) GGG substrate at  $H_{\text{App}} = 10$  kOe.

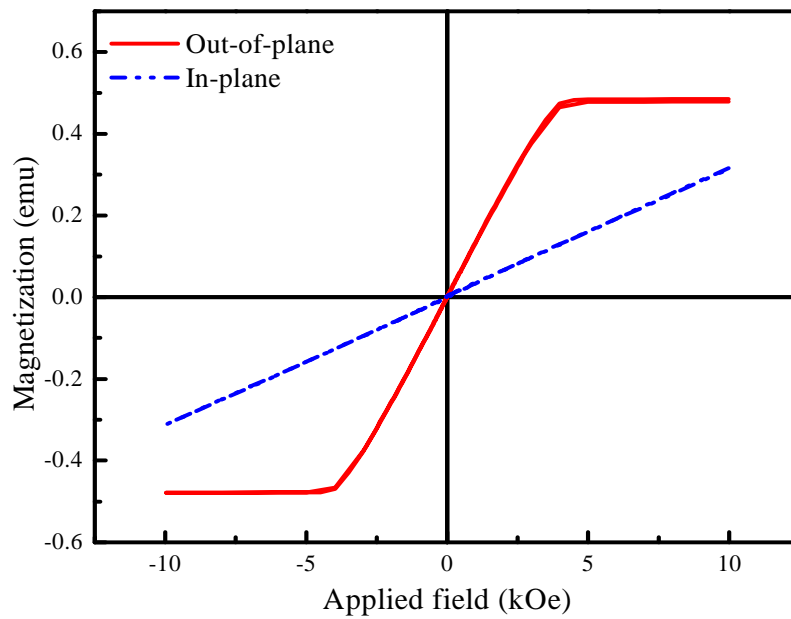


Figure 3.7 Magnetic hysteresis loop of 144  $\mu\text{m}$  thick BaM film on (111) GGG substrate.

Figure 3.7 shows the Magnetic hysteresis loop of the 144  $\mu\text{m}$  thick BaM film on (111) GGG substrate. It is confirmed from the hysteresis loop that the 144  $\mu\text{m}$  thick LPE processed

BaM film possesses uniaxial magnetic anisotropy. The saturation magnetization ( $4\pi M_s$ ) in the out-of-plane direction was found to be 4.2 kG at room temperature. The in-plane magnetization, however, shows no saturation at a maximum applied field of 10 kOe due to the high crystalline anisotropy field ( $H_A$ ) of the film. The coercive field of the LPE processed thick film was 3.8 Oe, implying that the films have relatively small defects and voids. The uniaxial anisotropy field for the 144  $\mu\text{m}$  film was estimated by the following equation [50]:

$$H_{\text{sat (hard)}} = H_k + 4\pi N_t M_s \quad (2.1)$$

For  $H_{\text{app}}$  along the easy direction, the magnetization is linear in  $H_{\text{app}}$  below saturation which occurs at  $H_{\text{sat (easy)}} = 3.9$  kOe, and  $H_{\text{sat (hard)}}$  is estimated to be 16.0 kOe by extrapolating the out-of-plane and in-plane curves to their intersection point. Assuming a density of 5.29  $\text{g/cm}^3$  for BaM [9], the saturation magnetization is obtained to be 4205 G. The demagnetizing factor,  $N_n$ , in the easy plane direction of the crystal is given by:

$$N_n = \frac{H_{\text{sat (easy)}}}{4\pi M_s} = \frac{3900}{4205} = 0.92 \quad (2.1)$$

the estimated demagnetization in the film plane of the crystal is,  $N_t = (1 - N_n) / 2 = 0.04$ , and  $4\pi M_s = 4205$  G yield 0.168 kOe of  $4\pi N_t M_s$ . Therefore,  $H_{\text{sat (hard)}} \cong H_k$  by equation (2.1) since  $4\pi N_t M_s$  is small and negligible. This means that the crystalline anisotropy of the 144  $\mu\text{m}$  thick BaM film is close to 16 kOe of  $H_{\text{sat (hard)}}$  and this film is of very high quality. With regard to microwave properties, room temperature FMR measurements have been performed on the 144  $\mu\text{m}$  thick BaM film with a shorted waveguide technique. The sample is mounted on the side wall of Ka band waveguide, and the static field is applied in the perpendicular direction to the film. From the shorting plate at the bottom of the waveguide, the sample position is adjusted to the maximum AC magnetic field position inside the waveguide. Also, to remove the linewidth

broadening caused by the modulation field, the smallest modulation field is chosen in the lock-in technique. The FMR condition used for the measurement is [28]

$$\frac{f_r}{\gamma} = (H_{res} + H_A - 4\pi M_s) \quad (3.3)$$

where  $f_r$  is the resonance frequency in GHz,  $H_{res}$  is the resonance external field in kOe,  $H_A$  is the anisotropy field, and  $\gamma' = \gamma/2\pi = 2.788$  GHz/kOe.

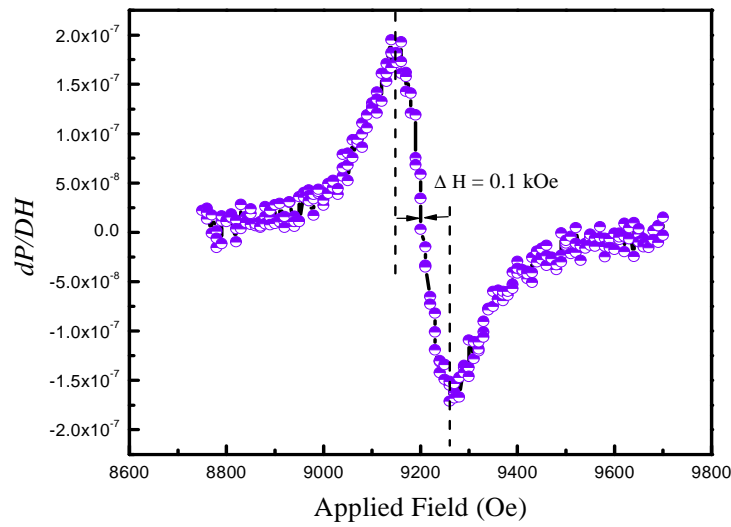


Figure 3.8 FMR linewidth of the 144  $\mu\text{m}$  thick BaM film.

Figure 3.8 shows the differential power absorbed  $dP/dH$  with an applied field. A ferrimagnetic resonance linewidth ( $\Delta H$ ) of 0.1 kOe at 35 GHz was obtained for 144  $\mu\text{m}$  thick BaM film from resonance absorption spectra. However, the linewidth of 0.1 kOe obtained is considerably larger than the best previous values reported for the thick BaM films grown on GGG substrates ( $\sim 60$  Oe at 59 GHz) [46]. This may be caused by the extrinsic strains and defects on the film surface as the film was grown at a higher temperature and also high growth rate of 72  $\mu\text{m}/\text{h}$  during the LPE process. Also, localized spin pinning and demagnetizing field effects by any outgrowths on the thicker films might have also caused the linewidth broadening.

Further reduction in FMR linewidth can be obtained by polishing and/or annealing the samples that enhance the crystal structure and reduce defects on the film and also any strains at the film substrate interface.

## 4.0. Magnetic and microwave properties of M-type Sm-doped SrFe<sub>12</sub>O<sub>19</sub> single crystals

### 4.1. Introduction

Strontium ferrite (SrFe<sub>12</sub>O<sub>19</sub>; SrM) is an M-type hexaferrites and has a magnetoplumbite crystal structure with easy magnetocrystalline anisotropy along the *c*-axis of the hexagonal unit cell just like the barium ferrite [8-9]. This ferrimagnet however exhibits a higher saturation magnetization and coercivity because of its relatively high magnetocrystalline anisotropy field [9]. The large anisotropy field in these ferrites acts as a built-in magnetic field and permits the application of ferrimagnetic resonance (FMR) in millimeter-wave devices [4]. Sufficiently low values of FMR linewidth ( $\Delta H$ ) are required for practical millimeter-wave device applications of hexagonal ferrites that can only be achieved by single crystal samples [1-6, 52-53]. For corresponding polycrystalline samples, the linewidth is about two orders of magnitude higher, typically  $\Delta H \sim 2000$  Oe [54-55]. Thus, microwave devices such as resonance isolators, circulators, tunable filters and oscillators can be operated in the millimeter-wave frequency range with moderate external magnetic bias fields. On the other hand, substitution for Fe<sup>3+</sup> and Sr<sup>2+</sup> is an effective method for tailoring the magnetic properties of these ferrites [17-19].

Although hexagonal ferrites have been extensively investigated in the past decades, the search for new substitution elements, especially the rare earth elements, has been a field of intense research [56-59]. Rare earth elements are unique because of their characteristic structure of electronic shells; physical, mechanical and magnetic properties could be improved by doping these elements in the hexagonal crystal lattice of hexaferrites. In this chapter, we studied the growth of high-quality single crystals of Sm-doped SrM (Sm-SrM) and the magnetic and

microwave properties with respect to the doping concentrations of Sm in the hexaferrite is discussed.

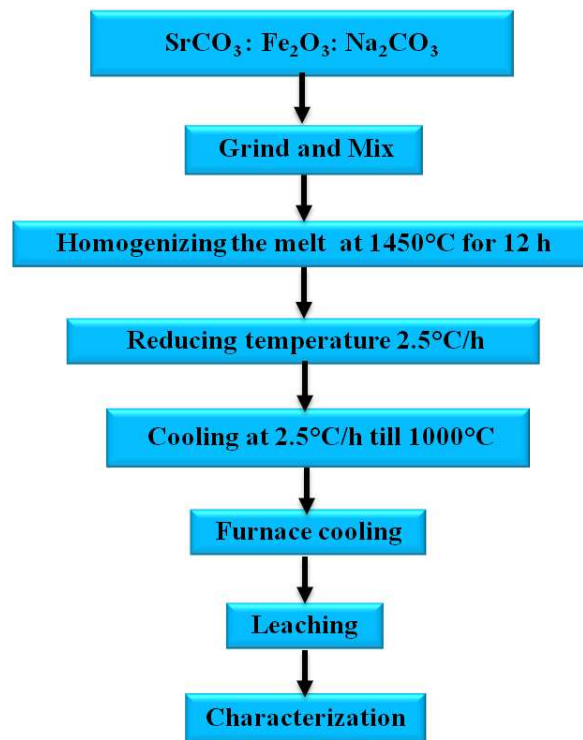


Figure 4.1 Experimental flowchart to grow Sm-SrM type single crystals.

#### 4.2. Experimental

Single crystals of Sm-doped SrFe<sub>12</sub>O<sub>19</sub> are grown in a platinum crucible using a high-temperature furnace. The primary reagents consist of SrCO<sub>3</sub>, Fe<sub>2</sub>O<sub>3</sub>, Sm<sub>2</sub>O<sub>3</sub> and Na<sub>2</sub>CO<sub>3</sub> (Reagent Grade, Sigma-Aldrich) with the respective mol % according to the composition 0.263 Na<sub>2</sub>CO<sub>3</sub> + 0.11 SrCO<sub>3</sub> + 0.61 Fe<sub>2</sub>O<sub>3</sub> + (x) Sm<sub>2</sub>O<sub>3</sub> (x = 0.017, 0.0098 and 0.0079) are used to grow the single crystals. The reagents after weighing the right amounts were blended and ground together in a pestle for 1 hour, thoroughly. The finely blended powder is filled in a platinum crucible with approximately three-fourths of the volume. The platinum crucible is then placed in a top-lift enclosed furnace and fired at the temperature of 1450 °C for 12 hours to homogeneous

the melt. After completely homogenizing the melt for 12 hours, it is slowly cooled at the rate of 2.5 °C/h to 1000 °C, and then cooled more rapidly in the furnace to room temperature. The obtained crystals were gradually separated by leaching in hot dilute nitric acid from the platinum crucible. Figure 4.1 shows the process flow chart to grow the Sm-SrM single crystals. Physical and magnetic properties of the grown single crystals are characterized by X-ray diffractometer (XRD), vibrating sample magnetometer (VSM) with a maximum applied field of 10 kOe, and optical microscopy. The microwave properties were measured by using a ferromagnetic resonance (FMR) measurement system.



Figure 4.2 Optical micrograph of the Sm-SrM single crystals.

#### 4.3. Results and discussion

The crystals grown in this study exhibits the typical hexagonal ferrite growth habit with a plate-like geometry, and the largest crystal is 10 mm in length and 3-4 mm in thickness. Figure 4.2 shows the optical micrograph of the grown crystals. We found that the grown crystals from the same batch contain several tiny crystals, some of them are Sm-doped SrM crystals, and the others contained a two phase crystal composition of Sm<sub>2</sub>O<sub>3</sub> and Sm-doped SrM. The saturation magnetization of the single crystal was measured by using a vibrating sample magnetometer (VSM). The values of saturation magnetization (at 10 kOe) and coercivity ( $H_c$ ) in the easy axis

direction are 69.8emu/g and 1.7 Oe, respectively as shown in Figure. 4.3. The low coercivity value indicates the crystals are free from impurities and voids.

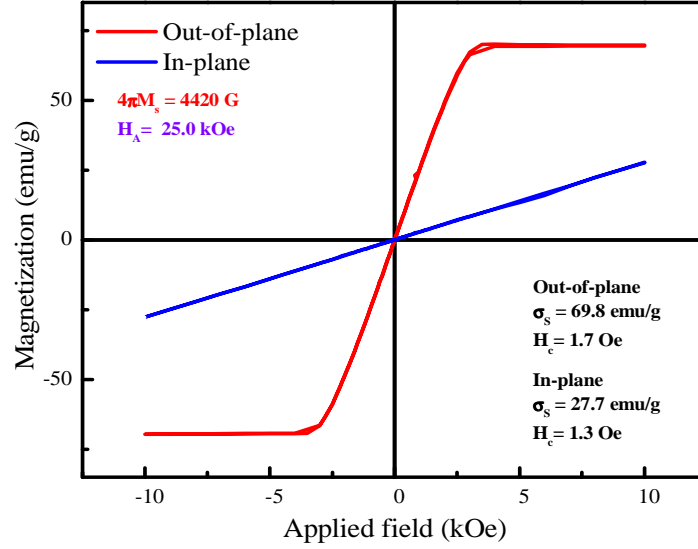


Figure 4.3 Magnetic hysteresis loop of Sm-SrM single crystal, when external magnetic field is out-of- plane (solid line) and in-plane (dashed line) to the crystal plane.

The uniaxial anisotropy field for the Sm-SrM crystal is verified theoretically by comparing the data from the VSM measurement. With  $H_{app}$  in the plane of the crystal, the magnetization is linear in  $H_{app}$  and the saturation was not achieved at the maximum available field of 10 kOe. Extrapolation of the out-of-plane and in-plane measurements from VSM data yields a saturation field of  $H_{sat(hard)} = 25.0$  kOe. In order to calculate the uniaxial anisotropy field ( $H_A$ ) with the demagnetizing factor in the in-plane direction, we used the following equation given by the saturation field [50]:

$$H_{sat(hard)} = H_A + 4\pi N_d M_s \quad (4.1)$$

For  $H_{app}$  along the crystal normal, to the easy direction, the magnetization is linear in  $H_{app}$  below saturation which occurs at  $H_{sat(easy)} = 4.0$  kOe. The saturation magnetic moment from the

hysteresis loop in Figure 4.3 is 69.8 emu/g. Assuming a density of 5.10 g/cm<sup>3</sup> for SrM, the saturation magnetization is obtained to be 4473 G. The demagnetizing factor  $N_n$  in the easy plane direction of the crystal is given by:

$$N_n = \frac{H_{sat(easy)}}{4\pi M_s} = \frac{4000}{4473} = 0.89 \quad (4.2)$$

estimated demagnetization in the film plane of crystal,  $N_d = (1 - N_n) / 2$ , and  $4\pi M_s = 4473$  G yield 24.75 kOe of anisotropy field ( $H_A$ ), which is close to the value obtained by extrapolation of the easy and the hard direction from the VSM measurements. Figure 4.4 shows the specific magnetization of the Sm-SrM single crystal along various measured directions against the  $c$ -axis of the crystal and a fairly large uniaxial anisotropy can be estimated for the crystal.

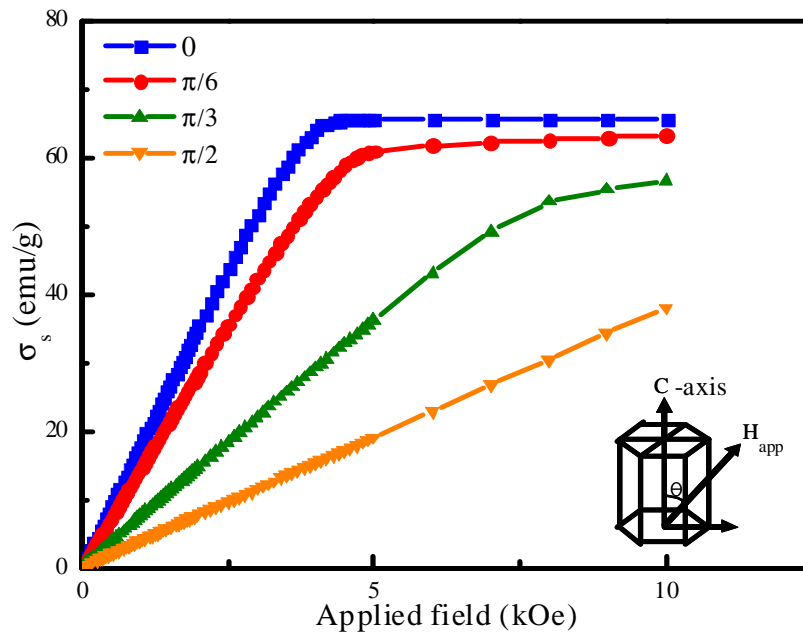


Figure 4.4 Magnetic hysteresis loop of Sm-SrM single crystal a function of the magnetic field applied at various angles with respect to the  $c$ -axis of the crystal.

<b>SrCO<sub>3</sub>:Fe<sub>2</sub>O<sub>3</sub>:Sm<sub>2</sub>O<sub>3</sub>: Na<sub>2</sub>CO<sub>3</sub> (mol%)</b>	<b><math>\sigma_{s\perp}</math> (emu/g)</b>	<b>H<sub>⊥</sub> (Oe)</b>	<b><math>\sigma_{s//}</math> (emu/g)</b>	<b>H<sub>c//</sub> (Oe)</b>	<b>H<sub>A</sub> (kOe)</b>
<b>11.53 : 61.0 : 0.79 : 26.30</b>	<b>65.5</b>	<b>2.7</b>	<b>38.02</b>	<b>9.72</b>	<b>19.5</b>
<b>11.53 : 61.0 : 0.98 : 26.30</b>	<b>63.7</b>	<b>4.2</b>	<b>40.0</b>	<b>7.61</b>	<b>23.0</b>
<b>11.53 : 61.0 : 1.17 : 26.30</b>	<b>69.8</b>	<b>1.7</b>	<b>27.7</b>	<b>1.3</b>	<b>25.0</b>

Table 4.1 Magnetic properties of Sm-SrM single crystal with various compositions.

A remarkable feature in the Sm-doped Sr-ferrite single crystal is the control of uniaxial anisotropy with the dopant concentration of the Sm ions. It was observed that as the percentage of Sm content in the composition of SrM increases from 0.79 mol % to 1.17 mol %, the uniaxial anisotropy field increased from 19.5 to 25 kOe, respectively. These details of the composition and the corresponding magnetic properties are summarized in the Table 4.1. An increase in the anisotropy can be attributed to the spin-orbit interaction between the different sites in the SrM crystal. Due to the large ion size difference between the Sm<sup>3+</sup> (0.97 Å) and Fe<sup>3+</sup> (0.64 Å), it is very unlikely that the rare-earth element Sm would substitute the Fe<sup>3+</sup> sites. The only real possibility is the substitution of Sr<sup>2+</sup> (1.12Å) by the Sm<sup>3+</sup>. As the ion size of the Sm is smaller than that of Sr<sup>2+</sup>, the Fe<sup>3+</sup> would be closer in the O-Fe-O lattice and a stronger interaction is anticipated, which would result in a change in the magnetic anisotropy of the Sm-doped SrM crystals. With increase in Sm concentration, the Sr ions are fully substituted by the Sm<sup>3+</sup>, suggesting a change in charge balance by gaining one electron for Fe<sup>3+</sup> on the 2a crystallographic sites, in which the strong Fe<sup>2+</sup> ion anisotropy attributes to increase in magnetocrystalline anisotropy [60-62].

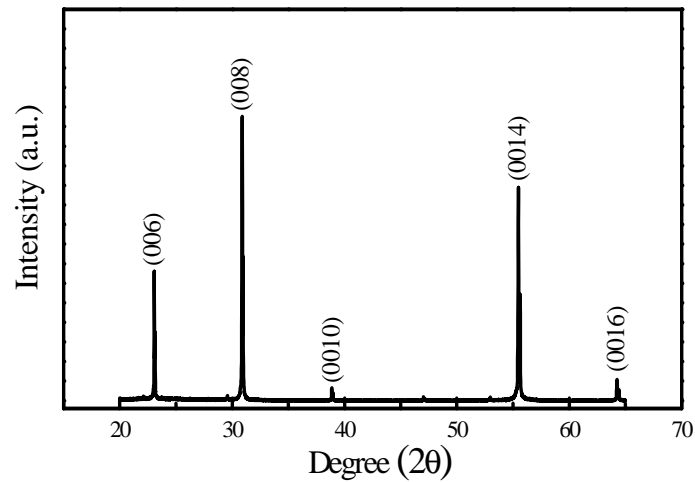


Figure 4.5 X-ray diffraction pattern of a Sm-SrM single crystal showing the (00*l*) planes of the crystal.

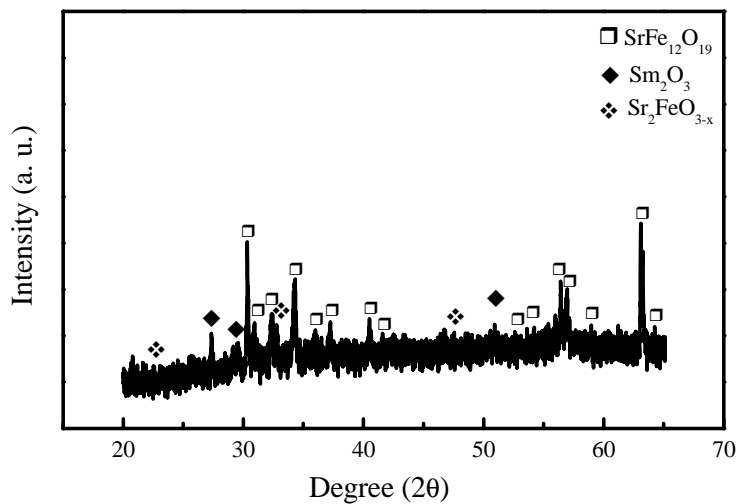


Figure 4.6 X-ray diffraction pattern of the powdered bulk crystals of Sm-SrM single crystal.

The crystal structure was confirmed by an X-ray diffractometer. The crystal reflects all the major planes of (006), (008), (0010), (0014) and (0016), which confirm the *c*-axis orientation of the crystal as shown in Figure 4.5. To further confirm the crystal structure, several bulk crystals are powdered, and the XRD measurement was performed. Figure 4.6 shows the XRD

pattern of the powdered single crystals. It was observed from the powdered pattern that there are some traces of strontium iron oxides ( $\text{SrFeO}_{3-x}$ ), and some phase of non-ferromagnetic samarium oxide ( $\text{Sm}_2\text{O}_3$ ) that coexist within the SrM. This kind of co-existing phases in the rare earth oxide dopants in hexaferrites was earlier reported by other researchers [63]. The existence of the nonmagnetic phase helps to understand the decrease in the saturation magnetization of the crystals doped with  $\text{Sm}^{3+}$  ions when compared to the bulk SrM crystal. Figure 4.7 shows room temperature Mössbauer spectra of the powdered single crystal sample. The spectra were contributed by the magnetic hyperfine field from Fe in five distinct crystallographic sites in the hexaferrite structure. All five sites, which are 12k, 4f<sub>IV</sub>, 4f<sub>VI</sub>, 2a, and 2b, are identified, but there are two unknown central peaks which might be due to the secondary phase such as  $\text{SrFeO}_{3-x}$  or the existence of a small amount of  $\text{Sm}_2\text{O}_3$  in the powder sample of the Sm-SrM crystals.

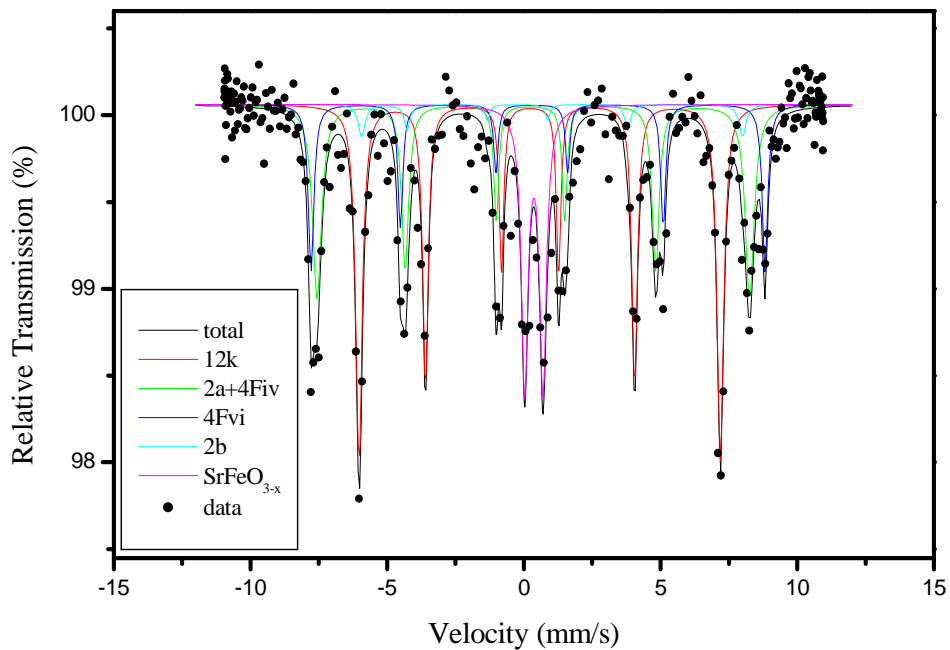


Figure 4.7 Mössbauer spectra of the powdered Sm-SrM single crystals.

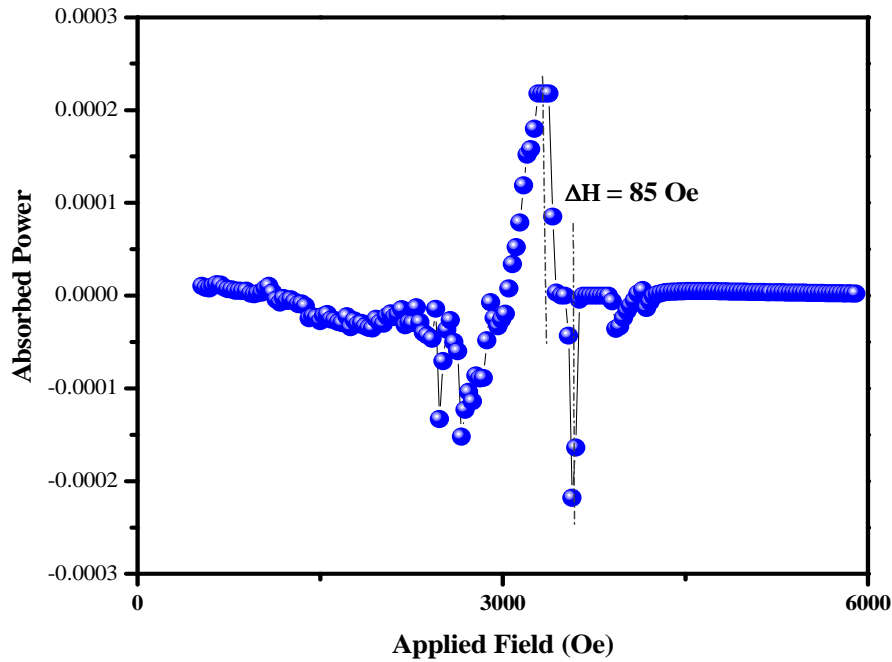


Figure 4.8 Ferrimagnetic resonance spectra of a thin single crystal of Sm-SrM with a linewidth of 85 Oe at 53 GHz.

Finally, ferrimagnetic resonance measurements (FMR) were performed at room temperature on a thin polished sample of Sm-SrM single crystal in the frequency range of 50-60 GHz. An FMR linewidth ( $\Delta H$ ) of 85 Oe was obtained at 53 GHz as shown in Figure 4.8. The linewidth is reasonable for the optimally prepared sample taking into the account the surface roughness and porosity in the sample. The linewidth can be further improved by grinding the samples to a sphere or round disk shape. The large uniaxial anisotropy fields present in these ferrites can be used to provide ferrimagnetic self-resonant frequencies above 40 GHz.

## 5.0. Ferrimagnetic $\text{Sr}_{(2-x)}\text{Ba}_x\text{Zn}_2\text{Fe}_{12}\text{O}_{22}$ ( $x = 0.5$ ) (Zn-Y) single crystal with planar anisotropy

### 5.1. Introduction

Among all the hexaferrites, Y-type hexaferrite ( $\text{Ba}_2\text{Zn}_2\text{Fe}_{12}\text{O}_{22}$ ; Zn-Y) is unique due to its in-plane (planar) magnetocrystalline anisotropy ( $H_A$ ) which has magnetization bounded to the basal plane of the crystal structure [8-9]. This unique planar nature of the Y-type hexaferrite satisfies the requirement for next generation ferrite phase shifters, since planar circuits are easy to be fabricated and integrated with semiconductor devices [20-21]. Moreover, substitution for  $\text{Fe}^{3+}$  and  $\text{Ba}^{2+}$  in Y-type hexaferrites is an effective method for tailoring the magnetic and physical properties of these ferrites and has been reported by several researchers [22-28]. Recently, single crystals of  $\text{Ba}_2\text{Mg}_2\text{Fe}_{12}\text{O}_{22}$  (Mg-Y) and  $\text{Sr}_{1.5}\text{Ba}_{0.5}\text{Zn}_2\text{Fe}_{12}\text{O}_{22}$  (SrBa-Y) showed a strong response to electric polarization and magnetization at room temperature which opens a potential for room temperature magnetoelectric (ME) devices and also magnetically controlled electro-optical devices [26-27].

Chun et al. showed that a small amount of Al substitution into SrBa-Y hexaferrite remarkably decrease the critical magnetic field ( $B$ ) for switching electric polarization ( $P$ ) from 1 T down to 1 mT, and the ME susceptibility is greatly enhanced to reach a giant value of  $2.0 \times 10^4$  ps/m at an optimum  $x = 0.08$  compared to  $4.3 \times 10^1$  ps/m for  $x = 0$  [27]. In SrBa-Y hexaferrite, the strontium cation with an ionic radius of 0.127 nm can be easily substituted for  $\text{Ba}^{2+}$  with an ionic radius of 0.143 nm. Moreover, it is highly anticipated that as the dopant concentration of  $\text{Sr}^{2+}$  increases, the hexagonal crystal lattice undergoes a greater distortion due to different size of ion by modifying the superexchange interaction between the iron ions. Although Zn-Y

hexaferrites have been widely explored for their magnetic and microwave properties, Sr-rich crystals of SrBa-Y hexaferrite have not been investigated in detail in this regard. The aim of this chapter is to study and understand the magnetic and microwave properties of strontium doped Zn-Y single crystals and to compare them with the un-doped Zn-Y single crystal.

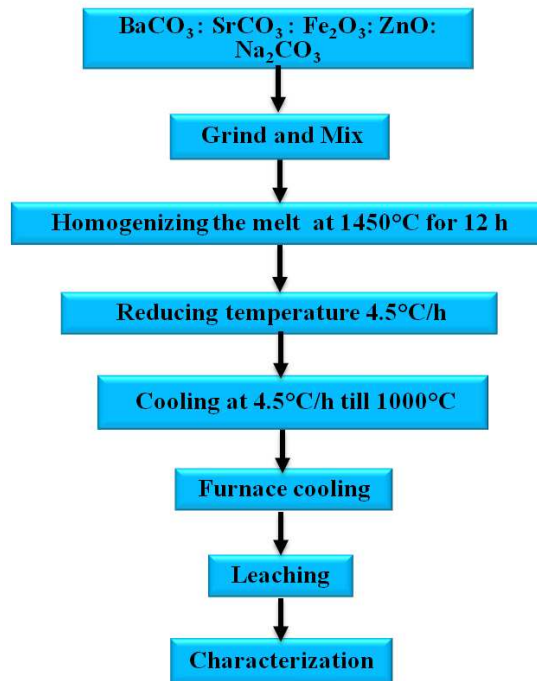


Figure 5.1 Experimental flowchart to grow SrBa-Y type single crystals.

## 5.2. Experimental

Single crystals of  $\text{Ba}_2\text{Zn}_2\text{Fe}_{12}\text{O}_{22}$  and  $\text{Sr}_{(2-x)}\text{Ba}_x\text{Zn}_2\text{Fe}_{12}\text{O}_{22}$  ( $x = 0.5$ ) were grown in a platinum crucible using the high temperature growing process reported in [64-65]. A typical mixture to grow SrBa-Y consisted of 4.92 mol %  $\text{BaCO}_3$ , 14.76 mol %  $\text{SrCO}_3$ , 53.61 mol %  $\text{Fe}_2\text{O}_3$ , 19.69 mol %  $\text{ZnO}$  and 7.01 mol %  $\text{Na}_2\text{CO}_3$ . As shown in Figure 5.1, the reagents were blended and ground together thoroughly in a pestle for 1 hour. The finely blended powder filled a platinum crucible, approximately three-fourth of the crucible volume. The crucible was then placed in a top-lift enclosed furnace and fired at the temperature of 1450 °C for 12 hours, to

homogenize the melt. After the melt was completely homogenized, it was slowly cooled at 4.5°C/h to 1000 °C, and then followed by a rapid cooling in the furnace to room temperature. The obtained crystals were separated, by leaching in hot dilute nitric acid, from the platinum crucibles. The morphology of the grown single crystals was examined with an optical microscope. The composition and the crystalline phase were identified by X-ray diffractometer (XRD). The magnetic properties were measured by a vibrating sample magnetometer (VSM) with a maximum applied field of 10 kOe and microwave properties were characterized using a broadband ferromagnetic resonance (FMR) measurement.



Figure 5.2 Optical micrograph of several bulk SrBa-Y single crystals showing the hexagonal growth habit morphology.

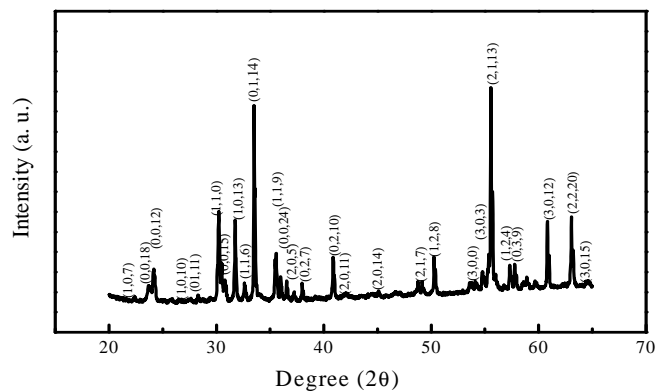


Figure 5.3 X-ray powder diffraction pattern of Sr-BaY single crystal.

### 5.3. Results and discussion

Figure 5.2 shows the optical micrograph of several bulk single crystals of SrBa-Y showing a typical hexagonal ferrite growth habit with a plate-like geometry on the crystal surfaces which are 4 to 6 mm in diameter and 2 to 3 mm in thickness. The crystal structure was confirmed by an X-ray diffractometer. Several bulk crystals were powdered for the XRD measurement. The crystal reflects all the major planes, which confirm the in-plane orientation of the crystal as shown in Figure 5.3.

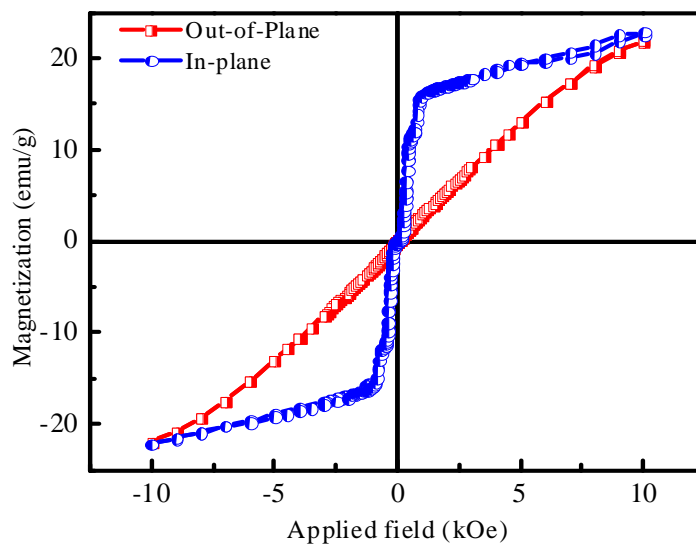


Figure 5.4 Magnetic hysteresis loop of SrBa-Y single crystal

Figure 5.4 shows the magnetic hysteresis loop measured in the out-of-plane and in-plane directions of the SrBa-Y hexaferrite single crystal having a magnetization of 22.5 emu/g at 10 kOe and a coercivity of 3.5 Oe in the easy axis in-plane direction. It is also evident from the VSM data that the easy axis of the crystal is in-plane, and the hard axis is out-of-plane to the crystal surface unlike M-type hexaferrites that have the easy axis out-of-plane and the hard axis in-plane. To better understand the static magnetic properties of the SrBa-Y hexaferrite, magnetic properties of pure Zn-Y hexaferrite were also investigated. Figure 5.5 (a) shows the low-field

magnetization curve of the Zn-Y single crystal, which has a saturation magnetization of 43.0 emu/g (at 10 kOe) and a coercivity of 0.2 Oe in the easy axis in-plane direction, which are close to the bulk values reported in the literature. Low-field magnetization curve of SrBa-Y presented in Figure 5.5 (b) shows novel magnetization behaviors in the easy direction. No net magnetization was observed up to the applied field ( $H_{app}$ ) of 400 Oe for SrBa-Y, unlike the Zn-Y crystal. However, it shows the ferrimagnetic behavior similar to the Zn-Y crystal at higher  $H_{app}$  of 1 kOe. This phenomenon can be understood by the superexchange interactions in the crystal lattice by different sizes of ions. The ionic size of Sr = 1.27 Å is smaller than that of Ba = 1.43 Å, and as a result, a local lattice deformation around Sr ions occurs which leads to a stronger superexchange interaction between Fe–O–Fe due to a change in the bond angles between them [66-67].

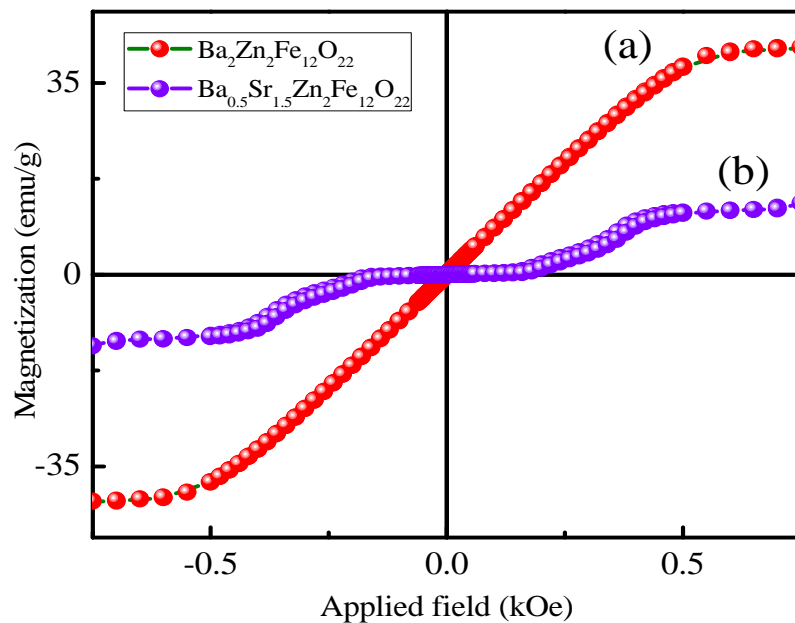


Figure 5.5 Magnetic hysteresis loop of (a) Zn-Y and (b) SrBa-Y single crystal at low applied field.

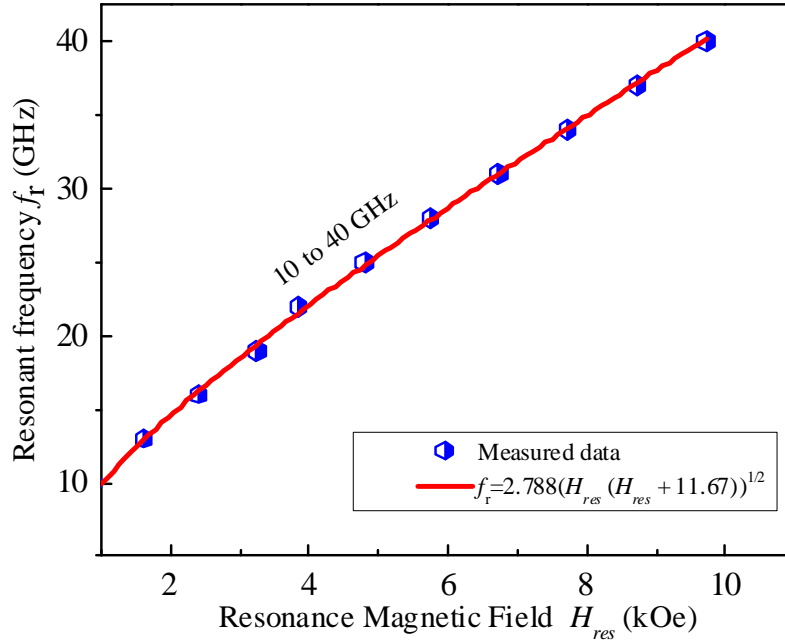


Figure 5.6 Plot of frequency vs FMR resonance field for a single crystal SrBa-Y sample.

With regard to microwave properties, FMR measurements were performed on a finely polished SrBa-Y single crystal in the form of a slab using a shorted waveguide configuration and a differential absorption detection scheme over a frequency range of 10 to 40 GHz. For ferrites with planar anisotropy, ferrimagnetic resonance occurs at a frequency which depends on both the resonant magnetic field  $H_{res}$  and the uniaxial anisotropy field  $H_A$ . The resonance condition is given by the relation [28].

$$\left(\frac{f_r}{\gamma}\right) = \sqrt{H_{res}(H_{res} + (4\pi M_s + H_A))} \quad (5.1)$$

However, for Y-type hexagonal ferrites with their high uniaxial anisotropy the saturation magnetization ( $4\pi M_s$ ) is considered to be the effective saturation magnetization ( $4\pi M_{eff}$ ) which is ( $4\pi M_s + H_A$ ). Therefore, Eq. (5.1) can be rewritten as:

$$\left(\frac{f_r}{\gamma}\right) = \sqrt{H_{res}(H_{res} + (4\pi M_{eff}))} \quad (5.2)$$

where,  $f_r$  is the resonance frequency in GHz and  $\gamma' = 2.8$  GHz/kOe. From the VSM measurement in Figure 5.4, the  $4\pi M_s$  value was calculated to be 1530 G. The magnetic anisotropy field ( $H_A$ ) was found by plotting the FMR frequency as a function of  $H_{res}$ , which was applied perpendicular to the slab plane. By fitting Eq. (5.2), we observed  $4\pi M_{eff} = 11.672$  kOe. From this, the value of  $H_A$  was estimated to be 10 kOe as shown in Figure 5.6 which is in good agreement with the magnetization curve as shown in Figure 5.4.

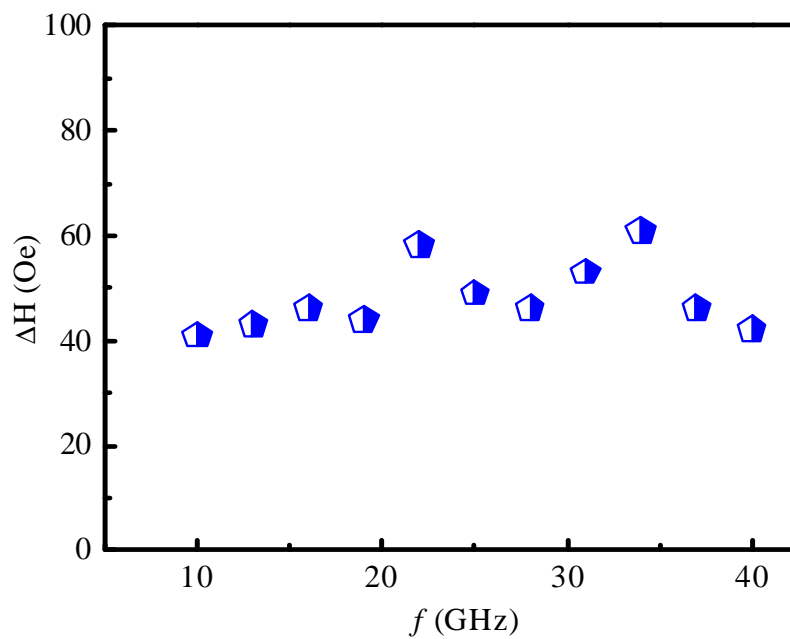


Figure 5.7 Plot of FMR linewidth vs. frequency for a single crystal SrBa-Y sample.

Finally, Figure 5.7 shows the FMR linewidth as a function of frequency from 10 to 40 GHz. The average  $\Delta H$  is about 48 Oe and remains constant from 10 to 40 GHz. The FMR linewidth of a ferromagnetic material depends on two factors. The first one is the intrinsic relaxation of system magnetization also called as the Gilbert damping where a linear response to the frequency is observed for  $\Delta H$ . The second parameter corresponds to the extrinsic two-magnon scattering processes in which magnon scattering was caused by one, or a combination, of the following mechanisms: spatial inhomogeneities in the local magnetic anisotropy fields, or

inhomogeneities in the local exchange interaction magnetic inhomogeneities of the ferromagnetic material. In our case, due to the relatively high dopant concentration of  $\text{Sr}^{2+}$  ions in the Zn-Y crystal and also due to the superexchange interactions between the different size of ions in the crystal lattice we observed a very small increase in linewidth with increasing the microwave frequency, which suggests that extrinsic relaxation mechanisms are dominant. This type of nonlinear response behavior is reported earlier for M-type barium ferrite single crystals and films [37, 68]. Figure 5.8 shows a  $\Delta H$  of 41 Oe at 10 GHz for the SrBa-Y single crystal. This low linewidth of 41 Oe has not yet been reported in the literature for the  $\text{Sr}_{1.5}\text{Ba}_{0.5}\text{Zn}_2\text{Fe}_{12}\text{O}_{22}$  ferrites. Moreover, the relatively constant  $\Delta H$  values obtained over a wide frequency range from 10 GHz to 40 GHz are important for practical device applications.

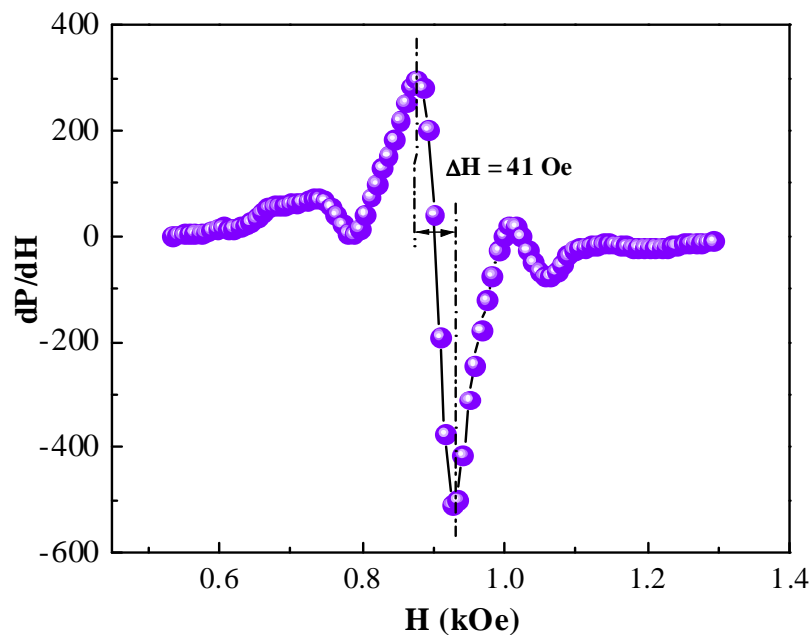


Figure 5.8 Ferrimagnetic resonance linewidth of a SrBa-Y single crystal sample showing the linewidth of 41 Oe at 10 GHz.

## **6.0. Magnetic and microwave properties of ferrimagnetic Zr-substituted $\text{Ba}_2\text{Zn}_2\text{Fe}_{12}\text{O}_{22}$ (Zn-Y) single crystal**

### 6.1. Introduction

As seen in the earlier chapter, one of the great advantages of the hexaferrites is to tailor their magnetic properties with the addition of different cation dopant elements. Not many studies have been done on reporting the effect of increase in saturation magnetization for Y-type hexaferrite single crystals. For example, saturation magnetization ( $\sigma_s$ ) of polycrystalline Zn-Y hexaferrite was increased by substituting  $\text{Co}^{2+}$  and  $\text{Cu}^{2+}$  for  $\text{Zn}^{2+}$  from 30 emu/g to 36 emu/g [69] but large magnetic loss was observed.  $\text{Sr}^{2+}$  substitution for  $\text{Ba}^{2+}$  in polycrystalline  $\text{Ba}_{2-x}\text{Sr}_x\text{Zn}_2\text{Fe}_{12}\text{O}_{22}$  hexaferrite showed a decrease in  $\sigma_s$  and increase in permittivity with Sr content from  $x = 1.0$  to  $1.5$  [70]. Savage et al. showed that a small quantity of  $\text{Mn}^{2+}$  substitution in single crystalline Zn-Y decreased the ferrimagnetic resonance (FMR) linewidth to 3.8 Oe at 9 GHz [71].

Although polycrystalline Zn-Y hexaferrite has been widely studied for their magnetic and microwave properties, their high microwave losses are still an issue to address. On the other hand, high quality Zn-Y single crystals showed promising results, operating at  $K_U$  band frequencies by reducing insertion losses and increasing bandwidth [4, 72]. However, microwave devices, such as phase shifters, employing Zn-Y single crystal hexaferrites need at least 2 kOe of the applied field to bias the ferrite [20-21]. It is still a rather large applied field and requires bulky and costly permanent magnets with high current drives to perform the operation. Therefore, there is a potential need to improve the magnetic and microwave properties of Y-type

hexaferrites for next generation of microwave devices. In this chapter, we report low loss and high anisotropy single crystal Zn-Y hexaferrite by substituting Zr ions into the Zn-Y type hexaferrite. It was found that substitution of Zr in the Zn-Y hexaferrite single crystal increases the  $\sigma_s$  from 44 emu/g to 52 emu/g and the  $H_A$  from 10 kOe to 13 kOe. This improvement in magnetic properties plays an important role for microwave devices that can operate with a low external bias field.

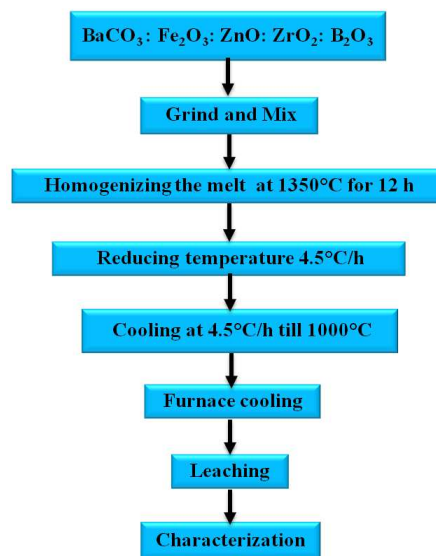


Figure 6.1 Experimental flowchart to grow Zr-Zn-Y type single crystals



Figure 6.2 Optical micrograph of bulk single crystals of Zr-Zn-Y ( $\text{Ba}_2\text{Zn}_2\text{Zr}_x\text{Fe}_{12-x}\text{O}_{22}$ )

## 6.2. Experimental

As shown in the process flowchart in Figure 6.1, single crystals of Zr-substituted Zn-Y ( $\text{Zr-Zn-Y}$ ;  $\text{Ba}_2\text{Zn}_2\text{Zr}_x\text{Fe}_{12-x}\text{O}_{22}$ ) were grown in a platinum crucible using a high temperature

furnace. The primary reagents of BaCO<sub>3</sub>, ZnO, Fe<sub>2</sub>O<sub>3</sub>, ZrO<sub>2</sub> and B<sub>2</sub>O<sub>3</sub> with the respective mol % according to the composition 0.563BaCO<sub>3</sub> + (0.25-x)Fe<sub>2</sub>O<sub>3</sub> + 0.08ZnO + 0.263B<sub>2</sub>O<sub>3</sub> + (x) ZrO<sub>2</sub> (x = 0.00, 0.05 and 0.08) were chosen. The reagents were blended and ground together thoroughly in a pestle for 1 h. The finely blended powder filled a platinum crucible, approximately three-fourth of the crucible volume. The crucible was then placed in a top-lift enclosed furnace and fired at the temperature of 1350 °C for 12 h, to homogenize the melt. After the melt was completely homogenized, it was slowly cooled at the rate of 4.5°C/h to 1000 °C, and then followed by rapid cooling in the furnace to room temperature. The crystals were separated, by leaching in hot dilute nitric acid, from the platinum crucible. The morphology of the grown single crystals was examined with an optical microscope. The composition and the crystalline phase were identified by X-ray diffractometer (XRD). The magnetic properties were measured by a vibrating sample magnetometer (VSM) with a maximum applied field of 10 kOe and microwave properties were characterized using a broadband ferrimagnetic resonance (FMR) measurement.

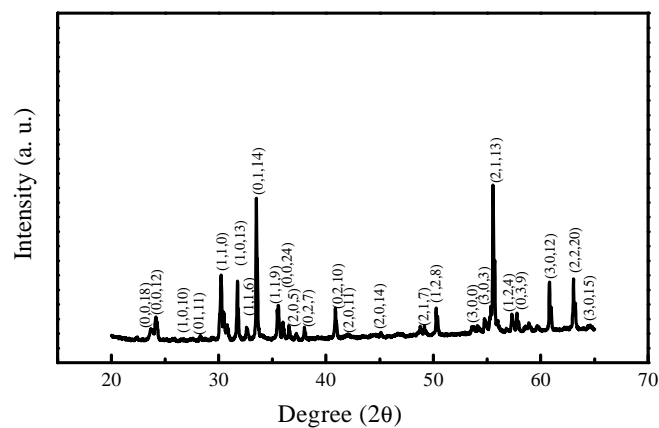


Figure 6.3 X-ray powder diffraction pattern reflecting all the major planes, which confirm Zn-Y composition.

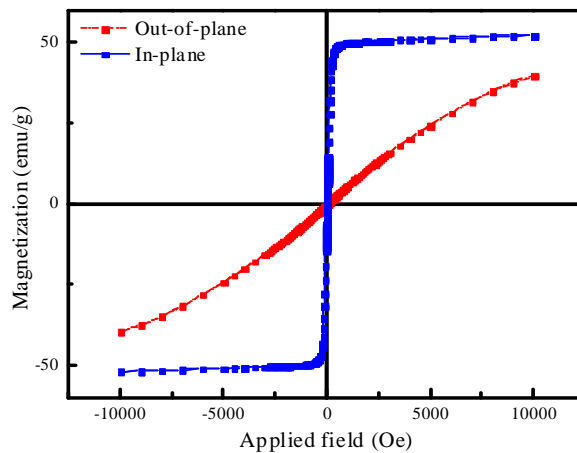


Figure 6.4 Magnetic hysteresis loops of  $\text{Ba}_2\text{Zn}_2\text{Zr}_x\text{Fe}_{12-x}\text{O}_{22}$  single crystal, when external magnetic field is applied in-plane (easy axis) and out-of-plane (hard axis).

### 6.3. Results and discussion

Figure 6.2 shows the optical micrograph of several bulk single crystals of Zr-Zn-Y ( $\text{Ba}_2\text{Zn}_2\text{Zr}_x\text{Fe}_{12-x}\text{O}_{22}$ ;  $x = 0.05$ ) hexaferrite. The crystals show a typical hexagonal ferrite growth habit with a plate-like geometry on the crystal and are 4 to 6 mm in diameter and 3 to 4 mm in thickness. Several bulk crystals were powdered for the XRD measurement. All X-ray peaks are indexed to the major planes of the Zn-Y hexaferrite composition as shown in Figure 6.3. The magnetic hysteresis loops were measured using a VSM in the out-of-plane and in-plane directions of the Zr-Zn-Y hexaferrite single crystal. Figure 6.4 shows the magnetic hysteresis loop of Zr-Zn-Y hexaferrite single crystal with the  $\text{ZrO}_2$  dopant amount of  $x = 0.05$ . The crystal has a  $c$ -plane magnetization of 52 emu/g at 10 kOe and a coercivity of 0.8 Oe in the easy axis in-plane direction. It is noted that uniaxial anisotropy ( $H_A$ ) and the  $\sigma_s$  of Zr-Zn-Y are controllable with a dopant concentration of the Zr ions. The  $H_A$  field increased from 10 to 13 kOe when the concentration of Zr is increased to  $x = 0.05$  and then decreased to 12.5 kOe at  $x = 0.08$ , while the

$\sigma_s$  shows the same trend. The composition and the corresponding magnetic properties are summarized in Table 6.1. Increase in  $H_A$  and  $\sigma_s$  with the concentration of Zr can be attributed to the superexchange interactions between the  $\text{Fe}^{3+}$  cations at different sites in the Zn-Y crystal lattice.

<b>BaCO<sub>3</sub>:ZnO: Fe<sub>2</sub>O<sub>3</sub>: B<sub>2</sub>O<sub>3</sub> : ZrO<sub>2</sub></b>	<b><math>\sigma_s //</math> (in-plane)</b>	<b><math>H_c //</math> ( in-plane)</b>	<b><math>\sigma_s \perp</math> (Out-of-plane)</b>	<b><math>H_c \perp</math> (Out-of-plane)</b>	<b><math>H_A</math></b>
<b>[mol %]</b>	<b>[emu/g]</b>	<b>[Oe]</b>	<b>[emu/g]</b>	<b>[Oe]</b>	<b>[kOe]</b>
<b>50.13: 7.12: 22.26 : 20.48: 0.0</b>	<b>44.0</b>	<b>0.4</b>	<b>31.0</b>	<b>3.7</b>	<b>10.0</b>
<b>50.13: 7.12: 17.80 : 20.48: 4.45</b>	<b>52.0</b>	<b>0.8</b>	<b>42.0</b>	<b>10.0</b>	<b>13.0</b>
<b>50.13: 7.12: 15.13 : 20.48: 7.12</b>	<b>38.0</b>	<b>0.8</b>	<b>27.0</b>	<b>6.8</b>	<b>12.0</b>

Table 6.1 Compositions and magnetic properties of  $\text{Ba}_2\text{Zn}_2\text{Zr}_x\text{Fe}_{12-x}\text{O}_{22}$  single crystal.

In a Zn-Y hexaferrite crystal, the magnetic moments of iron ions are arranged perpendicular to the hexagonal  $c$ -axis, but with opposite spin directions in the individual sublattices. Albanese et al. determined the various metallic lattice sites together with their coordination and spin orientations [73]. The crystal has six sublattices which are  $6c_{IV}$  (spin-down),  $3a_{VI}$  (spin-up),  $18h_{VI}$  (spin-up),  $6c_{VI}$  (spin-down),  $6c^*_{VI}$  (spin-down), and  $3b_{VI}$  (spin-up). The resulting magnetization  $M$  at a temperature  $T$  of Zn-Y per formula unit (f.u.) can be approximated by a simple summation according to the formula:  $M(T) = -6\sigma_{c_{IV}}(T) + 3\sigma_{a_{VI}}(T) + 18\sigma_{h_{VI}}(T) - 6\sigma_{c_{VI}}(T) - 6\sigma_{c^*_{VI}}(T) + 3\sigma_{b_{VI}}(T)$ , where  $\sigma$  stands for the magnetic moment of a  $\text{Fe}^{3+}$  ion. Assuming a magnetic moment of  $5 \mu_B$  per  $\text{Fe}^{3+}$  ion at 0 K ( $\mu_B$  is the Bohr magneton), the net magnetization of  $30 \mu_B$  per f.u. is obtained for pure Zn-Y. Accordingly, an increase of the net magnetization is expected if the  $\text{Fe}^{3+}$  ions in the spin down sublattices ( $6c_{IV}$ ,  $6c_{VI}$  and  $6c^*_{VI}$ ) are

replaced by non-magnetic ions.  $O^{2-}$  (1.4 Å) and  $Ba^{2+}$  (1.35 Å) ion take a close-packed layer structure along the  $c$ -axis of the Zn-Y crystal. Corresponding ionic radii are given in parentheses. The interlayers of tetrahedral and octahedral sites are occupied by  $Zn^{2+}$  (0.74 Å) and/or  $Fe^{3+}$  (0.64 Å) ions [73]. Substitution of non-magnetic  $Zr^{4+}$  (0.79 Å) will replace and substitute the  $Fe^{3+}$  sites in the  $6c^*_{VI}$  tetrahedral sites thus strengthening the  $Fe^{3+}$ -O- $Fe^{3+}$  superexchange interaction resulting in an increase of the net magnetization [74]. With an increase in the Zr ion concentration from  $x = 0.05$  to  $x = 0.08$ , the  $Fe^{3+}$  ions in the tetrahedral sites are fully substituted by the Zr ions, which causes a magnetic dilution by changing of the  $Fe^{3+}$  (high spin) valence state to  $Fe^{2+}$  (low spin) state on the tetrahedral sites. This weakens the  $Fe^{3+}$ -O- $Fe^{3+}$  superexchange interaction by the  $Fe^{2+}$  ions. In addition, a change in the anisotropy constant is anticipated with increase in the Zr ion concentration in Zr-Zn-Y hexaferrite. In hexagonal crystals, the crystalline anisotropy is originated from the dipole-dipole interaction, and for Y-type hexaferrites, the spin configuration is in the basal plane that is perpendicular to the  $c$ -axis. A complete calculation of the dipole sums has been made by Casimir et al. and is given by the equation (4.5) [75]:

$$(K_1)_{dip} = -(0.044 \mu_t^2 + 0.0006 \mu_t \mu_o + 0.240 \mu_o^2) \cdot 10^6 \text{ erg/cm}^3 \quad (6.1)$$

where  $\mu_t$  and  $\mu_o$  are the average magnetic moments expressed in Bohr magnetons of the tetrahedral and octahedral ions, respectively. From Eq.6.1, it was shown that the  $K_1$  values range from -5 to -7 x  $10^6$  erg/cm<sup>3</sup> for various Y-type hexaferrites at T = 0 K. For the Zr-Zn-Y material, Mössbauer spectra analysis is needed to reveal the cation site occupancy to determine the  $K_1$  values, which is currently under investigation. Figure 6.5 shows the specific magnetization of the Zr-Zn-Y single crystal along various measured directions against the  $c$ -axis of the crystal. The planar nature of the hexaferrite is clearly seen, where the easy axis of the crystal is in-plane and the hard axis is out-of-plane to the crystal surface.

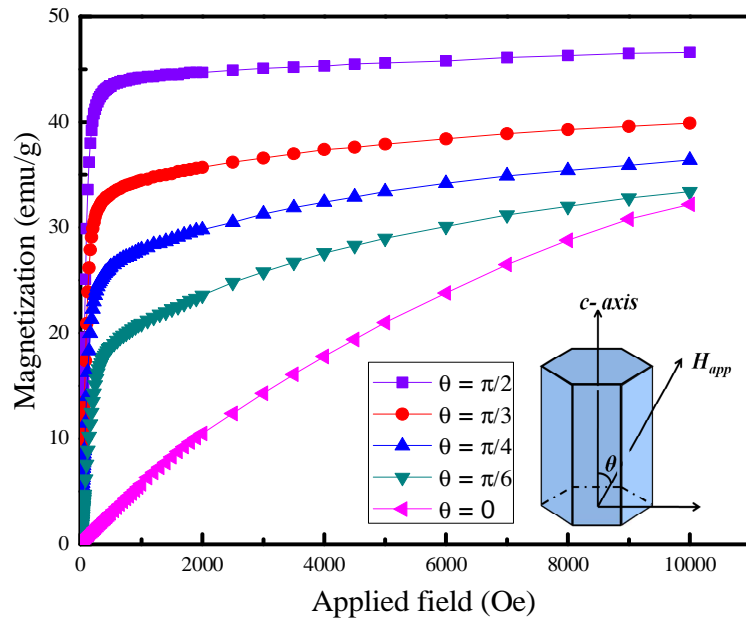


Figure 6.5 Angular dependence of magnetization for  $\text{Ba}_2\text{Zn}_2\text{Zr}_x\text{Fe}_{12-x}\text{O}_{22}$  single crystal, when external magnetic field is applied in-plane (easy axis) and out-of-plane (hard axis).

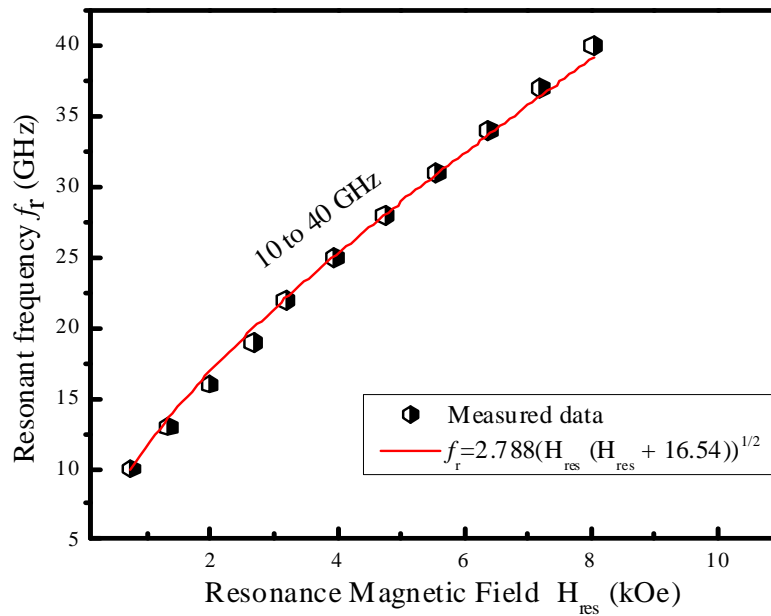


Figure 6.6 Plot of frequency vs FMR resonance field for a single crystal Zr-Zn-Y.

With regard to microwave properties, FMR measurements were performed on a finely polished Zr-Zn-Y single crystal in the form of a slab using a shorted waveguide configuration and a differential absorption detection scheme over a frequency range of 9 to 40 GHz. For ferrites with planar anisotropy, ferrimagnetic resonance occurs at a frequency which depends on both the resonant magnetic field  $H_{res}$  and the  $H_A$ . The resonance condition is given by the relation [28]:

$$\left( \frac{f_r}{\gamma'} \right) = \sqrt{H_{res}(H_{res} + (4\pi M_s + H_A))} \quad (6.2)$$

however, the saturation magnetization ( $4\pi M_s$ ) is considered to be the effective saturation magnetization ( $4\pi M_{eff}$ ) for Y-type hexagonal ferrites due to their high uniaxial anisotropy, which is ( $4\pi M_s + H_A$ ). Therefore, Eq. (6.2) is rewritten as

$$\left( \frac{f_r}{\gamma'} \right) = \sqrt{H_{res}(H_{res} + (4\pi M_{eff}))} \quad (6.3)$$

where  $f_r$  is the resonance frequency in GHz and  $\gamma' = 2.8$  GHz/kOe. From the VSM measurement in Figure 6.4, the  $4\pi M_s$  value was calculated to be 3544 G. The  $H_A$  was found by plotting the FMR frequency as a function of  $H_{res}$ , which was applied perpendicular to the slab plane. By fitting Eq. (6.3), we obtained  $4\pi M_{eff} = 16.54$  kOe. From this, the value of  $H_A$  was estimated to be 13 kOe as shown in Figure. 6.6, which is in good agreement with the magnetization curve as shown in Figure 6.4. An FMR linewidth ( $\Delta H$ ) of 18 Oe at 9 GHz was obtained for a Zr-Zn-Y ( $\text{Ba}_2\text{Zn}_2\text{Zr}_x\text{Fe}_{12-x}\text{O}_{22}$ )  $x = 0.08$  single crystal as shown in Figure 6.7. One reason for a low  $\Delta H$  is the substitution of  $\text{Zr}^{4+}$  in the Zn-Y crystal. It was reported that the tetravalent ion is able to form stable bonds with  $\text{Fe}^{2+}$  ions [76]. As the Zr concentration increases,  $\text{Fe}^{2+}$  content decreases, therefore reducing magnetic loss in ferrite. The values of  $H_A$  and  $\Delta H$  are comparable to those of Savage et al. [71] and Obol et al. [77] who used Mn to reduce the  $\text{Fe}^{2+}$  ion concentration. In the

former case, the  $4\pi M_s$  dropped from 2800 G to 2350 G, and in the latter case, fairly high  $\Delta H$  of 140 Oe at 9.56 GHz were obtained. The combination of low  $\Delta H$  with a high  $H_A$  in Zr-Zn-Y ( $\text{Ba}_2\text{Zn}_2\text{Zr}_x\text{Fe}_{12-x}\text{O}_{22}$ ;  $x = 0.08$ ) hexaferrite plays an important role for microwave devices that can operate with a low external biasing field.

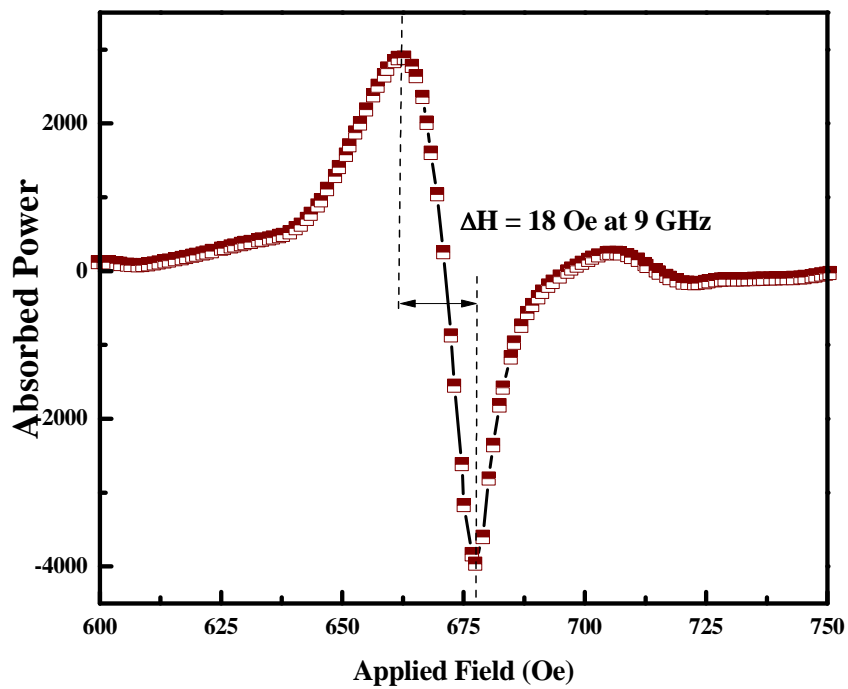


Figure 6.7 Ferrimagnetic resonance linewidth of a Zr-Zn-Y single crystal sample showing the linewidth of 18 Oe at 9 GHz.

## 7.0. MFM studies of magnetic domain patterns in BaM single crystals

### 7.1. Introduction

Ferromagnetic or ferrimagnetic materials get their magnetic properties not only because their atoms carry a magnetic moment but also because the material is made up of small regions known as magnetic domains [8]. In each domain, all of the atomic dipoles are coupled together in a preferential direction. This alignment develops as the material develops its crystalline structure during solidification from the molten state. Hexagonal ferrites with their complicated crystal structures and high crystalline anisotropy exhibit unique magnetic domain patterns when compared to cubic ferrites [8-9]. The first experimental observation of the magnetic domain patterns in hexagonal ferrites was done by Kooy and Enz by using the Faraday technique [78]. Bates et al. showed that domain pattern in single crystal of  $\text{PbFe}_{12}\text{O}_{19}$  consisted of  $180^\circ$  domains with complex pattern of undulatory walls and closed loops on the basal planes [79]. The relationship between the domain spacing and crystal thickness has been studied for a number of crystals of magnetoplumbite by Kaczér et al. [80]. The results showed that the domain width ( $\delta$ ) and thickness of the crystal ( $T$ ) were related by  $\delta \propto T^{1/2}$  for crystals with  $T < 10 \mu\text{m}$  and  $\delta \propto T^{2/3}$  for  $T > 10 \mu\text{m}$ . Kojima et al. studied domain patterns on BaM and strontium ferrite by the Faraday technique and determined the thickness dependence of the domain width on sample ranging from 2 to 25  $\mu\text{m}$  [81]. Later, these results were also verified by Gotō for  $\text{BaFe}_{12}\text{O}_{19}$  and  $\text{SrFe}_{12}\text{O}_{19}$  thin crystal platelets from 2 to 25  $\mu\text{m}$  [82]. The first experimental observations on the influence of external defects such as nonmagnetic inclusions and grain boundaries on the domain structures in BaM crystals was observed by Wells et al. [83]. The effect of cationic dopant

elements of Co and Ti in BaM thin single crystal platelets of 0.8  $\mu\text{m}$  to 300  $\mu\text{m}$  thickness was studied by Gemperle et al. [84]. It was found that with increasing Co concentration the thickness for surface wall undulation decreases.

Although the techniques of Faraday and Kerr effect methods have been extensively used to investigate magnetic domain structures in BaM single crystals, they have a limited resolution of about 300 nm. Moreover, intensity variations due to the sample's topography and angle of rotation of the plane of polarization have been a disadvantage. On the other hand, development of new imaging technique, such as magnetic force microscopy (MFM), has shown very promising results in the investigation of magnetic domain structure in thin films [85-86]. Based on the interaction between the magnetic tip and the sample, the stray field can be imaged with quite high resolution. Several studies have been reported on magnetic domain observation in thin polycrystalline BaM films using the MFM technique [87-89]. However, study of magnetic domain patterns in bulk single crystals of BaM using MFM has not yet been reported. In this chapter, we report the magnetic domain patterns in bulk BaM single crystals and investigate the switching properties of domains using the MFM technique. Also, the thickness dependence of domain width in the BaM crystals was studied.

## 7.2. Experimental

BaM single crystals were grown from a primary mixture of iron oxide ( $\text{Fe}_2\text{O}_3$ ), barium carbonate ( $\text{BaCO}_3$ ), and sodium carbonate ( $\text{Na}_2\text{CO}_3$ ). The mole ratios of the mixtures were chosen to be 63.17 mol %, 10.53 mol %, and 26.3 mol %, respectively [48]. The reagents were blended and ground together thoroughly in a pestle for 1 hour. The finely blended powder is

filled in a platinum crucible with approximately three-fourths of the volume. The platinum crucible is then placed in a furnace and fired at the temperature of 1350 °C for 12 hours to homogenize the melt. After completely homogenizing the melt for 12 hours, it is slowly cooled at the rate of 2.5 °C/h to 1000 °C, and then cooled more rapidly in the furnace to room temperature. The obtained crystals were separated from the platinum crucible by leaching in hot dilute nitric acid. A complete process flow chart of the process is shown in Figure 7.1. Physical and magnetic properties of the grown BaM single crystals were characterized by X-ray diffractometer (XRD), vibrating sample magnetometer (VSM) with a maximum applied field of 10 kOe, and scanning electron microscopy (SEM). Large single crystal BaM sample were chosen for the MFM measurement to observe the domain structures. The samples were thoroughly polished by fine micro-polish slurry by using the metallographic technique to make the surfaces smoother and free from any sharp edges or irregularities to observe the magnetic domain patterns.

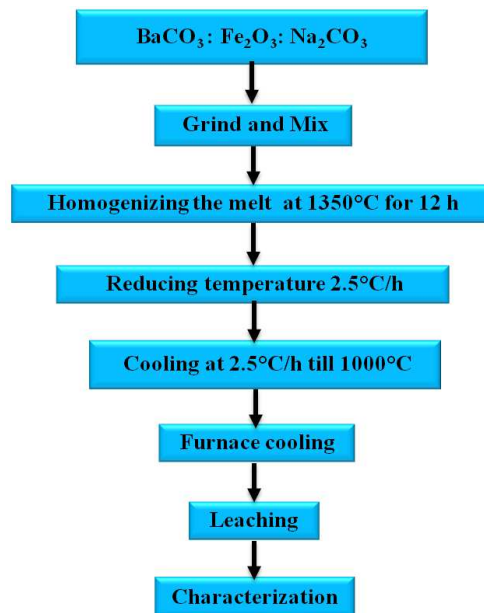


Figure 7.1 Experimental flowchart to grow BaM single crystals

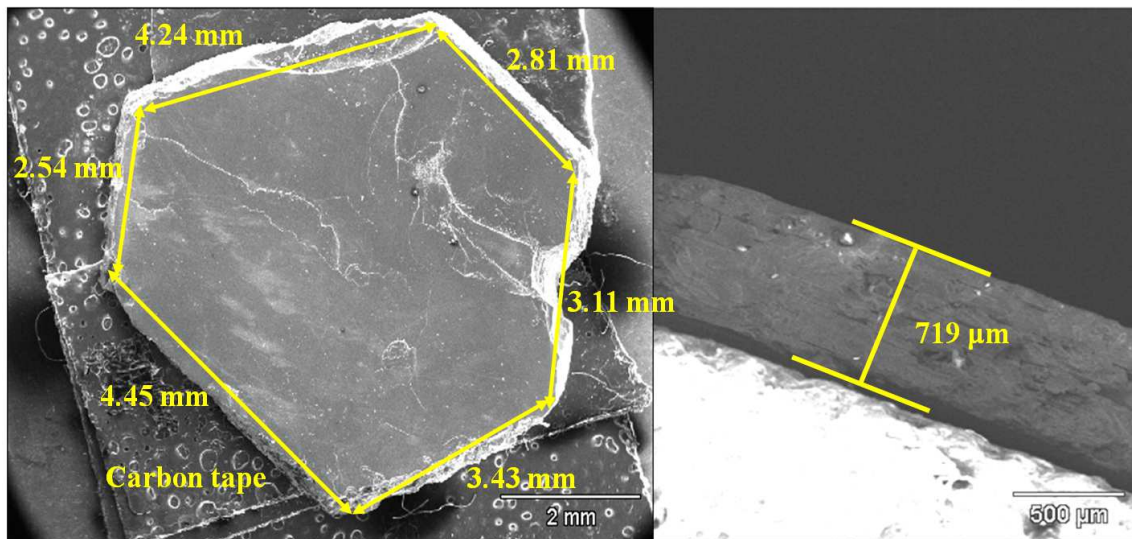


Figure 7.2 SEM image of a bulk BaM single crystal showing the top view and the cross-sectional view.

### 7.3. Results and discussion

The BaM crystals obtained exhibited the typical hexagonal ferrite growth habit with a plate-like geometry normal to the crystal plane. Figure 7.2 shows an SEM image of the top view and the cross-sectional view of a typical BaM crystal obtained. The largest crystal was up to 0.5 g in weight and 3-4 mm in diameter. The crystal structure was confirmed by an X-ray diffractometer. The crystal reflects all the major planes of (006), (008), (0010), (0012), (0014) and (0016), which confirm the  $c$ -axis orientation of the crystal as shown in Figure 7.3. The static magnetic properties of the single crystal were measured by a vibrating sample magnetometer (VSM). The values of saturation magnetization ( $\sigma_s$ ) and coercivity ( $H_c$ ) at 10 kOe in the easy axis direction are 69.8 emu/g and 0.8 Oe, respectively, as shown in Figure 7.4. The low coercivity value indicates that the crystals are free from impurities and voids.

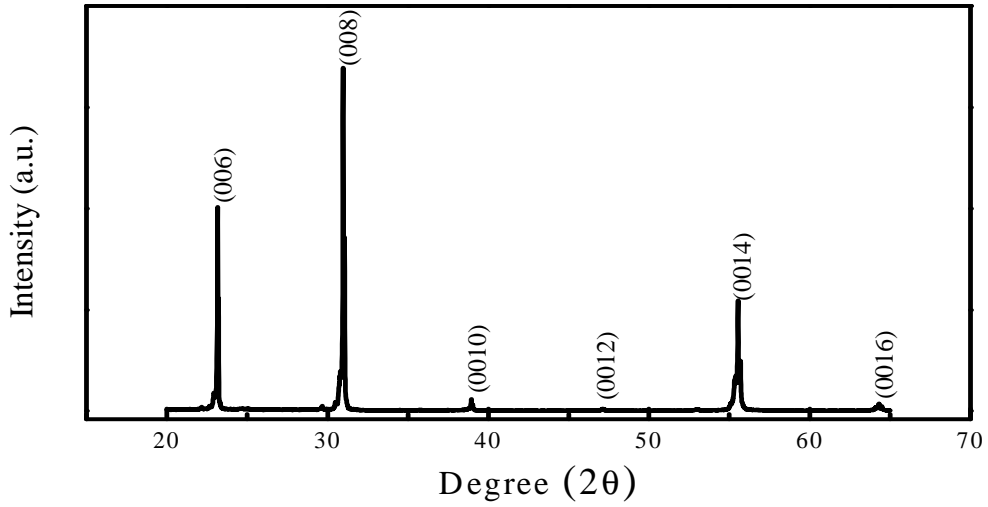


Figure 7.3 X-ray diffraction pattern of a BaM single crystal showing the (00*l*) planes of the crystal.

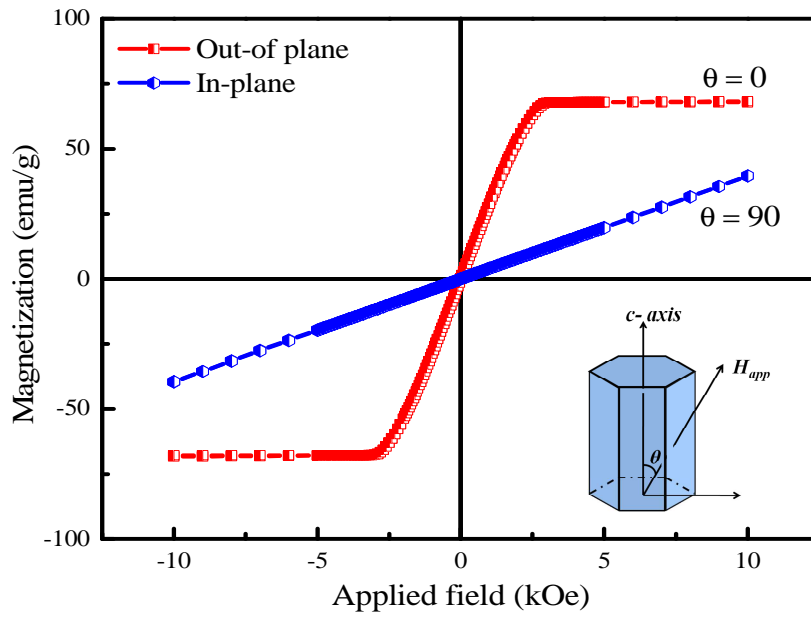


Figure 7.4 Magnetic hysteresis loops of BaM single crystal, when external magnetic field is applied out-of-plane and in-plane of the crystal.

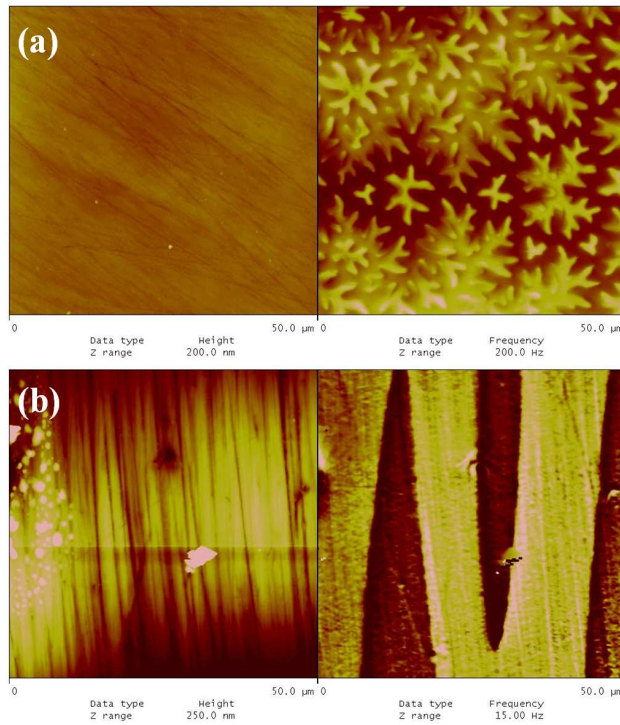


Figure 7.5 AFM and MFM images of a BaM single crystal on the (a) basal plane and (b) prism plane.

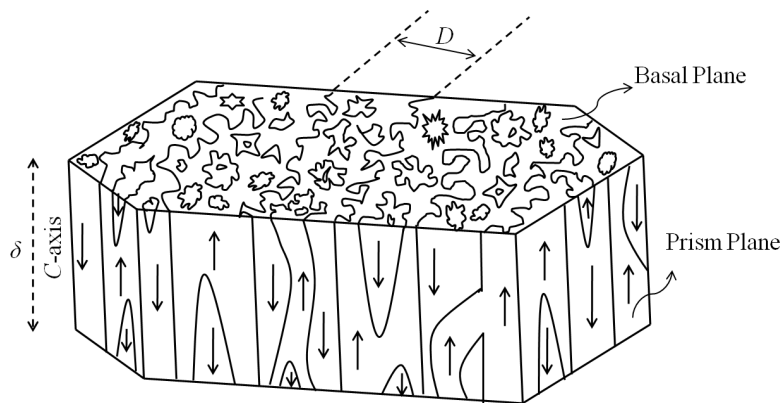


Figure 7.6 Artist's sketch showing the domain patterns on the basal plane and the prism plane of a bulk BaM single crystal.

To observe the magnetic domains of the BaM crystal, several crystals are collected and leached for a day with mild heating in dilute nitric acid to remove any surface impurities and

contaminants. The as-cleaned crystals were then polished by using fine micro-polish slurry by regular metallographic technique to decrease their size and make the surfaces smoother and shiny. Figure 7.5 (a) and 7.5 (b) show atomic force microscopy (AFM) and MFM images of a BaM single crystal on the basal planes and the prism planes, respectively. Well-isolated, highly contrasting flower-like patterns are observed on the basal plane and sharp spike-like domains are observed on the prism plane. The observed domains showed regions of bright contrasts at the center of the flower patterns and darker contrast along the edges. This bright (dark) MFM contrast indicates an upward (downward) vertical field gradient originating from the positive (negative) magnetic charges along the easy axis of the BaM crystal. It was reported earlier by other researchers that materials with a uniaxial anisotropy, such as BaM, show patterns on the surface from simple to complicated, leading to the appearance of corrugation and spike domains, and also more complicated “flower” domains [83-84]. This complicated configuration of domain patterns is shown as an explanatory sketch in Figure 7.6.

Thickness ( $T$ ) dependence of the domain width ( $\delta$ ) for various crystals was observed from the MFM scans by measuring domain width. Figure 7.7 shows the domain patterns of BaM single crystals with different thicknesses from 800  $\mu\text{m}$  to 100  $\mu\text{m}$ . It was found that the domain width decreased from 32  $\mu\text{m}$  to 9  $\mu\text{m}$ . In order to investigate and compare our results to published data, we plotted  $\log \delta$  against  $\log T$  as shown in Figure 7.8. The relationship between  $\delta$  and  $T$  is expressed as  $\delta = a T^b$ , where  $a$  and  $b$  are constants [82]. The constants  $a = 0.523$  and  $b = 0.611$  were determined from line intercept and slope of Figure 7.8, respectively. These values are very close to the reported results [80]. In addition, for uniaxial anisotropic crystals, the width of the domain is expressed as [90]

$$\delta = \sqrt{\frac{\sigma T}{0.85 M_s^2}} \quad (1)$$

where  $M_s$  is the saturation magnetization and  $\sigma$  is the domain wall energy given as

$$\sigma = 4\sqrt{AK_u} \quad (2)$$

the exchange constant  $A$  for BaM is  $0.5 \times 10^{-6}$  erg/cm [91] and the anisotropy constant  $K_u$  is  $3.2 \times 10^6$  erg/cm<sup>3</sup> [92]. The value of  $M_s$  is obtained from the VSM loop in Figure 7.4 to be 369 emu/cm<sup>3</sup>. For 100  $\mu$ m thick crystal (Figure 7.7 (c)), the  $\delta$  from the MFM image was measured to be 9  $\mu$ m. On the other hand, by using the equations (1) and (2), we calculated  $\delta$  to be 6.6  $\mu$ m, which is close to the experimental value observed from the MFM images.

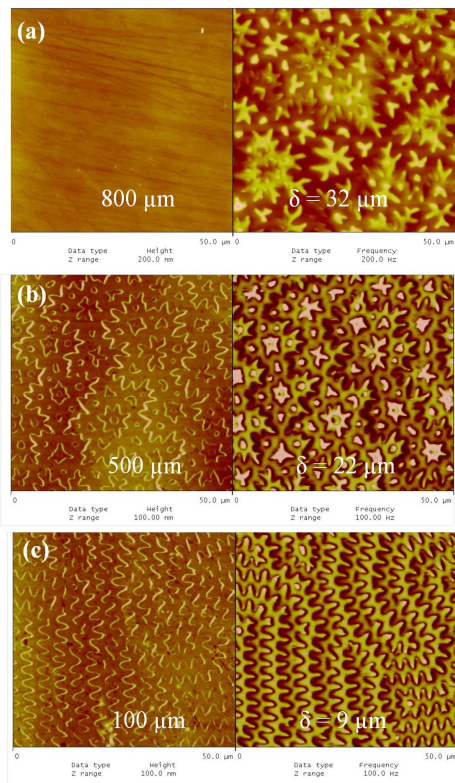


Figure 7.7 AFM and MFM images showing the thickness dependence on domain width of (a) 800  $\mu$ m, (b) 500  $\mu$ m, and (c) 100  $\mu$ m thick BaM crystal.

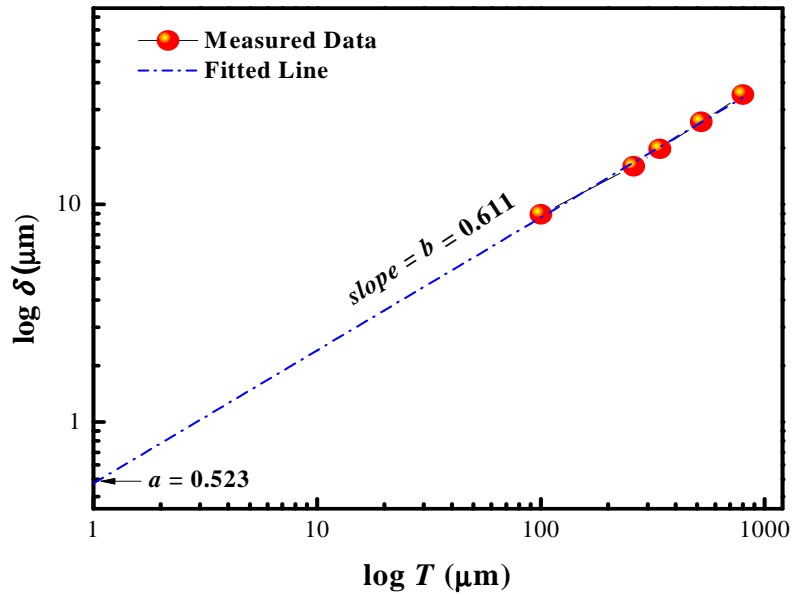


Figure 7.8 Measured relationship between the domain width ( $\delta$ ) and thickness ( $T$ ) of BaM crystals.

Finally, in order to study the dynamic switching process of individual domain, an identifying area on the crystal surface was chosen as a reference point such that it can be easily located during the process of successive application of an external applied field to the sample. After measuring the static magnetic domain pattern in the as-polished state, consecutive increase of 2 kOe field was applied by an electromagnet. The applied field direction was kept fixed along the easy direction ( $c$ -axis) of the BaM crystal sample as shown in Figure 7.4. After each step has been completed, the MFM images were taken at the reference point. Figure 7.9 shows the MFM images of change in domain configuration on the basal plane with an applied field. Figure 7.9 (a) shows the MFM image of the as-grown crystal in the demagnetized state with a few white flower-like dendritic patterns surrounded by dark regions throughout the basal plane of the crystal surface. The dark regions correspond to the domains having a magnetization component parallel to the crystal easy axis, and the white regions corresponding to the domains with

magnetization component anti-parallel to the  $c$ - axis of the crystal. With the increase in applied field, the darker domains grow at the expense of the white domains. Therefore, the magnetic domains, which remain canted from the easy axis, start to disappear and transform by aligning towards the applied field direction with an increase towards the saturation magnetization. Figure 7.9 (d) shows that, as the value of the applied field approaches the saturation value, only a small number of anti-parallel domains remain.

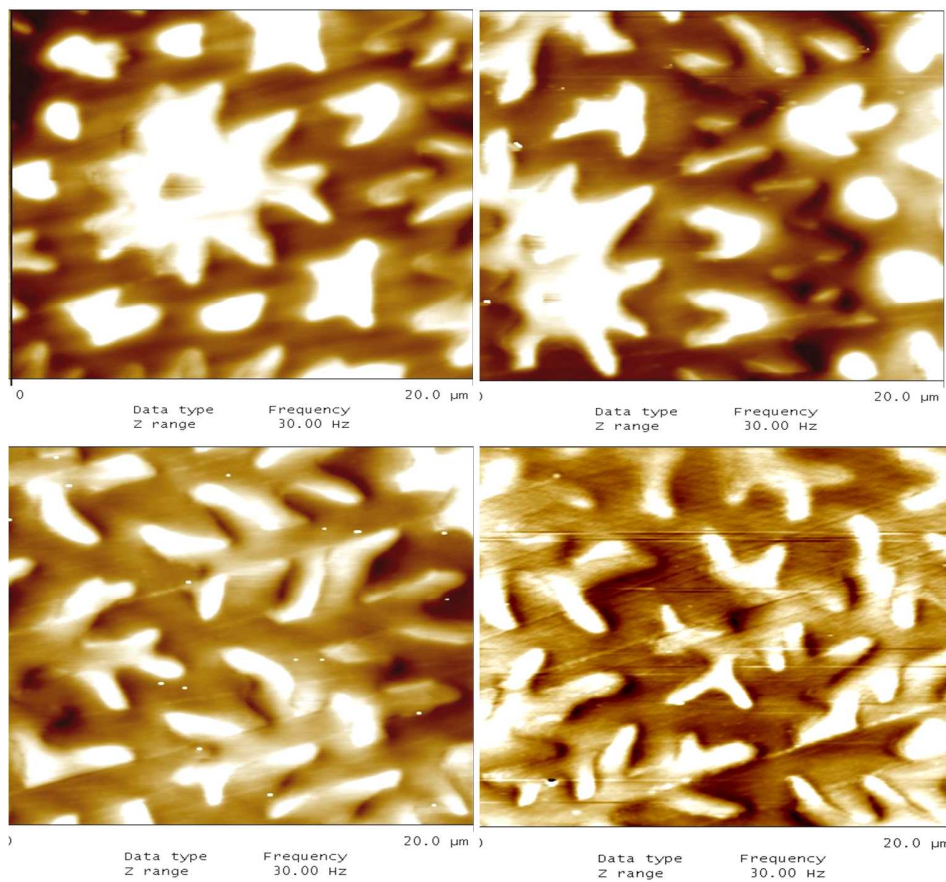


Figure 7.9 MFM images of BaM single crystal taken on the basal plane (a) as-grown, (b) after a 2 kOe field was applied, (c) after a 4 kOe field was applied, and (d) after a 6 kOe field was applied during the initial magnetization process.

## CONCLUSIONS

### **Part I. Spherical barium ferrite nanoparticles**

Spherical shaped barium ferrite (S-BaFe), were successfully synthesized by a unique adsorption diffusion process and a hydrothermal process. Precursory spherical magnetite (S-Mag) and cubic hematite nanoparticles were first synthesized and are coated by barium ions on the surface of the precursory particles which are later heat-treated at elevated temperature to convert to S-BaFe nanoparticles.

7-30 nm S-Mag nanoparticles were synthesized by a modified organic process where an iron oleate complex was first prepared by reacting iron chlorides and sodium oleate and later this complex is reacted in a high boiling point solvent to obtain the S-Mag nanoparticles. The S-Mag particles had a saturation magnetization ( $\sigma_s$ ) of 70 emu/g and exhibited superparamagnetic behavior as confirmed by the Mössbauer studies. Well dispersed 20-25 nm sized uniform hematite nanocubes were synthesized by the decomposition of an ironoleate complex under hydrothermal conditions, which was prepared from the reaction of iron chloride and sodium oleate. The process conditions were optimized to scale-up the process and to produce hematite nanocubes with uniform shape and narrow particle size distribution. The nanocubes had a saturation magnetization ( $\sigma_s$ ) and coercivity ( $H_c$ ) values of 0.47 emu/g and 77 Oe respectively.

24-30 nm sized S-BaFe were synthesized from nanosized S-Mag nanoparticles by the adsorption diffusion process. Room temperature Mössbauer spectra confirm no existence of superparamagnetic particles. Saturation magnetization and coercivity of the S-BaFe nanoparticles were found to be 41.4 emu/g and 4075 Oe, respectively. The thermal stability

factor for the S-BaFe particles was obtained to be  $K_u V/k_B T \approx 107$  from the time-dependent remanent coercivity measurements. S-BaFe particles synthesized from the uniform hematite nanocubes showed a saturation magnetization ( $\sigma_s$ ) of 45.4 emu/g with an intrinsic coercivity ( $H_C$ ) of 3015 Oe at a maximum applied field of 10 kOe. The particle sizes ranged from 20-22 nm.

In order to eliminate the several processing steps used by the adsorption-diffusion process, an alternative hydrothermal process was developed and optimized to synthesize S-BaFe nanoparticles. The worm-shaped particles were synthesized by hydrothermally reacting a mixture of  $\text{Ba}(\text{NO}_3)_2$  and  $\text{Fe}(\text{NO}_3)_3 \cdot 9(\text{H}_2\text{O})$  in an autoclave. 25-45 nm S-BaFe were obtained from the heat treatment of the worm-shaped particles. The saturation magnetization and coercivity of the heat treated S-BaFe nanoparticles were obtained to be 50.7 emu/g and 4311 Oe, respectively. Thermal stability measured on the particles showed a values  $K_u V/k_B T \approx 81$  from time-dependent remanent coercivity measurements. The table below summarizes the magnetic properties of S-BaFe nanoparticles achieved by the three different processes respectively.

Synthesis Process	Heat-treatment temperature	$\sigma_s$ (at 10 kOe) (emu/g)	$\sigma_r$ (emu/g)	$H_C$ (Oe)	Particle Size (nm)
S-MaG→S-BaFe	900°C-2h	41.4	24.3	4075	24-30
$\alpha$ -Fe <sub>2</sub> O <sub>3</sub> →S-BaFe	900°C-2h	45.4	26.4	3015	20-22
Hydrothermal	800°C-2h	50.7	30.2	4311	25-45

Table 8.1 Magnetic properties of S-BaFe nanoparticles achieved by the three different processes.

## Part II. Hexaferrite Single Crystals

Liquid phase epitaxy (LPE) technique was used to grow 144  $\mu\text{m}$  thick barium ferrite ( $\text{BaFe}_{12}\text{O}_{19}$ ; BaM) single crystalline films on (111)  $\text{Gd}_3\text{Ga}_5\text{O}_{12}$  (GGG) substrate. The growth rate of 72  $\mu\text{m}/\text{h}$  was achieved with a flux system of  $\text{Fe}_2\text{O}_3 - \text{BaCO}_3 - \text{Na}_2\text{CO}_3$ . The grown BaM films

show single crystalline (000 $l$ ) orientation that was confirmed by X-ray diffraction pattern and magnetic torque curves. The saturation magnetization ( $4\pi M_s$ ) and the anisotropy field ( $H_k$ ) were found to be 4.2 kG and 16.0 kOe, respectively. The ferrimagnetic resonance (FMR) linewidth ( $\Delta H$ ) at 35 GHz was measured to be 0.1 kOe.

High purity bulk single crystals of hexaferrites were grown and studied for their magnetic and microwave properties with respect to different cation dopant elements. M-type samarium doped strontium ferrite single crystals have been grown with a  $\text{SrCO}_3$  and  $\text{Na}_2\text{CO}_3$  flux system. The crystals exhibited the typical hexagonal ferrite growth habit with a plate-like geometry, and the largest crystals obtained are of 10 mm in length and 3-4 mm in thickness, respectively. It was observed that the saturation magnetization and anisotropy field are significantly affected by the doping concentration of Sm ions in the hexagonal crystal lattice of BaM. A saturation magnetization ( $\sigma_s$ ) of 69.8 emu/g and an anisotropy field ( $H_A$ ) of 25 kOe was achieved. Room temperature FMR measurements show 85 Oe of linewidth ( $\Delta H$ ) at 53 GHz.

Magnetic and microwave properties of planar Y-type  $\text{Sr}_{(2-x)}\text{Ba}_x\text{Zn}_2\text{Fe}_{12}\text{O}_{22}$  ( $x = 0.5$ ) single crystals were grown from the flux systems of  $\text{BaCO}_3$ ,  $\text{SrCO}_3$ , and  $\text{Na}_2\text{CO}_3$  by a high-temperature flux method. The anisotropy field ( $H_A$ ) and the in-plane magnetization ( $\sigma_s$ ) were measured to be 10 kOe and 22.5 emu/g, respectively. Ferrimagnetic resonance (FMR) measurements showed 41 Oe of linewidth ( $\Delta H$ ) at 10 GHz. Also, Zr substituted  $\text{Ba}_2\text{Zn}_2\text{Fe}_{12}\text{O}_{22}$  (Zn-Y) were grown from the flux systems of  $\text{BaCO}_3$  and  $\text{B}_2\text{O}_3$ . X-ray diffraction pattern confirmed that the crystal structure is an extended single crystalline array of Zn-Y composition with an in-plane easy axis crystallographic orientation. The obtained single crystals were characterized for magnetic and microwave properties. The anisotropy field ( $H_A$ ) and the in-plane magnetization ( $\sigma_s$ ) were

measured to be 13 kO and 52.0 emu/g, respectively. Ferrimagnetic resonance (FMR) measurements showed 18 Oe of linewidth ( $\Delta H$ ) at 9 GHz.

Finally, Magnetic domain patterns in bulk BaM single crystals on the basal (000 $l$ ) and the prism (1102) plane were studied by magnetic force microscopy (MFM). The surface domain patterns are in the form of flowers, stars, or saw type on the basal plane and long elongated spikes or stripe domains on the prism plane. The change in domain structure with an applied field ( $H_{app}$ ) and the thickness ( $T$ ) dependence on domain width ( $\delta$ ) were observed. The domain width decreased from 32  $\mu\text{m}$  to 9  $\mu\text{m}$  for the crystals of 800  $\mu\text{m}$  to 100  $\mu\text{m}$  thicknesses, respectively. The results obtained from domain images and the thickness dependence of domain wall width agree with the theoretical values.

## FUTURE WORK

### **Part I. Spherical Barium Ferrite Nanoparticles**

The magnetic tape industry is actively searching for a better performance magnetic media to meet future storage demands as today's tapes are fast approaching their thermal limit for recording capacity by reducing particle size. The produced S-BaFe particles although meet the required magnetic properties for a high-density particulate recording media the process needs to be further optimized to obtain scalable quantities. It was observed that increasing the amount of precursory particles quantity resulted in an increased amount of secondary phase formation such as  $\alpha$ -Fe<sub>2</sub>O<sub>3</sub> and spinel BaFe<sub>2</sub>O<sub>4</sub>. The results from those synthesis attempts were not promising enough, but a further fine tuning of the process needs to be evaluated. For example, changing the Ba/Fe/solvent concentrations with respect to DI water and ethanol, time for mixing and proper dispersing the particles needs to be studied and optimized.

The nature of the precursory particles also had a significant role in obtaining good S-BaFe particles. For example, it was very challenging to retain the spherical morphology of the synthesized S-BaFe particles by both the absorption diffusion and the hydrothermal process if the initial precursory particles had any organic surfactants (oleic acid, oleylamine) remained on the surface of the particles. The individual precursory particles stucked together during the drying stage of the process and later did not disperse well during the coating process which caused them to sinter together at high temperatures. Therefore, it is extremely important to use properly cleaned and dried precursory particles (preferably vacuum dried) with good dispersion mechanism during the coating process.

Future work should also involve in understanding the mechanism of phase and crystalline transformation of the precursor particles to the S-BaFe nanoparticles. The as-synthesized particles at various temperatures need to be studied for their thermochemical behavior and chemical bonding by thermal analysis and FTIR (Fourier-transform infrared (FTIR) spectrophotometer measurements. TEM images of the coated particles should be analyzed and studied for further understanding of the envisioned coating process.

Efforts to reduce the high sintering temperature and the prolonged holding times at that temperature need to be minimized. One way to realize this is if we can subject the as-coated precursory particles to microwave sintering instead of the conventional sintering methods. In microwave sintering, the heating rate is very rapid and the heat is generated internally within the particle instead of originating from the external source therefore instantaneous heat and shorter times for sintering to obtain the barium ferrite phase can be achieved.

## **Part II. Hexaferrite Single Crystals**

The results achieved from the thick films and the single crystals show significant improvement in magnetic and microwave properties. The next steps would be to get the ferrite films self-biased completely to avoid the use of permanent magnets to bias the microwave devices. Unfortunately, single crystal thick films and crystals have no remanence due to the demagnetization fields. One possible way to achieve this goal is by making a composite substrate of BaM which can consist of a single crystal hexaferrite slab in a matrix of polycrystalline hexaferrite.

## REFERENCES

### Part I. Spherical Barium Ferrite Nanoparticles

- [1] In Search of the Long-Term Archiving Solution -Tape Delivers Significant TCO Advantages over Disk, a white paper by The Clipper Group. December 23, 2010.
- [2] <http://www.oracle.com/us/products/servers-storage/storage/tape-storage/storagetek-tape-linecard-176440.pdf>
- [3] R. E. Fontana, Jr., S. R. Hetzler, and G. Decad, IEEE Trans. Magn., **48**, 1692 (2012). (<http://www.insic.org/news/A&S%20Roadmap.pdf>)
- [4] <http://public.dhe.ibm.com/common/ssi/ecm/en/tsd03127usen/TSD03127USEN.PDF>
- [5] <http://www.oracle.com/us/products/servers-storage/storage/tape-storage/storagetek-t10000-t2-cartridge-296699.pdf>
- [6] <http://www.zurich.ibm.com/news/10/storage.html>
- [7] DDS Specs Drive DAT Reliability, Computer Technology Review, **13**, 30 (1993).
- [8] H. N. Bertram, Theory of Magnetic Recording, Cambridge University Press, New York (1994).
- [9] J. D. Livingston, J. Appl. Phys., **52**, 2544 (1981).
- [10] G. Bertotti, Hysteresis in Magnetism, Academic Press, San Diego, (1998).
- [11] R. L. Comstock, Introduction to Magnetism and Magnetic Recording, John Wiley & Sons, (1999).
- [12] E. Clark, in Ferromagnetic Materials, ed E. P. Wolfarth, North-Holland, (1980).
- [13] B. D. Cullity and C. D. Graham, Introduction to Magnetic Materials, John Wiley & Sons, New Jersey, (2009).
- [14] S. Chikazumi, Physics of Magnetism, John Wiley & Sons, (1964).
- [15] T. Yogi and T. A. Nguyen, IEEE Trans. Magn., **29**, 307 (1993).
- [16] R. C. O. Handley, Modern Magnetic Materials, John Wiley and Sons, New York, (2000).

- [17] L. Néel, Influence des fluctuations thermiques sur l'aimanation de grains ferromagnétiques très fins, *Compt. Rend.*, 228:664, (1949).
- [18] C. P. Bean and F. E. Luborsky, *J. App. Phys.*, **30**, 120S (1959).
- [19] S. X. Wang and A. M. Taratorin, *Magnetic Information Storage Technology*, Academic Press, San Diego, CA, (1999).
- [20] E. C. Stoner and E. P. Wohlfarth. *Phil. Trans. Roy. Soc. (London)*, A240:599, (1948).
- [21] J. C. Mallinson, On Extremely High Density Recording, *IEEE Trans. Magn.*, **10**, 368 (1974).
- [22] D. Weller and A. Moser, *IEEE Trans. Magn.*, **35**, 4423 (1999).
- [23] M. P. Sharrock, *IEEE Trans. Magn.*, **35**, 4414 (1999).
- [24] N. Sekiguchi, , M. Terakawa, T. Akasaka, T. Fukuda, Y. Kamoshita, H. Ohnuma, *IEEE Trans. Magn.*, **44**, 3564 (2008).
- [25] H. Nishio, H. Yamamoto, *IEEE Trans. Magn.*, **46**, 3747 (2010).
- [26] S. Matsunuma, T. Inoue, T. Watanabe, T. Doi, S. Gomi, Y. Mashiko, K. Hirata, and S. Nakagawa, *J. Appl. Phys.*, **109**, 07B745 (2011).
- [27] K. Motohashi et al., *IEEE Trans. Magn.*, **43**, 2325 (2007).
- [28] M. P Sharrock, *IEEE Trans. Magn.*, **36**, 2420 (2000).
- [29] R. H. Dee, *Proc. IEEE*, **96**, 1775 (2008).
- [30] D. Berman et al., *IEEE Trans. Magn.*, **43**, 3502 (2007).
- [31] A. Matsumoto, Y. Murata, A. Musha, S. Matsubaguchi, and O. Shimizu, *IEEE Trans. Magn.*, **46**, 1208 (2010).
- [32] O. Shimizu, T. Harasawa, and M. Oyanagi, *IEEE Trans. Magn.*, **46**, 1607 (2010).
- [33] T. Harasawa, R. Suzuki, O. Shimizu, S. Olcer, and E. Eleftheriou, *IEEE Trans. Magn.*, vol. **46**, 1894 (2010).
- [34] R. D. Cideciyan et al., *IEEE Trans. Magn.*, **47**, 137 (2011).
- [35] J. Smit and H. P. J. Wijn, "Ferrites", Philips Techn. Library, Eindhoven (1959).
- [36] Adelsköld V *Arkiv Kemi Min. Geol.* A 121-9, (1938).

- [37] Y. Xu, G. Yang, D. Chu, and H. Zhai, *Phys. Stat. Sol. (b)* **157**, 685 (1990).
- [38] T. Ido, O. Kubo, and H. Yokoyama, *IEEE Trans. Magn.*, **22**, 704 (1986).
- [39] O. Kubo, T. Nomura, T. Ido, and H. Yokoyama, *IEEE Trans. Magn.*, **24**, 2859 (1988).
- [40] N. Sugita, M. Maekawa, Y. Ohta, K. Okinaka, and N. Nagai, *IEEE Trans. Magn.*, **31**, 2854 (1995).
- [41] Y. K. Hong, S. J. Park, and H. S. Jung, *J. Kor. Magnetism Society*, **5**, 216 (1995).
- [42] Y. K. Hong, S. J. Park, and H. S. Jung, *J. Kor. Magnetism Society*, **4**, 275 (1995).
- [43] G. B. The, S. Nagalingam, and D. A. Jefferson, *Mater. Chem. Phys.*, **101**, 158 (2007).
- [44] X. Z. Zhou, A. H. Morrish, Z. Yang, and H. X. Zeng, *J. Appl. Phys.*, **75** 5556 (1994).
- [45] D. H. Han and Z. Yang, *IEEE Trans. Magn.*, **31**, 2351 (1995).
- [46] Y. Xu, G. Yang, D. Chu, and H. Zhai, *Phys. Stat. Sol. (b)* **157**, 685 (1990).
- [47] T. Fujiwara, M. Isshiki, Y. Koike, and T. Oguchi, *IEEE Trans. Magn.*, **18**, 1200 (1982).
- [48] O. Kubo, T. Ido, and H. Yokoyama, *IEEE Trans. Magn.*, **18**, 1122 (1982).
- [49] D. E. Speliotis and K. Peter. *J. Magn. Magn. Mater.*, **120**, 28 (1993).
- [50] D. E. Speliotis, *IEEE Trans. Magn.*, **29**, 3613 (1993).
- [51] D. E. Speliotis, *IEEE Trans. Magn.*, **31**, 2877 (1995).
- [52] J. C. Mallinson, *IEEE Trans. Magn.* **10**, 368–374 (1974).
- [53] D. Weller and A. Moser, *IEEE Trans. Magn.* **35**, 4423 (1999).
- [54] M. P. Sharrock, *IEEE Trans. Magn.*, **35**, 4414 (1999).
- [55] A. Matsumoto, Y. Endo, and H. Noguchi, *IEEE Trans. Magn.*, **42**, 2315 (2006).
- [56] <http://www.oracle.com/technetwork/articles/systems-hardware-architecture/tape-dimensional-stability-294733.pdf>
- [57] <http://www.fujifilm.com/news/n100910.html>
- [58] <http://www.mydigitallife.info/fujifilm-and-ibm-tech-to-develop-35tb-magnetic-tape-drives/>

- [59] T. Harasawa, Recording Media Research & Development Laboratories, FUJIFILM Corporation “Development of Barium-Ferrite Particulate Media for High-Recording-Density Tape Storage Systems,” INSIC Tape Technology Forum IV, 4th-5th November, 2010.
- [60] Y. K. Hong and H. S. Jung, *J. Appl. Phys.*, **85**, 5549 (1999).
- [61] Y. K. Hong, F. J. Jeffers, and M. H. Park, *IEEE Trans. Magn.*, **36**, 3863 (2000).
- [62] Y. K. Hong, H. S. Jung, P. R. Taylor, US Patent 2003/0077382 A1, (2003).
- [63] P. Jubert, B. Biskeborn, D. Qiu, A. Matsumoto, H. Noguchi, and O. Shimizu, *IEEE Trans. Magn.* **47**, 386 (2011).
- [64] S. H. Gee, Y. K. Hong, F. J. Jeffers, J. C. Sur, M. H. Park, C. Weatherspoon, and I. T. Nam, *IEEE Trans. Magn.*, **41**, 4353 (2005).
- [65] J. Jalli, Y. K. Hong, S. Bae, G. S. Abo, J. J. Lee, J. C. Sur, S. H. Gee, S. G. Kim, S. C. Erwin, and A. Moitra, *IEEE Trans. Magn.*, **45**, 3590 (2009).
- [66] J. Jalli, Y. K. Hong, J. J. Lee, G. S. Abo, J. H. Park, A. M. Lane, S. G. Kim, and S. C. Erwin, *IEEE Magn. Lett.*, **1**, 4500204 (2010).
- [67] M. Cornell, U. Schwertmann, *The Iron Oxides Structure, Properties, Reactions, Occurrence and Uses*, second ed., Wiley–VCH, Weinheim, (2003).
- [68] Z. Zhang, S. Satpathy, *Phys. Rev. B.*, **44** 13319 (1991).
- [69] S. Soeya, J. Hayakawa, H. Takahashi, K. Ito, C. Yamamoto, A. Kida, H. Asano, M. Matsui, *Appl. Phys. Lett.*, **80**, 823 (2002).
- [70] S. Sun, C.B. Murray, D. Weller, L. Folks, A. Moser, *Science.*, **287** 1989 (2000).
- [71] J. Tang, K.Y. Wang, W. Zhou, *J. Appl. Phys.*, **89**,7690 (2001).
- [72] H. T. Pu, F.J. Jiang, *Nanotechnology.*, **16**, 1486 (2005).
- [73] D.K. Yi, S.S. Lee, J.Y. Ying, *Chem. Mater.*, **18**, 2459 (2006).
- [74] Q. A. Pankhurst, J. Connolly, S.K. Jones, J. Dobson, *J. Phys. D Appl. Phys.* **36** R167 (2003).
- [75] S. Mornet, S. Vasseur, F. Grasset, E. Duguet, *J. Mater. Chem.*, **14**, 2161 (2004).

- [76] R. Weissleder, D.D. Stark, B.L. Engelstad, B.R. Bacon, C.C. Compton, D.L. White, P. Jacobs, J. Lewis, *Am. J. Rentgenol.* **152**, 167 (1989).
- [77] D. T. Harvey, R.W. Linton, *Anal. Chem.*, **53**, 1684 (1981).
- [78] Z. J. Zhang, Z.L. Wang, B.C. Chakoumakos, J.S. Yin, *J. Am. Chem. Soc.*, **120**, 1800 (1998).
- [79] S. Si, C. Li, X. Wang, D. Yu, Q. Peng, Y. Li, *Cryst. Growth. Des.*, **5**, 391 (2005).
- [80] J. Rockenberger, E.C. Scher, A.P. Alivisatos, *J. Am. Chem. Soc.*, **121**, 11595 (1999).
- [81] T. Hyeon, S.S. Lee, J. Park, Y. Chung, H.B. Na, *J. Am. Chem. Soc.*, **123**, 12798 (2001).
- [82] J. Park, K. An, Y. Hwang, J. G. Park, H. J. Noh, J.Y. Kim, J. H. Park, N. M. Hwang, T. Hyeon, *Nat. Mater.*, **3**, 891 (2004).
- [83] J. Smit and H. P. J. Wijn, *Ferrites; physical properties of ferromagnetic oxides in relation to their technical applications*, International Edition, Philip's Technical Library, Eindhoven, The Netherlands (1965).
- [84] A. H. Morrish, *Canted Antiferromagnetism: Hematite* ~World Scientific, Singapore, (1994).
- [85] R. M. Cornell and U. Schwertmann, *The Iron Oxides, Structure, Properties, Occurrences and Uses* ~VCH, Weinheim, (1996).
- [86] K. M. Rosso, D. M. A Smith, and M. Dupuis, An ab initio model of electron transport in hematite ( $\alpha$ -Fe<sub>2</sub>O<sub>3</sub>) basal planes. *J. Chem. Phys.*, **118**, 6455 (2003).
- [87] P. A. Cox *Transition metal oxides: An introduction to their electronic structure and properties*. Oxford University Press, England, 1992.
- [88] F. J. Morin Electrical properties of  $\alpha$ -Fe<sub>2</sub>O<sub>3</sub>. *Phys. Rev.*, **93**, 1195 (1954).
- [89] F. J. Morin Electrical properties of  $\alpha$ -Fe<sub>2</sub>O<sub>3</sub> and  $\alpha$ -Fe<sub>2</sub>O<sub>3</sub> containing titanium. *Phys. Rev.*, **83**, 1005 (1951).
- [90] D. Adler *Insulating and metallic states in transition metal oxides*, *Solid State Physics.*, **21** 1-111. Academic Press, (1968).
- [91] T. Townsend Smith, *Phys. Rev.*, **8**, 721 (1916).
- [92] M. Ozaki, N. Ookoshi, E. Matijevic, *J. Colloid Interface Sci.*, **137**, 546 (1990).
- [93] J. K. Bailey, C. J. Brinker, M. L. Mecartney, *J. Colloid Interafce Sci.*, **157**, 1 (1993).

- [94] M. Gotic', Popovic', S. Ljubes'ic', N. Music', S. J. Mater. Sci., **29**, 2474 (1994).
- [95] T. Sugimoto, A. Muramatsu, K. Sakata, D. Shindo, J. Colloid Interface Sci., **158**, 420 (1993).
- [96] T. Sugimoto, A. Muramatsu, J. Colloid Interface., **184**, 626 (1996).
- [97] T. Sugimoto, Y. Wang, H. Itoh, A. Muramatsu, Colloids Surf. A, **134**, 265 (1998).
- [98] S. Kan, S. Yu, X. Peng, X. Zhang, D. Li, L. Xiao, G. Zou, T. Li, J. Colloid Interface Sci., **178**, 673 (1996).
- [99] S. Kan, X. Zhang, S. Yu, S. D. Li, L. Xiao, G. Zou, T. Li, W. Dong, Y. Lu, J. Colloid Interface Sci., **191**, 503 (1997).
- [100] K. Kandori, J. Sakai, T. Ishikawa, Phys. Chem. Chem. Phys., **2**, 3293 (2000).
- [101] H. Katsuki, S. Komarneni, J. Am. Ceram. Soc., **84**, 2313 (2001).
- [102] S. Music', S. Krehula.; Popovic', S. Mater. Lett, **58**, 2640 (2004).
- [103] Liang, X.; Wang, X.; Zhuang, J.; Chen, Y.; Wang, D.; Li, Y. Adv. Funct. Mater., **16**, 1805 (2006).
- [104] S. Wang, Y. Min, and S. H. Yu, J. Phys. Chem. C., **111**, 3551 (2007).
- [105] J. Jalli, Y. K. Hong, S. Bae, J. J. Lee, J. H. Park, G. S. Abo, A. M. Lane, S. G. Kim, B. C. Choi, M. J. Kim, S. C. Erwin, T. Hyeon, R. Syslo, and N. Neveu, "Large scale synthesis of monodisperse antiferromagnetic nanocubes" Paper no: **AT-14**, presented at the 55th Magnetism and Magnetic Materials Conference, Atlanta, Georgia, November 14-18, 2010.
- [106] J. Jalli, Y. K. Hong, C. S. Kim, C. M. Kim, J. H. Park, J. J. Lee, G. S. Abo, A. Romero, A. Rodriguez, "Mössbauer and X-ray Spectromicroscopy Studies of Hematite ( $\alpha$ -Fe<sub>2</sub>O<sub>3</sub>) Nanocubes" Paper no: **CE-03**, presented at the 56<sup>th</sup> Annual Conference on Magnetism and Magnetic Materials, Scottsdale, AZ, 30 October-3 November (2011).
- [107] J. Jalli, Y. Hong, S. Gee, J. C. Sur, K. An and T. Hyeon, "Spherical Barium Ferrite (S-BaFe) 20-22 nm sized particles for particulate recording media", Paper No. **CW-08** (poster), presented at the 53rd Annual Conference on Magnetism and Magnetic Materials, Austin, TX, Nov. 10-14, (2008).
- [108] A. M. Homola, M. R. Lorenz, C. J. Mastrangelo, and T. L. Tibury, "Novel magnetic dispersions using silica stabilized particles," IEEE Trans. Magn., **22**, 716 (1985).
- [109] H. P. Steier, J. Requena and J. S. Moya, J. Mater. Res., **14**, 3647 (1999).

- [110] M. P. Sharrock, IEEE Trans. Magn., **35**, 4414 (1999).
- [111] E. C. Stoner and E. P. Wohlfarth, Phil. Trans. Roy. Soc., **A 240**, 599 (1948).
- [112] K. V. P. M. Shafi, Y. Kolytyn, A. Gedanken, R. Prozorov, Balogh, J. Lendvai, and Felner I (1997), "Sonochemical Preparation of Nanosized Amorphous NiFe<sub>2</sub>O<sub>4</sub> Particles." J. Phys. Chem. B **101**, pp. 6409-6414.
- [113] G. S. Abo, Y. K. Hong, J. Jalli, S. Bae, J. Lee, J. Park, N. Neveu, S. Kim, J. C. Sur "Modeling of hysteresis loops for spherical barium ferrite (S-BaFe) particles with uniaxial anisotropy," paper no. **DP-06**, presented at the 11<sup>th</sup> Joint MMM-Intermag conference, Washington, DC, January 18-22 (2010).
- [114] G. S. Abo, J. J. Lee, J. H. Park, S. Bae, S. G. Kim, B. C. Choi and T. Tanaka, J of Magnetism, **17**, 1 (2012).
- [115] K. Song, M. R. Parker, J. W. Harrell., J. of Mag. and Mag. Matr., **120**,180 (1993).
- [116] T. Fujiwara, IEEE Trans. Magn., **5**, 3125 (1987)
- [117] Z. L. Wang, J. M. Petroski, T. C. Green, and M. A. El-Sayed., J. of Phys. Chem. B., **102**,6145 (1998).

## Part II. Hexaferrite Single Crystals

- [1] V. Voronkov, J. Phys IV France., **7**, C1-35 (1997).
- [2] H. S. Newman, D. C. Web, and C. M. Krowne, "International conference on millimeter and submillimeter waves and applications III," Proceedings of SPE., **181**, 2842 (1996).
- [3] U. Ozgur, Y. Alivov, H. Morkoc, Microwave Ferrites, Part 1: Fundamental properties, Journal of Materials Science Materials in Electronics., **20**, 789 (2009).
- [4] G. Winkler and H. Doetsch, "Hexagonal ferrites at millimeter wavelengths," 9<sup>th</sup> Microwave Conference European Microwave., **79**, 13 (1979).
- [5] N. Zeina, H. How, C. Vitoria, and R. West, IEEE Trans. Magn., **28**, 3219 (1992).
- [6] A. J. Baden Fuller, Ferrites at Microwave Frequencies, Peter Peregrinus Ltd., London, (1987).
- [7] W. H. von Aulock, Handbook of Microwave Ferrite Materials, Academic Press Inc., New York, (1965).

- [8] H. Kojima, *Ferromagnetic Materials*, Vol. **3**, edited by E. P. Wohlfarth, North-Holland Publishing Co., New York, (1982).
- [9] J. Smit and H. P. J. Wijn: *Ferrites*, John Wiley & Sons, Inc., New York, (1959).
- [10] V. Adelsköld, *Arkiv Kemi, Min. Geol.*, **A12**, 1(1938).
- [11] G. H. Jonker, H. P. Wijn, P. B. Braun, *Philips Technol. Rev.*, **18**, 145 (1956-1957)
- [12] Y. Xu, G. Yang, D. Chu, and H. Zhai, *Phys. Stat. Sol.(b)*., **157**, 685 (1990).
- [13] T. Ido, O. Kubo, and H. Yokoyama, *IEEE Trans. Magn.*, **22**, 704 (1986).
- [14] O. Kubo, T. Nomura, T. Ido, and H. Yokoyama, *IEEE Trans. Magn.*, **24**, 2859 (1988).
- [15] N. Sugita, M. Maekawa, Y. Ohta, K. Okinaka, and N. Nagai, *IEEE Trans. Magn.*, **31**, 2854 (1995).
- [16] Y. K. Hong, S. J. Park, and H. S. Jung, *J. Kor. Magnetism Society.*, **5**, 216 (1995).
- [17] Y. K. Hong, S. J. Park, and H. S. Jung, *J. Kor. Magnetism Society.*, **4**, 275 (1995).
- [18] G. B. The, S. Nagalingam, and D. A. Jefferson, *Mater. Chem. Phys.*, **101**, 158 (2007).
- [19] X. Z. Zhou, A. H. Morrish, Z. Yang, and H. X. Zeng, *J. Appl. Phys.*, **75** 5556 (1994).
- [20] K. Shiban Koul and Bharathi Bhat: *Microwave and Millimeter Wave Phase Shifters*, Vol. **1** Dielectric and Ferrite Phase Shifters, Artech House, Inc., Norwood, (1991).
- [21] Joseph Helszajn: *Ferrite Phase Shifters and Control Devices*, McGraw-Hill Book Company Limited, (1989).
- [22] Y. Bai, J. Zhou, Z. Gui, Z. Yue, and L. Li, *J. of Mag. and Mag. Mater.*, **264**, 44 (2003).
- [23] Xu Fang, Bai Yang, Ai Fen and Qiao Li-Jie, *Chinese Phys. B.*, **17**, 4652 (2008).
- [24] R. O. Savage Jr, S. Dixon Jr, and A. Tauber, *J. of Appl. Phys.*, **36**, 873 (1964).
- [25] S. Ishiwata, Y. Taguchi, H. Murakawa, Y. Onose, Y. Tokura, *Science.*, **319**, 1643 (2008).
- [26] T. Kimura, G. Lawes, and A. P. Ramirez, *Phys. Rev. Lett.* **94.**, 137201 (2005).
- [27] S. H. Chun, Y. S. Chai, Y. S. Oh, D. J. Nagar, S. Y. Haam, I. Kim. B. Lee, D. H. Nam, K. T. Ko, J. H. Park, J. H. Chung, and K. H. Kim, *Phys. Rev. Lett.*, **104**, 037204 (2010).

- [28] C. Vittoria: Microwave Properties of Magnetic Films, World Scientific Publishing Co. Pte. Ltd., Singapore, (1993).
- [29] D. Polder, "On the Theory of Ferromagnetic Resonance", Philosophical Magazine, Vol. **40**, pp. 99-115, (1949).
- [30] A. W. Scott, Understanding Microwaves. John Wiley & Sons, New York, (1993).
- [31] Dexter Magnetic Technologies International, <http://dextermag.com/default.aspx>.
- [32] H. Bosma, IEEE Trans. on Microwave Theory and Techniques., **12**, 61 (1964).
- [33] C. E. Fay and R. L. Comstock, IEEE Trans. on Microwave Theory and Techniques., **13**, 15 (1965).
- [34] D. B. Nicholson, "Hexagonal ferrites for millimeter-wave applications," Hewlett-Packard Journal., **41**, 59 (1990).
- [35] J. Jalli, Y. K. Hong, S. Bae, J. J. Lee, G. S. Abo, A. Lyle, S. H. Gee, H. Lee, T. Mewes, J. C. Sur, and S. I. Lee, J. Appl. Phys., **105**, 07A511(2009).
- [36] J. Jalli, Y. K. Hong, S. H. Gee, S. Bae, J. J. Lee, J. C. Sur, G. S. Abo, A. Lyle, S. I. Lee, H. Lee, and T. Mewes, IEEE Transactions on Magnetics., **44**, 2978 (2008).
- [37] J. Jalli, Y. K. Hong, S. Bae, J. J. Lee, G. S. Abo, J. H. Park, T. Mewes, B. C. Choi, and S. G. Kim, IEEE Magnetic Letters, **2**, 5000104 (2011).
- [38] J. Jalli, Y. K. Hong, S. Bae, J. J. Lee, G. S. Abo, J. H. Park, S. G. Kim, T. Mewes, B. C. Choi, S. H. Gee, S. C. Erwin, I. T. Nam, and T. Tanaka, J. Appl. Phys., **109**, 07A509 (2011).
- [39] J. Jalli, Y. K. Hong, G. S. Abo, S. Bae, J. J. Lee, J. H. Park, B. C. Choi, and S. G. Kim, J. of Mag. and Mag. Mater., **323**, 2627 (2011).
- [40] M. Matsuoka, Y. Hoshi, M. Naoe, and S. Yamanaka, IEEE Trans. Magn., **20**, 800 (1984).
- [41] S. Pignard, H. Vincent, and J. P. Senateur, Thin Solid Films., **350**, 119 (1999).
- [42] S. D. Yoon and C. Vittoria, J. Appl. Phys., **96**, 2131 (2004).
- [43] S. D. Yoon and C. Vittoria, IEEE Trans. Magn., **39**, 3163 (2003).
- [44] S. D. Yoon and C. Vittoria, J. Appl. Phys., **93**, 8597 (2003).
- [45] S. G. Wang, S. D. Yoon, and C. Vittoria, J. Appl. Phys., **92**, 6728 (2002).
- [46] R. C. Linares and E. L. Sloan, III, J. Cryst. Growth., **27**, 249 (1974).

- [47] R. Hiskes, *J. Cryst. Growth.*, **27**, 287 (1974).
- [48] R. J. Gambino and F. Leonhard, *J. Am. Ceram. Soc.*, **44**, 221 (1961).
- [49] A. K. Srivastava et al, *J. Appl. Phys.*, **85**, 7838 (1999).
- [50] M. A. Wittenauer, J. A. Nyenhuis A. I. Schindler, H. Sato, F. J. Friedlaender, J. Truedson, R. Karim and C.E. Patton, *J. Cryst. Growth.*, **130**, 533 (1993).
- [51] S. D. Yoon and C. Vittoria, *J. Magn. Magn. Mater.*, **E1833-E1834**, 272 (2004).
- [52] G. P. Rodrigue, *IEEE Trans. Microwave Theory Tech.*, **11**, 351, (1963).
- [53] C. Vittoria, *J. Magn. Mag. Mater.*, **21**, 109, (1980).
- [54] G. F. Dionne and J. F. Fitzgerald, *J. Appl. Phys.*, **70**, 6140 (1991).
- [55] X. Zuo, H. How, S. Somu, and C. Vittoria, *IEEE Trans. Magn.*, **39**, 3160, (2003).
- [56] Y. Kubota, T. Takami, and Y. Ogata, *Hitachi Metals Technical Review.*, **15**, 65 (1999).
- [57] F. Kools, A. Morel, P. Tenaud, R. Rossignol, O. Isnard, R. Grössinger, P. Tenaud, *J. Magn. Mag. Mater.*, **242**, 1270, (2002).
- [58] X. Liu, W. Zhong, S. Yang, Z. Yu, B. Gu, and Y. Du, *J. Magn. Magn. Mater.*, **238**, 207 (2002).
- [59] R. Grössinger, M. Küpferling, J. C. Tellez Blanco, G. Wiesinger, M. Müller, G. Hilscher, M. W. Pieper, J. F. Wang, and I. R. Harris, *IEEE Trans. Magn.*, **39**, 2911( 2003).
- [60] Jean-Marie Le Breton, Jacques Teillet, Günter Wiesinger, Antoine Morel, Frans Kools, and Philippe Tenaud, *IEEE Trans. Magn.*, **38**, 2952, (2002).
- [61] J. M. Le Breton, G. Wiesinger, C. Tellez Blanco, O. Isnard, J. Teillet, R. Grössinger, A. Morel, F. Kools, and P. Tenaud, *Proc. 8th Int. Conf. Ferrites, Kyoto, Japan, Sept. 18–21*, pp. 199-201(2000).
- [62] Ch. Sauer, U. Köbler, W. Zinn, and H. Stäblein, *J. Phys. Chem. Solids.*, **39**,1197 (1978).
- [63] J. F. Wanga, C. B. Pontonb, and I. R. Harris, *J. Magn. Magn. Mater.*, **234**, 233( 2001).
- [64] A. Tauber, S. Dixon Jr. and R. O. Savage Jr., *J. Appl. Phys.*, **35**, 1008 (1964).
- [65] N. Momozawa, M. Mita and H. Takei, *J. Cryst. Growth.*, **83**, 403 (1987).

- [66] N. Momozawa, Y. Yamaguchi, H. Takei and M. Mita, *J. Phys. Soc. Jpn.*, **54**, 3895 (1985).
- [67] S. Utsumi, D. Yoshiba, and N. Momozawa, *J. Phys. Soc. Jpn.*, **76**, 034704-1 (2007).
- [68] Y. Chen, A. L. Geiler, T. Chen, T. Sakai, C. Vittoria, and V. G. Harris, *J. Appl. Phys.*, **101**, 09M501 (2007).
- [69] Y. Bai, J. Zhou, Z. Gui, Z. Yue, and L. Li, *J. of Mag. and Mag. Mater.*, **264**, 44 (2003).
- [70] X. Fang, B. Yang, A. Fen and Q. Li-Jie, *Chinese Phys. B.*, **17**, 4652 (2008).
- [71] R. O. Savage Jr, S. Dixon Jr, and A. Tauber, *J. of Appl. Phys.*, **36**, 873 (1964).
- [72] A. L. Geiler, J. Wang, J. S. Gao, S. D Yoon, Y. Chen, V. G. Harris, and C. Vittoria, *IEEE Trans. Magn.*, **45**, 4179 (2009).
- [73] G. Albanese, M. Carbucicchio, A. Deriu, G. Asti and S. Rinaldi, *Applied Physics A* **7**, 227 (1975).
- [74] M. J. Iqbal and B. Ain, *Materials Science and Engineering B.*, **164**, 6 (2009).
- [75] H. B. G. Casimir, J. Smit, U. Enz, J. F. Fast, H. P. J. Wijn, E. W. Gorter, A. J. W. Duyvesteyn, J. D. Fast et and J. J. de Jong , *J. Phys. Rad.*, **20**, 2 (1959).
- [76] A. A. Sattar, H.M. El-Sayed, W.R. Agami and A.A. Ghani, *American Journal of Applied Sciences.*, **4**, 89 (2007).
- [77] M. Obol and C. Vittoria, *IEEE Trans. Magn.*, **39**, 3103 (2003).
- [78] C. Kooy and U. Enz, *Philips Res. Rep.*, **15**, 7 (1960).
- [79] L. F. Bates, D. J. Craik, P. M. Griffiths, and E. D. Isaac, *Proc. R. Soc. Lond. A*, **253**, 1 (1959).
- [80] J. Kaczér and R. Gemperle, *Czech. J. Phys. B.*, **10**, 505 (1960).
- [81] H. Kojima and K. Goto, *J. Phys. Soc. Jap.*, **16**, 1483 (1961).
- [82] K. Gotō, *Jap. J. of Appl. Phys.*, **5**, 117 (1966).
- [83] R. G. Wells and D. V. Ratnam, *IEEE Trans. Magn.*, **7**, 651(1971).
- [84] R. Gemperle, V. Kamberský, J. imová, L. Murtinová, L. Pst, P. Görnet W. Schüppel, and R. Gerber, *J. of Mag. and Mag. Mater.*, **118**, 295(1993).

- [85] U. Kaiser, A. Schwarz, and R. Wiesendanger, *Nature Letters.*, **446**, 522 (2007).
- [86] D. Rugar, H. J. Mamin, P. Guethner, S. E. Lambert, J. E. Stern, I. McFadyen, and T. Yogi, *J. Appl. Phys.*, **68**, 1169 (1990).
- [87] Y. Chen, M. Xiao, J. Zhu, and M. H. Kryder, *IEEE Trans. Magn.*, **35**, 583 (1999).
- [88] Q. F. Li, X. D. Su, H. Li, L. Zhang, Z. H. Liu and H. J. Zhong, *J. Appl. Phys.*, **106**, 123914 (2009).
- [89] L. Zhanga, X. D. Sua, Y. Chen, Q. F. Li, and V.G. Harris, *J. Appl. Phys.*, **63**, 492 (2010).
- [90] B. D. Cullity and C. D. Graham, *Introduction to Magnetic Materials*, John Wiley & Sons, New Jersey, (2009).
- [91] C. A. Carosella, D. B. Chrisey, P. Lubitz, J. S. Horwitz, P. Dorsey, R. Seed, and C. Vittoria, *J. Appl. Phys.*, **71**, 5107 (1992).
- [92] H. Kojima, and E. P. Wohlfarth, "Fundamental properties of hexagonal ferrites," *Ferromagnetic Materials*, **3**, 305, North-Holland (1982).

## APPENDIX A.

### List of Publications by the Author

1. G. S. Abo, Y. K. Hong, J. Jalli, J. J. Lee, J. H. Park, S. Bae, S. G. Kim, B. C. Choi and T. Tanaka, "Shape Dependent Coercivity Simulation of a Spherical Barium Ferrite (S-BaFe) Particle with Uniaxial Anisotropy" *J of Magnetics*, **17**(1), 1-5 (2012).
2. G. S. Abo, Y. K. Hong, S. Bae, J. Jalli, J. H. Park, J. J. Lee, R. Syslo, and N. Neveu, "Micromagnetic Computer Simulated Scaling Effect of S-Shaped Permalloy Nano-Element on Operating Fields for AND or OR Logic" *IEEE Transactions on Magnetics*, **99**, 1-1 (2011).
3. J. Jalli, Y. K. Hong, S. Bae, J. J. Lee, G. S. Abo, J. H. Park, T. Mewes, B. C. Choi, and S. G. Kim, "Ferrimagnetic  $\text{Sr}_{1.5}\text{Ba}_{0.5}\text{Zn}_2\text{Fe}_{12}\text{O}_{22}$  Single Crystal with Planar Anisotropy" *IEEE Magnetic Letters* **2**, 5000104 (2011).
4. J. Jalli, Y. K. Hong, G. S. Abo, S. Bae, J. J. Lee, J. H. Park, B. C. Choi, and S. G. Kim "MFM studies of magnetic domain patterns in bulk barium ferrite ( $\text{BaFe}_{12}\text{O}_{19}$ ) single crystals", *Journal of Magnetism and Magnetic Materials*, **323**, Issue 21, p. 2627-2631,(2011).
5. J. Jalli, Y. K. Hong, S. Bae, J. J. Lee, G. S. Abo, J. H. Park, S. G. Kim, T. Mewes, B. C. Choi, S. H. Gee, S. C. Erwin, I. T. Nam, and T. Tanaka "Magnetic and microwave properties of ferrimagnetic Zr-substituted  $\text{Ba}_2\text{Zn}_2\text{Fe}_{12}\text{O}_{22}$  (ZnY) single crystal" *J. Appl. Phys.*,**109**, 07A509 (2011).
6. J. J. Lee, Y. K. Hong, S. Bae, J. Jalli, G. S. Abo, J. H. Park, W. M. Seong, S. H. Park, and W. Ki Ahn "Low loss  $\text{Co}_2\text{Z}$  ( $\text{Ba}_3\text{Co}_2\text{Fe}_{24}\text{O}_{41}$ ) glass composite for GHz antenna application" *J. Appl. Phys.*, **109**, 07E530 (2011).
7. J. J. Lee, Y. K. Hong, S. Bae, J. Jalli, J. H. Park, G. S. Abo, G. W. Donohoe, and B. C. Choi, "Integrated Ferrite Film Inductor for Power System-on-chip (PowerSoC) Smart Phone Applications," to be published in, *IEEE Transactions on Magnetics*, vol. **47** February, (2011).
8. S. Bae, Y. K. Hong, J. J. Lee, J. H. Park, J. Jalli, G. S. Abo, W. M. Seong, S. H. Park, J. S. Kum, W. K. Ahn, and G. H. Kim, "Dual-Band Ferrite Chip Antenna for GPS and Bluetooth Applications," *Microwave and Optical Technology Letters*, vol. **53**, 14 (2011).
9. J. Jalli, Y. K. Hong, J. J. Lee, G. S. Abo, J. H. Park, A. M. Lane, S. G. Kim, S. C. Erwin "Conversion of Worm-Shaped Antiferromagnetic Hematite to Ferrimagnetic Spherical

- Barium-Ferrite Nanoparticles for Particulate Recording Media,” IEEE Magnetic Letters, vol. **1**, 4500204 (2010).
10. S. Bae, Y. K. Hong, J. J. Lee, J. H. Park, J. Jalli, G. S. Abo, H. M. Kwon, and C. K. K. Jayasooriya, “Miniature and higher-order mode ferrite MIMO ring patch antenna for mobile communication system,” Progress in Electromagnetics Research B, vol. **25**, 53 (2010).
  11. A. Lyle, Y. K. Hong, B. C. Choi, G. S. Abo, J. Jalli, R. Syslo, S. Bae, J. J. Lee, M. H. Park, and G. W. Donohoe, “Spin-polarized current switching of Co/Cu/Py Pac-man type II, J. of Magnetism, vol. **15**, 103 (2010).
  12. J. J. Lee, Y. K. Hong, S. Bae, J. Park, J. Jalli, G. S. Abo, B. Choi, and G. W. Donohoe, “High quality factor Ni-Zn Ferrite Planar Inductor”, IEEE Transactions on Magnetism, vol. **46**, 2417 (2010).
  13. S. Bae, Y. Hong, J. Lee, W. Sung, J. Kum, W. Ahn, S. Park, G. S. Abo, J. Jalli, and J. Park, “Miniaturized broadband ferrite T-DMB antennas for mobile phone applications”, IEEE Transactions on Magnetism, vol. **46**, 2361 (2010).
  14. J. Park, Y. Hong, S. Bae, J. J. Lee, J. Jalli, G. S. Abo, N. Neveu, C. Choi, J. Lee, “Saturation Magnetization and crystalline anisotropy calculations for MnAl permanent magnet”, J. Appl Phys., vol.**107**, 09A731(2010).
  15. J. Jalli, Y. K. Hong, S. Bae, G. S. Abo, J. J. Lee, J. C. Sur, S. H. Gee, S. G. Kim, S. C. Erwin, and A. Moitra, “Conversion of nanosized spherical magnetite to spherical barium ferrite nanoparticles for high density particulate recording media”, IEEE Transactions on Magnetism, vol.**45**, 3590 (2009).
  16. J. Jalli, Y. K. Hong, S. Bae, J. J. Lee, G. S. Abo, A. Lyle, S. H. Gee, H. Lee, T. Mewes, J. C. Sur, and S. I. Lee, “Growth and characterization of 144  $\mu\text{m}$  thick barium ferrite single crystalline film for microwave device application”, J. Appl. Phys., vol.**105**, 07A511(2009).
  17. S. Bae, Y. K. Hong, J. J. Lee, J. Jalli, G. S. Abo, A. Lyle, B. C. Choi, and G. W. Donohoe, “High Q Ni-Zn-Cu ferrite inductor for on-chip power module”, IEEE Transactions on Magnetism, vol.**45**, 4773 (2009).
  18. J. J. Lee, Y. K. Hong, S. Bae, J. Jalli, G. S. Abo, W. M. Seonug, W. G. Ahn, S. H. Park, C. J. Choi, and J. G. Lee, “Broadband  $\text{Ni}_x\text{Zn}_{0.8-x}\text{Cu}_{0.2}\text{Fe}_2\text{O}_4$  electromagnetic absorber for 1 GHz application”, IEEE Transactions on Magnetism, vol. **45**, 4230 (2009).
  19. S. Bae, Y. K. Hong, J. J. Lee, J. Jalli, G. S. Abo, W. M. Sung, G. H. Kim, S. H. Park, J. S. Kum, and H. M. Kwon, “ $\text{Co}_2\text{Z}$  hexaferrite T-DMB antenna for mobile phone applications”, IEEE Transactions on Magnetism, vol.**45**, 4199 (2009).

20. S. Bae, Y. K. Hong, J. J. Lee, J. Jalli, G. S. Abo, A. Lyle, I. T. Nam, W. M. Seong, J. S. Kum, and S. H. Park, "New synthetic route of Z-type ( $\text{Ba}_3\text{Co}_2\text{Fe}_{24}\text{O}_{41}$ ) hexaferrite particles", IEEE Transactions on Magnetics, vol.**45**, 2557 (2009).
21. A. Lyle, Y. K. Hong, B. C. Choi, G. S. Abo, M. H. Park, S. H. Gee, J. Jalli, S. Bae, and G. W. Donohoe, "Spin-polarized current switching of Co/Cu/Py elongated Pac-man spin-valve", IEEE Transactions on Magnetics, vol. **45**, 2367(2009).
22. S. Bae, Y. K. Hong, J. J. Lee, J. Jalli, G. S. Abo, A. Lyle, W. M. Seong, and J. S. Kum, "Low loss Z-type barium ferrite ( $\text{Co}_2\text{Z}$ ) for terrestrial digital multimedia broadcasting antenna application", J. Appl. Phys., vol.**105**, 07A515(2009).
23. J. J. Lee, S. Bae, Y. K. Hong, J. Jalli, G. S. Abo, W. M. Seong, S. H. Park, C. J. Choi, and J. G. Lee, "Novel Ni–Mn–Co ferrite for gigahertz chip devices", J. Appl. Phys., vol. **105**, 07A514 (2009).
24. J. Jalli, Y. K. Hong, S. H. Gee, S. Bae, J. J. Lee, J. C. Sur, G. S. Abo, A. Lyle, S. I. Lee, H. Lee, and T. Mewes, "Magnetic and microwave properties of Sm-doped  $\text{SrFe}_{12}\text{O}_{19}$  single crystals", IEEE Transactions on Magnetics, vol. **44**, 2978 (2008).
25. S. Bae, Y. K. Hong, J. J. Lee, G. Abo, J. Jalli, A. Lyle, H. Han, and G. W. Donohoe, "Optimized design of low voltage high current ferrite planar inductor for 10 MHz on-chip power module", Journal of Magnetics, vol.**13**, 37 (2008).

## APPENDIX B.

### List of Presentations by the Author

1. J. Jalli, Y. K. Hong, C. S. Kim, C. M Kim, J. H. Park, J. J Lee, G. S Abo, A. Romero, A. Rodriguez, "Mössbauer and X-ray Spectromicroscopy Studies of Hematite ( $\alpha$ -Fe<sub>2</sub>O<sub>3</sub>) Nanocubes" presented at the 56th Annual Conference on Magnetism and Magnetic Materials, Scottsdale, AZ, 30 October-3 November 2011.
2. J. Lee, Y. K. Hong, S. Bae, G. S. Abo, J. Park, J. Jalli, W. M. Seong, S. H. Park, W. K. Ahn, and G. Kim "Co<sub>2</sub>Z hexaferrite-glass composite chip antenna for global positioning systems," Paper no: 1550, accepted for presentation at the 2011 IEEE AP-S International Symposium on Antennas and Propagation and 2011 USNC/URSI National Radio Science Meeting in Spokane, Washington, USA, July 3-8, 2011.
3. J. Jalli, Y. K. Hong, S. Bae, J. J. Lee, J. H. Park, G. S. Abo, A. M. Lane, S. G. Kim, B. C. Choi, M. J. Kim, S. C. Erwin, T. Hyeon, R. Syslo, and N. Neveu, "Large scale synthesis of monodisperse antiferromagnetic nanocubes" Paper no: AT-14 (Poster), accepted for presentation at the 55th Magnetism and Magnetic Materials Conference, Atlanta, Georgia, November 14-18, 2010.
4. J. Jalli, Y. K. Hong, S. Bae, J. J. Lee, G. S. Abo, J. H. Park, S. G. Kim, T. Mewes, B. C. Choi, S. H. Gee, S. C. Erwin, I. T. Nam, T. Tanaka, R. Syslo, and N. Neveu, "Magnetic and microwave properties of ferrimagnetic Zr-substituted Ba<sub>2</sub>Zn<sub>2</sub>Fe<sub>12</sub>O<sub>22</sub> (ZnY) single crystal" Paper no: DW-04 (Poster), accepted for presentation at the 55th Magnetism and Magnetic Materials Conference, Atlanta, Georgia, November 14-18, 2010.
5. J. J. Lee, Y. K. Hong, S. Bae, J. Jalli, G. S. Abo, J. H. Park, W. M Seong, S. H Park, W. K. Ahn, G. H. Kim, F. Yang, A. Yu, R. Syslo, and N. Neveu, "Broadband GHz Co<sub>2</sub>Z hexaferrite (Ba<sub>2</sub>Co<sub>3</sub>Fe<sub>24</sub>O<sub>41</sub>)-glass composite Bluetooth antenna," Paper no: HE-06 (Oral), accepted for presentation at the 55th Magnetism and Magnetic Materials Conference, Atlanta, Georgia, November 14-18, 2010.
6. J. J. Lee, Y. K Hong, S. Bae, J. Jalli, G. S. Abo, J. H. Park, W. M. Seong, S. H. Park, W. K. Ahn, R. Syslo, and N. Neveu, "Low loss Co<sub>2</sub>Z (Ba<sub>3</sub>Co<sub>2</sub>Fe<sub>24</sub>O<sub>41</sub>)-glass composite for gigahertz antenna application," Paper no: HE-02 (Oral), accepted for presentation at the 55th Magnetism and Magnetic Materials Conference, Atlanta, Georgia, November 14-18, 2010.
7. J. H. Park, Y. K. Hong, S. Bae, J. J. Lee, G. S. Abo, J. Jalli, C. J. Choi, J. G. Lee, S. G. Kim, O. Mryasov, B. C. Choi, S. C. Erwin, R. Syslo, and N. Neveu, "Magnetization and high temperature (BH) max of ferromagnetic low temperature phase MnB, " Paper no:

- HF-08 (Oral), accepted for presentation at the 55th Magnetism and Magnetic Materials Conference, Atlanta, Georgia, November 14-18, 2010.
8. S. Bae, Y. K. Hong, J. J. Lee, J. H. Park, J. Jalli, G. S. Abo, W. M. Seong, S. H. Park, W. K. Ahn, "Soft magnetic  $\text{SrFe}_7\text{Sn}_{2.5}\text{Zn}_{2.5}\text{O}_{19}$  hexaferrite for GHz antenna applications," paper No. HE-09 (Oral), accepted for presentation at the 55th Magnetism and Magnetic Materials Conference, Atlanta, Georgia, November 14-18, 2010.
  9. G. S. Abo, Y. K. Hong, B. C. Choi, J. Jalli, S. Bae, J. J. Lee, J. H. Park, G. W. Donohoe, and M. H. Park, "Scaling effect of S-shaped permalloy nano-element on bias field," accepted for presentation at The IEEE 7<sup>th</sup> International symposium on metallic multilayers (MML2010), September 19-24, 2010, Berkeley, California.
  10. J. H. Park, Y. K. Hong, S. Bae, J. J. Lee, G. S. Abo, J. Jalli, C. J. Choi, J. G. Lee, S. G. Kim and A. Moitra, "First-principles Calculations of Magnetic Moment and Anisotropy Constant for LTP MnBi," paper No. AMF-0679 (oral), presented at the 7<sup>th</sup> Asian Meeting on Ferroelectricity, Jeju, South Korea, June 28 - July 1, 2010.
  11. J. J. Lee, Y. K. Hong, S. Bae, J. H. Park, J. Jalli, G. S. Abo, W. M. Seong, S. H. Park, J. S. Kum, W. K. Ahn and G. H. Kim, "Broadband Bluetooth Antenna based on  $\text{Co}_2\text{Z}$  Hexaferrite-Glass Composite," paper No. AMF-0780 (poster), presented at the 7<sup>th</sup> Asian Meeting on Ferroelectricity, Jeju, South Korea, June 28 - July 1, 2010.
  12. J. J. Lee, Y. K. Hong, S. Bae, J. Jalli, J. H. Park, G. S. Abo, G. W. Donohoe, and B. C. Choi, "Integrated Ferrite Film Inductor for Power Systems-on-a-chip (PowerSoC) Smart Phone Applications," paper No. 097, presented at the 2010 International Conference on Microwave Magnetics, Boston, MA, June 1-4, 2010.
  13. J. Jalli, Y. Hong, S. Bae, J. Lee, G. S. Abo, J. Sur, S. Lee, I. Nam, H. Lee, and T. Mewes, "Microwave properties of Lanthanum (La)-doped Y-type hexaferrite single crystal", Paper No. BW-02 (poster), presented at the 11<sup>th</sup> Joint Magnetism and Magnetic Materials/IEEE International Magnetics Conference, Washington, DC, January 18-22, 2010.
  14. J. Lee, Y. Hong, S. Bae, J. Park, J. Jalli, G. S. Abo, B. Choi, and G. W. Donohoe, "High quality factor Ni-Zn Ferrite Planar Inductor", Paper No. GX-08 (poster), presented at the 11<sup>th</sup> Joint Magnetism and Magnetic Materials/IEEE International Magnetics Conference, Washington, DC, January 18-22, 2010.
  15. S. Bae, Y. Hong, J. Lee, W. Sung, J. Kum, W. Ahn, S. Park, G. S. Abo, J. Jalli, and J. Park, "Miniaturized broadband ferrite T-DMB antennas for mobile phone applications", Paper No. FX-07 (poster), presented at the 11<sup>th</sup> Joint Magnetism and Magnetic Materials/IEEE International Magnetics Conference, Washington, DC, January 18-22, 2010.
  16. S. Bae, Y. Hong, J. Lee, J. Park, J. Jalli, G. S. Abo, H. Kwon, and C. Jayasooriya, "Hexaferrite ring patch antenna for W-LAN multiple-input multiple-output antenna

- applications”, Paper No. FX-06 (poster), presented at the 11<sup>th</sup> Joint Magnetism and Magnetic Materials/IEEE International Magnetics Conference, Washington, DC, January 18-22, 2010.
17. G. S. Abo, Y. Hong, J. Jalli, S. Bae, J. Lee, J. Park, N. Neveu, S. Kim, and J. Sur, “Modeling of hysteresis loops for spherical barium ferrite (S-BaFe) particles with uniaxial anisotropy”, Paper No. DP-06 (poster), presented at the 11<sup>th</sup> Joint Magnetism and Magnetic Materials/IEEE International Magnetics Conference, Washington, DC, January 18-22, 2010.
  18. J. Park, Y. Hong, S. Bae, J. J. Lee, J. Jalli, G. S. Abo, N. Neveu, C. Choi, J. Lee, “Magnetic moment and crystalline anisotropy calculations for MnAl permanent magnet”, Paper No. AW-15 (poster), presented at the 11<sup>th</sup> Joint Magnetism and Magnetic Materials/IEEE International Magnetics Conference, Washington, DC, January 18-22, 2010.
  19. J. Jalli, Y. Hong, S. Bae, J. Lee, G. S. Abo, S. Gee, J. C. Sur, and S. G. Kim, “Conversion of nanosized spherical magnetite (S-Mag) to spherical barium ferrite (S-BaFe) nanoparticles for high density particulate recording media”, Paper No. DP-08 (poster), presented at the IEEE International Magnetics Conference, Sacramento, CA, May 4-8, 2009.
  20. J. Lee, Y. Hong, S. Bae, J. Jalli, G. S. Abo, W. Seoung, W. Ahn, S. Park, C. Choi, and J. Lee, “Broadband  $\text{Ni}_x\text{Zn}_{0.8-x}\text{Cu}_{0.2}\text{Fe}_2\text{O}_4$  electromagnetic absorber for 1 GHz application”, Paper No. CG-02 (oral), presented at the IEEE International Magnetics Conference, Sacramento, CA, May 4-8, 2009.
  21. S. Bae, Y. Hong, J. Lee, J. Jalli, G. S. Abo, B. Kim, and G. W. Donohoe, “High Q ferrite film inductor for on-chip power module”, Paper No. EH-04 (oral), presented at the IEEE International Magnetics Conference, Sacramento, CA, May 4-8, 2009.
  22. A. Lyle, Y. Hong, B. Choi, G. S. Abo, J. Jalli, S. Bae, R. Syslo, M. Park, G. W. Donohoe, “Spin-polarized current switching of Co/Cu/Py Pac-man type II”, Paper No. FD-09 (oral), presented at the IEEE International Magnetics Conference, Sacramento, CA, May 4-8, 2009.
  23. S. Bae, Y. Hong, J. Lee, J. Jalli, G. S. Abo, W. Sung, G. Kim, S. Park, J. Kum, and H. Kwon, “ $\text{Co}_2\text{Z}$  hexaferrite T-DMB antenna for mobile phone”, Paper No. FE-07 (oral), presented at the IEEE International Magnetics Conference, Sacramento, CA, May 4-8, 2009.
  24. A. Lyle, Y. K. Hong, B. C. Choi, G. S. Abo, M. H. Park, S. H. Gee, J. Jalli, and G. W. Donohoe, “Spin-polarized current switching of Co/Cu/Py elongated Pac-man spin-valve”, Paper No. CU12 (poster), presented at the Asian Magnetics Conference, Busan, Korea, Dec. 10-13, 2008.

25. S. Bae, Y. K. Hong, J. J. Lee, J. Jalli, G. S. Abo, A. Lyle, I. T. Nam, W. M. Seong, G. H. Kim, "New synthetic route of single-phase Z-type ( $\text{Ba}_3\text{Co}_2\text{Fe}_{24}\text{O}_{41}$ ) hexaferrite particles", Paper No. AP14 (poster), presented at the Asian Magnetism Conference, Busan, Korea, Dec. 10-13, 2008.
26. J. Jalli, Y. Hong, S. Gee, J. C. Sur, K. An and T. Hyeon, "Spherical Barium Ferrite (S-BaFe) 20-22 nm sized particles for particulate recording media", Paper No. CW-08 (poster), presented at the 53rd Annual Conference on Magnetism and Magnetic Materials, Austin, TX, Nov. 10-14, 2008.
27. A. Lyle, Y. Hong, B. C. Choi, G. S. Abo, H. Han, J. Jalli, S. Bae, J. Lee, P. LeClaire, R. Syslo, G. W. Donohoe, and S. Gee, "Spin-polarized current stimulation of 100 nm dual vortex Co/Cu/Py spin valve nanopillars", Paper No. AS-11 (poster), presented at the 53rd Annual Conference on Magnetism and Magnetic Materials, Austin, TX, Nov. 10-14, 2008.
28. S. Bae, Y. Hong, J. Lee, J. Jalli, G. S. Abo, A. Lyle, W. Seong, and J. Keum, "Low loss Z-type barium ferrite ( $\text{Co}_2\text{Z}$ ) for T-DMB antenna application", Paper No. AV-15 (poster), presented at the 53rd Annual Conference on Magnetism and Magnetic Materials, Austin, TX, Nov. 10-14, 2008.
29. J. Jalli, Y. Hong, S. Bae, J. Lee, M. Kothakonda, G. S. Abo, A. Lyle, S. Gee, H. Lee, T. Mewes, J. C. Sur, and S. Lee, "Growth and characterization of 144  $\mu\text{m}$  thick barium ferrite single crystalline film for microwave device application", Paper No. DS-01 (poster), presented at the 53rd Annual Conference on Magnetism and Magnetic Materials, Austin, TX, Nov. 10-14, 2008.
30. S. Bae, Y. K. Hong, J. J. Lee, G. S. Abo, J. Jalli, A. Lyle, H. Han, and G. W. Donohoe, "Optimized design of low voltage high current ferrite planar inductor for 10 MHz on-chip power module", Paper No. I-3, presented at the Global KMS International Conference, Jeju, Korea, October 23-25, 2008.
31. S. Bae, Y. K. Hong, J. J. Lee, G. S. Abo, J. Jalli, A. Lyle, S. H. Park, and W. M. Sung, "Miniature IL chip antenna for T-DMB applications", Paper No. I-4, presented at the Global KMS International Conference, Jeju, Korea, October 23-25, 2008.
32. S. Bae, Y. Hong, J. Lee, G. S. Abo, J. Jalli, A. Lyle, H. Han, and G. W. Donohoe, "High Q and high current NiZnCu ferrite inductor for on-chip power module", Paper No. AG-04 (oral), presented at the IEEE International Magnetism Conference, Madrid, Spain, May 4-8, 2008.
33. A. Lyle, Y. Hong, B. C. Choi, J. Rudge, G. S. Abo, S. Gee, H. Han, J. Jalli, and G. W. Donohoe, "Fabrication of 8x8 array of spin valve pillars and MR characterization", Paper No. AS-01 (poster), presented at the IEEE International Magnetism Conference, Madrid, Spain, May 4-8, 2008.

34. S. Bae, Y. Hong, J. Lee, J. Jalli, G. S. Abo, A. Lyle, H. Han, and G. W. Donohoe, "Optimization of design parameters for ferrite inductor for 10 MHz on-chip power module", Paper No. CQ-12 (poster), presented at the IEEE International Magnetics Conference, Madrid, Spain, May 4-8, 2008.
35. J. Jalli, Y. Hong, S. Gee, J. Lee, S. Bae, G. S. Abo, A. Lyle, H. Han, J. Kim, H. Lee, and S. Lee, "Ferrimagnetic  $Ba_{0.5}Sr_{1.5}Zn_2Fe_{12}O_{22}$  (Zn-Y) single crystal barium ferrites", Paper No. EH-10 (oral), presented at the IEEE International Magnetics Conference, Madrid, Spain, May 4-8, 2008.
36. J. Jalli, Y. Hong, S. Gee, J. Lee, S. Bae, G. S. Abo, A. Lyle, H. Han, J. Kim, H. Lee, and S. Lee, "Magnetic and microwave properties Sm-doped  $SrFe_{12}O_{19}$  single crystals", Paper No. EU-06 (poster), presented at the IEEE International Magnetics Conference, Madrid, Spain, May 4-8, 2008.
37. J. Jalli, Y. Hong, S. Gee, G. S. Abo, H. Han, A. Lyle, and T. Mewes, "Microwave and magnetic properties of Mn substituted Zn-Y type barium ferrite single crystals", Paper No. CT-05 (poster), presented at the 52nd Annual Conference on Magnetism and Magnetic Materials, Tampa, FL, Nov. 5-9, 2007.